

DESIGN AND DEVELOPMENT OF MODULAR ELECTROCHROMIC DEVICE FOR ACTIVE CAMOUFLAGING

A Thesis Submitted

in Partial Fulfilment of the Requirements

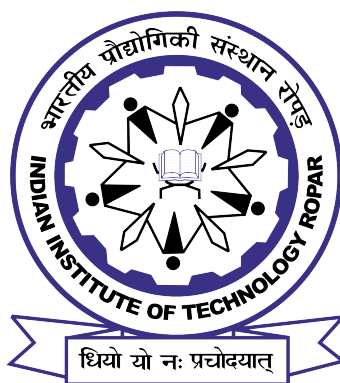
for the Degree of

DOCTOR OF PHILOSOPHY

by

Vishal Agrawal

(2017mez0016)



DEPARTMENT OF MECHANICAL ENGINEERING
INDIAN INSTITUTE OF TECHNOLOGY ROPAR

November, 2023

Vishal Agrawal: *Design and development of modular electrochromic device for active camouflaging*

Copyright ©2023, Indian Institute of Technology Ropar

All Rights Reserved

This thesis is dedicated to my father - Late Shri. Vinod Agrawal.

Declaration of Originality

I hereby declare that the work which is being presented in the thesis entitled **Design and Development of Modular Electrochromic Device for Active Camouflaging** has been solely authored by me. It presents the result of my own independent investigation/research conducted during the time period from Jan 2018 to Nov 2023 of PhD. Thesis submission under the supervision of Dr. Prabhat K Agnihotri, Associate Professor, Department of Mechanical Engineering, Indian Institute of Technology Ropar and Dr. Ekta Singla, Associate Professor, Department of Mechanical Engineering, Indian Institute of Technology Ropar. To the best of my knowledge, it is an original work, both in terms of research content and narrative, and has not been submitted or accepted elsewhere, in part or in full, for the award of any degree, diploma, fellowship, associateship, or similar title of any university or institution. Further, due credit has been attributed to the relevant state-of-the-art and collaborations (if any) with appropriate citations and acknowledgments, in line with established ethical norms and practices. I also declare that any idea/data/fact/source stated in my thesis has not been fabricated/falsified/ misrepresented. All the principles of academic honesty and integrity have been followed. I fully understand that if the thesis is found to be unoriginal, fabricated, or plagiarized, the Institute reserves the right to withdraw the thesis from its archive and revoke the associated Degree conferred. Additionally, the Institute also reserves the right to appraise all concerned sections of society of the matter for their information and necessary action (if any). If accepted, I hereby consent for my thesis to be available online in the Institute's Open Access repository, inter-library loan, and the title & abstract to be made available to outside organizations.


Signature

Name: Vishal Agrawal

Entry Number: 2017mez0016

Program: PhD

Department: Mechanical Engineering

Indian Institute of Technology Ropar

Rupnagar, Punjab 140001

Date: Nov 06, 2023

Acknowledgement

Thank you, God, for bestowing upon me the opportunity to work at the Indian Institute of Technology Ropar which provided me with one of the nation's best research facilities and environment. It is at IIT Ropar that I learned the art of research and this was not possible without the knowledge, wisdom and research attitude I gained from my PhD supervisors. I am extremely grateful to my thesis supervisors *Dr. Prabhat K. Agnihotri* and *Dr. Ekta Singla* for allowing me to make a balance between my PhD work and my personal life. Their invaluable guidance and constant encouragement to reach perfection can never be forgotten. I thank them for bestowing overwhelming trust, cultivating independent thinking, and having time for those long research-related discussions whenever needed.

I sincerely thank my doctoral committee members, *Dr. Navin Kumar*, *Dr. S S Padhee*, *Dr. Prabir Sarkar* of Department of Mechanical Engineering, and *Dr. Abhinav Dhall* of the Department of Computer Science and Engineering, for continuously monitoring the work and provide me the valuable suggestions. I also want to thank *Dr. Dhiraj K Mahajan* and his lab members *Dr. Tushita Rohilla*, *Dr. Navneet Kumar*, *Dr. Aman Arora*, *Mr Vishal Singh*, *Mr Mukesh*, *Dr Ahmed* and *Mr Dharmendra tyagi* for giving access to an electrochemical workstation and when required. I would like to extend my gratitude to *Dr. Devranjan Samanta* and *Mr Khusro* to provide me access for performing the rheology experiments. Moreover, I thank *Mr Ram Kumar*, *Mr Pankaj Thakur*, and *Mr Harpreet* for their help and support during my PhD work. My gratitude is towards the *Dr. Rajesh Kumar* and *Ms. Tanushree* of Indian Institute of Technology Indore to support me in the spectroelectrochemical measurements. I am very much thankful to *HOD* and *Departmental Research Facilities* of the Department of Mechanical Engineering for their unconditional support.

I am indebted to the immense discussion I had with my colleagues, clearing my thoughts and opening up new pathways in the road to finish this work. Therefore, I would like to thank my lab mates from MAdMatLab - *Dr. Beant Kaur*, *Dr. Harpreet Bedi*, *Dr. Jasdeep Bhinder*, *Dr. Viney Ghai*, *Dr. Ankit Baranwal*, *Mr. Ankit Chauhan*, *Mr. Sudhendu Tiwari*, *Mr. Vinay Kumar*, *Mr. Shiva Bansal*, *Mr. Devnarayan*, *Mr. Vaibhav*, *Mr. Prakash*, and from MOIR Lab - *Dr. Sakshi Gupta*, *Dr. Anubhav Dogra*, *Mr. Shreyas*, *Mr. Sumitkumar*, *Mr. Saiful*, *Ms Priyanka*, *Mr. Shudhanshu*, *Mr. Vikrant* and *Ms. Bhavna*. I would like to extend my gratitude to *Dr. Monika Chaudhary* and *Dr. Gaje Singh* of Department of Chemistry to discuss the concepts of chemistry whenever required. I also thanks *Mr. Iyeppan* and *Mr. Dilbagh* of Department of Electrical Engineering for their assistance in the preparation of the integrated electrical circuits. Many of my acquaintances at

IIT Ropar made my stay there more pleasurable, including *Hreetabh*, *Neha Mehani*, *Avneesh*, *Rakesh*, *Piyush*, *Kalyani*, *Chandersekhar* to name a few. Diverse activities for the development of students made my time at IIT Ropar more enjoyable.

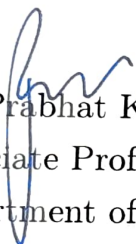
In the end, my deepest gratitude to my wife *Megha*, who always supports me like a backbone and motivates me throughout the PhD journey. She made it possible for me to balance between PhD work and family responsibilities. *Smiley* and *Shiny*, my daughters also bring a lot of energy and motivation to my life, with the goal of ensuring a bright future for her. I would also like to express my gratitude towards my mother who always encouraged and provided me platform throughout my academics. I would like to thank my sister *Pallavi* and other family members for their support throughout my journey. Finally, My heartfelt thanks to all those COVID warriors who risked their lives to save us.

Certificate

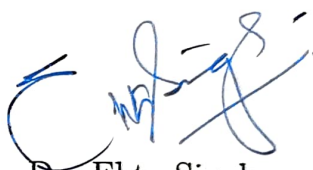
This is to certify that the thesis entitled **Design and Development of Modular Electrochromic Device for Active Camouflaging**, submitted by **Vishal Agrawal (2017mez0016)** for the award of the degree of **Doctor of Philosophy** of Indian Institute of Technology Ropar, is a record of bonafide research work carried out under my (our) guidance and supervision. To the best of my knowledge and belief, the work presented in this thesis is original and has not been submitted, either in part or full, for the award of any other degree, diploma, fellowship, associateship or similar title of any university or institution.

In my (our) opinion, the thesis has reached the standard fulfilling the requirements of the regulations relating to the Degree.

Date: Nov 06, 2023



Dr. Prabhat K. Agnihotri
Associate Professor
Department of Mechanical Engineering
Indian Institute of Technology Ropar
Rupnagar, Punjab 140001



Dr. Ekta Singla
Associate Professor
Department of Mechanical Engineering
Indian Institute of Technology Ropar
Rupnagar, Punjab 140001

Abstract

Active camouflage refers to the dynamic change in color and/or texture of an organism/device to blend with the surroundings. Chameleons, octopuses, squid, etc. are some natural species that have this amazing ability. They are capable of adapting according to their habitat and survive. The present thesis aims to mimic their active camouflaging ability in an artificial system. It is a challenge to develop a general system considering the huge variations in color space. Therefore, we have limited ourselves to the greenish surroundings which represent a large domain of environments for surveillance applications. Active camouflaging has two major requirements; the first is to collect and quantify the information of surroundings, and the second is to make a device that can change its color using this information. A thorough literature survey reveals that algorithms have been developed to form digital patterns based on the collected information of surroundings. However, these are not utilized to change the patterns in an artificial physical system. In addition, novel materials are reported in the literature that are capable of dynamic changes in color and texture. High input power, complex design, and limited applicability are the main problems with these reported solutions. To address some of these issues, a modular electrochromic device (ECD) capable of changing color under an applied voltage is designed and developed in this work. ECD is a layered device comprising of electrochromic polymer (ECP), gel electrolyte (GE), and electrodes. Electrochromic polymer is responsible for color changing due to a jump in energy gap at different excited states under an applied potential. GE provides the ion and maintains a gap between the compliant electrodes. Repeated coloration-decoloration cycles, varying temperature, humidity, and mechanical loading of ECDs may induce cracks, cuts, and damage in GE. In such scenarios, ECD needs to be replaced. Therefore, it is essential to develop repairing strategies for GE to enhance the operational life of ECD. In addition, there are some other requirements of green vegetation that are essential for the development of active camouflage devices such as the multiple shades of green color in a single leaf, brown color of sand, mud, and dry leaves.

To address these issues, the present thesis is divided into four objectives. The first objective is to induce self-healing behavior in the gel electrolyte (GE). GE comprises salt, solvent and polymer. Salt provides the ions, solvent gives the passage for ions and polymer solidifies the electrolyte. Polymethyl methacrylate (PMMA) is used as a polymer due to its excellent self-healing characteristics. The concentration of PMMA in GE is varied to optimize the composition of GE. The recovery in tensile strength and ionic conductivity of GE is found to be maximum for 15 wt% PMMA. Hence, GE with 15 wt% of PMMA is used to fabricate ECD. The effect of healing on the color contrast of ECD is also investigated. It is shown that the

color contrast of ECD prepared with healed GE approaches that of original ECD with increasing healing time. Optimized weight percentage (15%) of PMMA in GE is used subsequently for the development of ECDs.

After achieving the self-healing in GE, experiments are performed to achieve varying shades of green color and quantify the coloration of ECDs. Polyaniline (PANI) is used as an ECP which gives the light green, green, and blue colors at reduced, neutral and oxidized states respectively. Following Lambert's law, PANI of different thicknesses (250 nm – 650 nm) is used in ECDs to modulate the shades of green in ECD. PANI is coated on ITO electrode by electropolymerization method using cyclic voltammetry (CV) technique. To vary the thickness, PANI is coated for 5, 10, 15, and 20 number of cycles. Comparative analysis is performed by digital images, spectroelectrochemical measurements, and spectral colorimetry. Results show that the minimum thickness (≥ 400 nm) of the ECP layer is required to get the noticeable color change in ECD. The color contrast of ECD ranges from 14 % to 80 % at both excited states and it increases with the increase in thickness of the ECP layer. ECDs get different shades of green and blue colors due to the variation in thickness.

In the next part, an experimental investigation is carried out to achieve the shades of brown and green color in ECD. Dual ECDs are fabricated and tested using Poly (3-hexyl thiophene) (P3HT) as another electrochromic polymer with PANI. P3HT gives magenta and cyan colors at neutral and oxidized states respectively. Complementary dual ECD has P3HT and PANI ECP layers on the opposite electrodes while hybrid dual ECD has both the ECP layers on the same electrode. Comparative analysis revealed that the hybrid dual ECD has the ability to achieve green, brown, and blue colors at reduced, neutral, and oxidized states.

To prepare the active camouflage device as a proof-of-concept, an Electrochromic Modular Architecture is designed and fabricated using four types of ECDs (3-single ECDs of different thickness of PANI and 1-hybrid dual ECD). To collect the surrounding information, a Pattern Detection Algorithm is developed which includes image acquisition, shadow removal, image segmentation, and image processing. A modular image is developed using surrounding information followed by the system integration of the Electrochromic Modular Architecture and Pattern Detection Algorithm. Modular image has the same number of modules arrangement as of electrochromic modular architecture. Then, a simulation is performed to get the best possible patterns. Digital Modular Architecture is prepared using the design principle of Electrochromic Modular Architecture and digital images of all four types of ECDs. Simulated Digital Modular Architecture gives the required input potentials of best-suited patterns. Using the simulation results, the potential is applied to the ECDs of Electrochromic Modular Architecture which gives different patterns for different surroundings. It is envisaged that the findings

of the present study will be a significant step in designing the active camouflage layers (arrangements of devices) for the applications of surveillance, defense, and wildlife discoveries.

Keywords: Active camouflage, electrochromic device, Polyaniline, P3HT, self healing, gel electrolyte, modular

List of Publications

Journal

Article 1: **Agrawal, V.**, Singla, E. and Agnihotri, P.K., 2022. Modulation of optical properties of electrochromic device. *Journal of Materials Science: Materials in Electronics*, 33(27), 21935-21954. <https://doi.org/10.1007/s10854-022-08982-4>

Article 2: **Agrawal, V.**, Singla, E. and Agnihotri, P.K., 2023. Exploiting self-Healing characteristics of poly (methyl methacrylate) in gel electrolyte for application in electrochromic devices. *ACS Applied Engineering Materials*, 1(6), 1543–1553. <https://doi.org/10.1021/acsaenm.3c00109>

Article 3: **Agrawal, V.**, Singla, E. and Agnihotri, P.K., 2023. Design and fabrication of dual electrochromic device with a broader color space. (Submitted).

Article 4: **Agrawal, V.**, Agnihotri, P.K. and Singla, E., 2023. Bio-inspired active camouflage device: a modular design approach. (Submitted).

Patents

Patent 1: Agnihotri, P.K., Singla, E. and **Agrawal, V.**, 2023. An Electrochromic device and method for fabrication of Electrochromic device. (Application No: 202311072527).

Patent 2: Singla, E., Agnihotri, P.K. and **Agrawal, V.**, 2023. A system for optical active camouflaging and a method thereof. (Application No: 202311075188).

Contents

Declaration	vii
Acknowledgement	ix
Certificate	xi
Abstract	xiii
List of Publications	xvii
List of Symbols	xxxi
List of Abbreviations	xxxiii
1 Introduction	1
1.1 Active camouflage materials	1
1.2 Electrochromic device	3
1.3 Self healing in gel electrolyte	6
1.4 Surrounding detection	7
1.5 Key issues	8
1.6 Objectives	9
1.7 Organization of thesis	9
2 Materials and methods	11
2.1 Materials	11
2.1.1 Gel electrolyte (GE)	11
2.1.2 Preparation of PANI and P3HT electrochromic polymers . . .	11
2.1.3 Fabrication of single and dual electrochromic devices	13
2.1.4 Active camouflage device	14
2.2 Characterizations	15
3 Exploiting self healing characteristics of polymethyl methacrylate (PMMA) in gel electrolyte for application in electrochromic devices	17
3.1 Introduction	17
3.2 Experimental	19
3.2.1 Materials and preparation	19

3.2.2	Characterization	20
3.3	Results and discussion	22
3.3.1	Fourier transform infrared spectroscopy (FTIR)	22
3.3.2	Effect of PMMA on the glass transition temperature of GE	22
3.3.3	Effect of PMMA on the mechanical properties and self healing behavior of GE	24
3.3.4	Effect of PMMA concentration on the ionic conductivity of GE	32
3.3.5	Comparative analysis of electrochromic device (ECD)	33
3.4	Conclusion	36
4	Modulation of optical properties of electrochromic device	39
4.1	Introduction: Electrochromic devices	39
4.2	Experimental details	41
4.2.1	Materials and preparation	41
4.2.2	Characterizations	42
4.3	Results and discussion	43
4.3.1	Preparation of PANI layer	44
4.3.2	Effect of CV cycles on the roughness and morphology of electrochromic PANI layer	44
4.3.3	Optical properties of electrochromic PANI layer	48
4.3.4	AC conductivity of ECD	48
4.3.5	Electrochemical properties of ECD	52
4.3.6	Spectroelectrochemical properties of ECD	52
4.3.7	Spectral colorimetric analysis	56
4.4	Conclusion	59
5	Design and fabrication of dual electrochromic device with broader color space	61
5.1	Introduction	61
5.2	Experimental Section	63
5.2.1	Materials and preparation	63
5.2.2	Characterization	63
5.3	Results and Discussion	64
5.3.1	Thickness, roughness and morphology of PANI and P3HT electrochromic films	65
5.3.2	Optical properties of PANI and P3HT electrochromic films	68
5.3.3	Electrochemical properties of ECDs	69
5.3.4	Spectroelectrochemical properties of dual ECDs	69
5.4	Conclusion	76

6	Bio-inspired active camouflage device: A modular design approach	79
6.1	Introduction	79
6.2	Materials and method	81
6.2.1	Fabrication of electrochromic device (ECD)	81
6.2.2	Characterization	81
6.2.3	Development of active camouflage device	82
6.3	Results	83
6.3.1	Pattern detection algorithm: an environment representation	83
6.3.2	Pattern formation hardware: an array	86
6.3.3	Active camouflage device	88
6.4	Conclusion	93
7	Conclusion	95
7.1	Summary of the work	95
7.2	Future scope	96
	References	97

List of Figures

2.1	Processing steps followed for fabrication of gel electrolyte.	12
2.2	(a) Photographic image of electrochemical set up used for electrochemical polymerization of polyaniline (PANI) and (b) green color polyaniline (PANI) film on ITO/PET sheet after electro polymerization process	12
2.3	Schematic of different electrochromic devices (ECD) showing architecture of (a) ECD1(PET/ITO/PANI/GE/ITO/PET), (b) ECD2(PET/ITO/P3HT/GE/ITO/PET), (c) ECD3(PET/ITO/PANI/GE/P3HT/ITO/PET) showing side 1 and side 2 to take the separate measurements from both sides and (d) ECD4(PET/ITO/PANI/P3HT/GE/ITO/PET).	13
2.4	(a) Setup of active camouflage device showing electrochromic modular architecture with integrated circuit and (b) casing of electrochromic modular architecture contains 25 cavities prepared on the solid-works.	14
2.5	Schematic showing original and healed GE specimens for (a) tensile test, (b) ionic conductivity test and (c) electrochromic device.	16
3.1	(a)FTIR curve and (b) its zoomed view comparing pure PC, pure LiClO_4 , PMMA powder, liquid electrolyte (LE), GE15, GE25, GE35, and GE50 in the range of $400 - 2800 \text{ cm}^{-1}$ and $1700 - 1850 \text{ cm}^{-1}$ respectively. Molecular structure of (c) PC and (d) PMMA. Schematic showing the (e) Li^+ - PMMA interaction and (f) spring-mass system represents m as Li^+ , S1 and S2 as $(\text{C}=\text{O})$ group of PC and PMMA respectively.	21
3.2	(a) Loaded sample for shear test in DMA to perform the temperature sweep, (b) $\tan \delta$ vs temperature curves and (c) Glass transition temperature (T_g) of GE15, GE25, GE35 and GE50.	23
3.3	(a) $\sigma - \epsilon$ curve of GE as a function of PMMA wt% and its zoomed view. (b) Schematic showing the uncoiling of PMMA chains on the application of tensile load.	24
3.4	Variation in toughness modulus of GE as a function of PMMA concentration.	25

3.5	Comparative $\sigma - \varepsilon$ curve of original and healed specimen of GE15 for (a) 10 min and (b) 6 hours healing time. Optical images of GE15 as (c) original, (d) after break, (e) after rejoin, (f) after 10 mins and (g) 6 hours of healing.	26
3.6	Comparing $\sigma - \varepsilon$ curve of original and healed specimens of GE25, GE35 and GE50 at healing time of (a, c, e) 10 min and (b, d, f) 6 hours respectively.	27
3.7	Recovery of (a) tensile strength, (b) elongation at break and (c) toughness modulus of GE15, GE25, GE35 and GE50 as a function of healing time. (c) GE25 during the tensile test marked the healed point (i) before stretching and (ii) after failure. (d) Optical images of (i) GE25, (ii) GE35 and (iii) GE50 after 6 hours of healing time. .	29
3.8	Schematic of (a) GE15 and (b) GE25 (original, after break, healed) network showing the re-crosslinking of Li^+ —PMMA at the interface of two parts (I and II).	30
3.9	(a) Schematic of notched specimen and (b) corresponding $F - \delta$ curve of GE50 sample.	32
3.10	Ionic conductivity of original and healed GE specimens.	33
3.11	Cyclic voltammetry curve of original and healed ECDs.	34
3.12	Digital images of (a) original ECD and (b) 10 min and (c) 6 hours healed ECDs at different excited states.	35
3.13	Mean of the color coordinates of digital images of (a) original ECD, healed ECDs after (b) 10 min and (c) 6 hours of healing at different excited states in HSV color space.	36
4.1	(a) Processing steps followed to fabricate ECD, and (b) Schematic of ECD showing all the layers and connections (PET/ITO/GE/PANI/ITO/PET)	41
4.2	(a) Processing steps followed to fabricate ECD. (b) Schematic of ECD showing all the layers and connections (PET/ITO/GE/PANI/ITO/PET) (c) Photographic image of electrochemical set up used for electrochemical polymerization of polyaniline (PANI) and (d) green color polyaniline (PANI) film on ITO/PET sheet after electro polymerization process	43

4.3	Optical images are showing the notch in (a) PANI5, (d) PANI10, (g) PANI15 and (j) PANI20 layer which is created to measure the thickness through AFM analysis. AFM micrographs of (b) PANI5, (e) PANI10, (h) PANI15 and (k) PANI20 layer showing all 10 readings in each film. AFM topographs of (c) PANI5, (f) PANI10, (i) PANI15 and (l) PANI20 films. Variation of (m) thickness and (n) surface roughness of PANI layers with increasing number of CV cycles. 2nd order polynomial used to fit the experimental data points is also included in (m) and (n).	45
4.4	SEM micrographs of (a) bare ITO, (b) PANI5, (c) PANI10, (d) PANI15 and (e) PANI20 films. The zoomed micrographs of these samples are also included in (b1 – d1).	46
4.5	Photographic images of (a) PANI5, (b) PANI10, (c) PANI15 and (d) PANI20 films showing the shades of green color. Comparison of (e) Absorbance vs wavelength and (f) Reflectance vs wavelength (curve of ITO/PET is in inset) spectra of all the PANI films.	47
4.6	(a) Ideal Nyquist plot and its equivalent circuit. (b) Nyquist plot of all the ECDs and their (c) zoomed view. Equivalent circuit of (d) ITO only, (e) ECD-5, (f) ECD-10, (g) ECD-15 and (h) ECD-20. (i) Schematic of charge polarization at electrode/ electrolyte interface and (j) schematic representation of ion diffusion in (j1) ECD-5 and (j2) ECD-20. (k) AC conductivity and equivalent series resistance (R) of ITO and all the ECDs.	49
4.7	CV curves of all the ECDs	51
4.8	Photographic images at reduced, neutral and oxidized states (1-3), absorbance (4) and transmittance (5) spectra of (a) ECD-5, (b) ECD-10, (c) ECD-15 and (d) ECD-20 at their respective redox potentials.	54
4.9	Transmittance vs wavelength spectra of all ECDs at (a) neutral, (b) reduced and (c) oxidized state.	54
4.10	Photographic images at reduced, neutral and oxidized states (1-3), absorbance (4) and transmittance (5) spectra of (a) ECD-5, (b) ECD-10, (c) ECD-15 and (d) ECD-20 at their respective redox potentials.	57

5.1	(a) Optical image showing the notch and (b) AFM micrograph of P3HT film with 10 readings using height to measure the thickness. Optical images and peak force measurement of a cross-sectional view of (c) PANI and PANI/P3HT films. AFM topographs showing roughness of (e) PANI, (f) P3HT and (g) PANI-P3HT and deformation measurement of (h) PANI and (i) PANI/P3HT.	64
5.2	Morphology of (a) PANI, (b) P3HT fiber, (c) P3HT after spin coating and (c) PANI-P3HT films.	66
5.3	(a) Schematic of PANI-P3HT film (PET/ITO/PANI/P3HT) and (b) weight % of different elements is showing in different regions at cross-section of PANI-P3HT film.	66
5.4	(a) Absorbance-wavelength and (b) reflectance-wavelength spectra of ITO/PET sheet, PANI, P3HT and PANI-P3HT films.	67
5.5	Cyclic voltammetry curve of ECDs.	68
5.6	Absorbance-wavelength spectra of (a) ECD1, (c) ECD2, ECD3 from (e) side 1 and (f) side 2; and (h) ECD4. Transmittance-wavelength spectra of (b) ECD1 and (d) ECD2. (g) Schematic of ECD3 showing (i) negative and (ii) positive electrodes connected to the PANI layer.	71
5.7	Current density -time curve of (a) P8, (b) P3, (c) P8GEP3 and (d) P8P3 to find the cyclic stability.	75
5.8	Morphology of (a) PANI (P8), (b) P3HT (P3) and (c) PANI/P3HT (P8P3) films after the cyclic stability test.	76
6.1	Flow chart of pattern detection algorithm.	82
6.2	(a) Showing difference 'd' between centroid of two clusters 'a' and 'b' in k-means clustering algorithm and (b) comparing (i) original image, (ii) image after shadow removal and (iii) modular image of green surroundings.	83
6.3	(a) Image of forest vegetation showing multiple shades of green color. Two points showing different RGB color coordinates, (b) and (c) are the examples of (i) segmented part of surrounding image and (ii) color recognition from segmented part.	84
6.4	Schematic of (a) M^1 , M^2 and M^3 (3 types of PANI thickness); and (b) M^4 (PANI-P3HT) modules.	85
6.5	Four types of modules are arranged in electrochromic modular architecture.	86
6.6	Digital images of (a) M^1 , (b) M^2 , (c) M^3 and (d) M^4 at different voltages.	87
6.7	Comparing modular image and digital modular architecture.	88

6.8	Comparing (i) original image, (ii) modular image and (iii) digital modular architecture (MoD_A). MoD_A representing the best suited pattern to particular surrounding by optimizing the digital images of modules ('n' = neutral state (0 V), 'o' = oxidized state (2.5 V) and 'r' = reduced state (-2.5 V)).	88
6.9	Images of green vegetation in the presence of (a) skylight showing bluish green color and (b) sunlight showing yellowish green color of grass. Turtle bot (i) with and (ii) without digital modular architecture (MoD_A) under (c) skylight and (d) sunlight.	89
6.10	(a) Schematic showing mapping of segmented part of the modular image and module of electrochromic modular architecture, (b) circuit diagram and (c) active camouflage device changing patterns for different surroundings.	92

List of Tables

3.1	Comparison of current work with the reported gel electrolytes.	31
3.2	Mean square error (MSE) of digital images of GE15, GE25 and GE35 based ECD between neutral and excited states.	34
4.1	Oxidation and reduction voltage of ECD-5, ECD-10, ECD-15 and ECD-20.	51
4.2	Color contrast and response time of all the ECDs at redox potentials.	52
5.1	Comparing electrochromic properties of ECD1, ECD2, ECD3 and ECD4.	73
6.1	Compare structural similarity index measures of mobile robot, modular image and digital modular architecture with reference to surrounding images.	90

List of Symbols

ΔE	Color difference
η_{ce}	Coloration efficiency
λ_{ac}	AC conductivity
Q	Charge density
R	Equivalent series resistance
R_a	Surface roughness
T_g	Glass transition temperature
Z'	Real impedance
Z''	Imaginary impedance
λ_{ionic}	Ionic conductivity
U_T	Modulus of toughness
σ	Tensile strength
ε	Elongation at break
R_{CT}	Charge transfer resistance
C_{geom}	Geometrical capacitance
ω	Frequency

List of Abbreviations

ACD	Active Camouflage Device
AFM	Atomic Force Microscopy
CPE	Constant Phase Element
CV	Cyclic Voltammetry
DMA	Dynamic Mechanical Analysis
ECD	Electrochromic Device
ECP	Electrochromic Polymer
EIS	Electrochemical Impedance Spectroscopy
FTIR	Fourier Transform Infrared Spectroscopy
GE	Gel Electrolyte
MoD _A	Digital Modular Architecture
MoE _A	Electrochromic Modular Architecture
MoI	Modular Image
MSE	Mean Square Error
OD	Optical Density
P3HT	Poly(3-hexyl thiophene)
PANI	Polyaniline
PDA	Pattern Detection Algorithm
PFH	Pattern Formation Hardware
SEM	Scanning Electron Microscopy
SSIM	Structural Similarity Index Measure

Chapter 1

Introduction

Camouflaging is a phenomenon in which a body/device hides likely by blending with the surroundings. The survival probability of personnel or assets in hostile environments critically depends on the ability to camouflage. Fundamentally, camouflage is of two types; passive and active. Passive camouflage refers to matching colors, contours, patterns, or textures of organisms or objects with the surroundings, e.g. grasshopper, polar bear, patterning of security personal uniforms, equipment and landscapes, etc. One of the major drawbacks of passive camouflage is that it needs to be uniquely designed for each type of surrounding, making it less cost and time-effective. On the other hand, active camouflage refers to the dynamic phenomenon where an organism/device changes its color and/or texture to blend with the variable surroundings. Some of the bio-species like chameleons, octopuses, squid, etc have this ability. Active camouflaging finds applications in technical textiles, surveillance, security personal assets, and wildlife discoveries. Inspired by bio species, there are two main phenomena on which focus is required to achieve active camouflaging in man-made systems. First is the sensing of the surroundings and the other one is to bring the changes physically. Since many defense operations and wildlife discoveries are carried out in green vegetation, the focus of this work is to develop a device that can achieve active camouflaging in forest environments. The second phenomenon which includes the physical change of color is the most challenging task to achieve with the already available resources. Electrochromic devices (ECD) find the suitability to achieve it. ECD is a layered device that changes color on the application of voltage. It comprises of electrochromic and gel electrolyte (GE) layer sandwiched by electrodes and substrates. Repeated coloration-decoloration cycles, varying temperature, humidity, and mechanical loading of ECDs may induce cracks, cuts, and damage in GE. It resulted in the replacement of ECD which made it essential to develop the strategy to repair cuts and cracks in GE to enhance the operational life of ECD.

1.1 Active camouflage materials

Curiosity-driven understanding of natural materials/species has led to advancements in many technologically important areas and developing artificial camouflage is

no exception. It was observed that an Asian butterfly 'angled sunbeam' has silvery white ventral (bottom) wings that blend with the environment due to reflection resulting from diffuse illumination from surroundings [1]. Paradise whiptail changes color from blue to red using reflective strips on its body which contain iridophores cells and act as multilayer reflectors [2]. Leptocephallis are the flat and transparent larvae found in deep oceans. Transparency is an ideal phenomenon for the camouflage. Taking a clue from Leptocephallis larvae, Yuk H et al. developed transparent hydrogel-based actuators that are optically camouflaged in water [3]. A transparent soft robot is developed which is driven by transparent dielectric actuators [4]. Poly dimethyl siloxane (PDMS) based transparent structural film mimics the transparent wings of insects [5]. Cephalopods achieve active camouflage by using dense networks of pigmented, muscle-driven chromatophore cells which actuate under neuroelectrical stimulus [6, 7]. Artificial chromatophores are developed that are actuated by electroactive materials [8, 9]. Adaptive optoelectronic systems and protochromic devices are also developed with the cephalopod's skin-inspired design [10, 11]. Photonic crystals are responsible for causing the active color change in chameleons [12]. Chameleon inspired structural-color actuator works on vapochromic and vapomechanical response [13]. Another chameleon-inspired soft robot achieves artificial camouflage using thermochromism [14].

Apart from these studies, researchers have developed strategies to achieve camouflaging by dynamically changing the texture. Controlled bistable silicon cells were prepared with locally reinforced regions for morphing application [15]. Use of synthetic tissue groupings was reported which allows the programmable transformation of two-dimensional stretchable surfaces into targeted three-dimensional shapes [16]. A method was developed based on the combination of bimetallic nanodot arrays and electrochemical bias to mimic the chameleon skin [17]. Efforts are also being taken to evolve the color-changing strategies such as by using liquid dye, a microfluidic network was developed to change color, pattern, contrast, and luminescence of soft machines for camouflaging [18]. In addition, By using the concept of plasmonic effect, a flexible device was fabricated based on near-field coupling between plasmonic silver nanoparticles and an underlying conductor for color change through applied pressure [19]. Zhu et al. developed a flexible, high-contrast silicon metastructure embedded in a flexible membrane that can change the color from green to orange on stretching [20]. To change the fluorescence and illumination, elastomer-based material were also developed in some studies. An electro-mechano-chemically responsive elastomer was designed which exhibits a wide variety of fluorescent patterns under the application of electric field [21]. Moreover, an electroluminescent material was presented that changed

illuminance under deformation due to ZnS-phosphor doped dielectric elastomer layer sandwich by hydrogel electrodes [22]. Chou et al. developed a stretchable electronic skin that changes its color upon applying pressure using electrochromic materials [23].

1.2 Electrochromic device

An electrochromic device (ECD) is a multilayered device capable of changing the color on the application of voltage [24, 25, 26]. It finds applications in diverse engineering fields including energy storage, display, smart window, smart textiles, smart fabrics, etc., [27, 28, 29, 30, 31, 32]. It works on electrochromism which refers to the reversible color change on the application of voltage due to redox phenomena that occur in electrochromic materials. ECD consists of the electrochromic layer, a gel electrolyte sandwiched between the electrodes and substrates. An electrochromic layer is responsible for changing the color which changes its energy gap on the application of voltage.

The color and other performance parameters of ECD depend on various factors like types of electrodes [33], microstructure [34], band-gap [35] etc. In addition, the thickness and chemistry of the electrochromic layer also influence the electrochromic performance of ECD [36]. Initially, inorganic metal oxide layers are studied as an electrochromic material. Performance of Tungsten oxide and nickel oxide layers are studied as electrochromic materials [37, 38, 39, 40]. The electrochromic performance of organic materials is also investigated. Derivatives of viologen give the colorless and blue color at neutral and reduced states respectively [41]. Over inorganic and organic materials, electrochromic polymers (ECP) are increasingly used in ECDs [42, 43, 44] as they show a multitude of color variations with high color contrast and at low power consumption [45]. ECP are generally conjugated polymers which shows the electrochromism due to its conjugated backbone [46]. Polyaniline, polypyrrole, polythiophene and their derivatives are mainly explored as electrochromic polymers (ECP) [35]. The choice of electrochromic material depends on the specific ECD application requirements. Thiophene and its derivatives are used to get red, blue, and brown colors at different excited states [47, 48, 49]. Polynorbornene shows light yellow, green, and blue colors [33]. Poly(3,4-ethylenedioxythiophene) (PEDOT) converts from a blue color to a transparent state on oxidation [34]. Derivatives of tetra bipyridilium gives pink, purple, and beige colors [50]. Red-to-black electrochromism is achieved by 4,9-dihydro-s-indaceno [1,2-b:5,6-b']dithiophene [49]. Electrochromic polyimides and copolyimides change the color from pale yellowish to green to blue [51]. Polyaniline (PANI) undergoes multi-coloration states from light

green to green to blue if prepared in an acidic medium [52].

Further, the incorporation of secondary electrochromic material may enhance the electro-optical performance, and, the assembly is termed as dual ECD. Conventionally, both the electrochromic films are applied on the opposite electrodes separated by the gel electrolyte (GE) and performed complementary to each other. Prussian blue (PB) and viologen perform complementary to switch the color from sky blue to dark blue and transparent [53]. In another combination of viologen with P3HT, it shows transparent, magenta, and blue colors [42]. Combination of inorganic - inorganic dual ECDs is also explored by using tungsten trioxide (WO_3) with nickel oxide (NiO) [54, 55] [32] and vanadium pentoxide (V_2O_5) [56] which performed complementary to give the transparent, light blue and dark blue colors at different potentials. Polyaniline (PANI) and poly(ethylenedioxythiophene) (PEDOT) combinedly modulate the color from light blue to deep blue and improve the coloration efficiency [57] [14] while after doping with poly(styrene sulfonic acid) (PSS), they show pale yellow, light green and dark blue colors [58, 59]. PANI is also explored with the other derivatives of thiophene (P3MT [60] and P3HT [61]) in complementary dual ECD to make the comparative study with the single ECDs. Prussian blue (PB) with PANI is studied for variable-light transmission ECD and changes the dark blue state to transparent [62] and with PEDOT, gives light and dark blue shades for large area ECDs [63]. An investigation is also carried out with p-type and n-type polydithieno[3,4-b,3'4'-e]-[1,4]-dithiine (PDTH) in complementary dual ECD [64]. Complementary dual ECD works better when anodic and cathodic electrochromic materials are used simultaneously. It allows them to darken or bleach simultaneously in small driving force and response time. Unlike complementary dual ECD, both electrochromic films are placed on the same electrode in hybrid dual ECD. Efforts have been made to use the PANI [65] and P3HT [66] layers on the WO_3 film to enhance the electrochemical and electrochromic properties [15]. However the study in hybrid dual ECD is limited to the combination of inorganic-organic electrochromic materials.

Polyaniline (PANI) is the most explored ECP due to its three stable excited states (leucoemeraldine, emeraldine, pernigraniline) and shows the light green, green and blue colors at reduced, neutral, and oxidized states respectively [67]. Moreover, PANI is preferred due to its facile synthesis, reversible redox chemistry, excellent environmental stability, low cost, and high conductivity [68]. Different methods such as chemical oxidation, interfacial polymerization, microemulsion polymerization, and electrochemical polymerization are reported to polymerize PANI [69]. In the chemical method, an oxidizing agent is used to oxidize aniline monomer in an acidic medium which initiates the chain growth of polymer [70]. Drop coating [71], spin coating [72, 73], and dip coating [70] techniques are used to coat PANI on different

substrates. On the other hand, poly (3-hexyl thiophene) (P3HT) is one of the widely investigated thiophene derivatives. It is a magenta color electrochromic polymer (ECP) that changes to cyan at the oxidation state. In addition, P3HT is a soluble polymer that provides the flexibility to use different deposition techniques. Like other derivatives of thiophene, P3HT is a complementary polymer to PANI. Moreover, both the ECPs show the different primary colors; (P3HT: red/blue and PANI: green/blue) and their union triggers the possibility of different color combinations.

Two conductive transparent electrodes with substrates are used to sandwich the electrolyte and electrochromic layer [74, 29]. One of the widely investigated electrode is silver nanowire (AgNW) with different polymers like polydimethyl siloxane (PDMS) [41], polyimide [44], polyethylene terephthalate (PET) [75] etc due to the high thermal stability and low cost. carbon nano tubes and graphene electrodes are also studied for optoelectronic devices [76]. On the other hand, indium tin oxide (ITO) coated flexible polyethylene terephthalate (PET) is the mostly used electrode material due to low sheet resistance, high transparency, and ease of deposition [77, 78].

There are some parameters given below to measure the electrochromic performance of ECD [35].

Response time: It is the total time required to change the color. It is taken as the 65 % of total transmittance change between two excited states.

Color contrast: It is probably the most important factor in evaluating the ECD. It is the total transmittance change at a specified wavelength where the ECD has highest optical contrast.

$$Color\ contrast(\%) = \frac{(T_1 - T_2)}{T_1} \times 100 \quad (1.1)$$

where T_1 and T_2 are the transmittance of ECDs at different excited states.

Coloration efficiency: It is used to measure the performance of ECD. It tells the amount of charge necessary to produce the optical change.

$$\eta_{ce} = \frac{\Delta OD}{Q} \quad (1.2)$$

where variation of optical density $\Delta OD = A_n - A_e$, A_n and A_e are the absorbance at neutral and excited states, respectively, and Q is the charge density.

Cyclic stability: Cyclic stability is usually associated with electrochemical stability since the degradation of the active redox couple results in the loss of electrochromic contrast and hence the performance of the ECD.

1.3 Self healing in gel electrolyte

Electrolyte is an important layer of ECD on which its performance is critically dependent. It provides ions and ensures a sufficient gap between electrodes. Electrolytes are broadly classified into three types on the basis of phases; liquid, solid and gel electrolytes. Ionic conductivity of electrolyte should be in the range of 10^{-4} - 10^{-3} S/cm for the applicability in ECDs [27, 79]. The ionic conductivity of liquid electrolytes is sufficiently high to be used in the ECD but leakage is its main limitation [27]. Solid electrolyte is used to address this leakage issue by compromising the conductivity followed by improper contact with electrodes [80]. Among these, gel electrolytes (GE) are preferred due to their ease of handling, mechanical properties, sufficiently high ionic conductivity, and better contact issues [29]. GE comprises of salt, solvent, and polymer. Salt consists of ions while solvent provides a medium for the movement of ions. The addition of polymer solidifies and induces the mechanical properties in electrolytes. Different lithium based gel electrolytes are developed using polyvinylidene fluoride (PVDF), [81, 82, 83, 84, 85], polyvinyl chloride (PVC) [86], polyethylene oxide (PEO) [87], poly(vinylidene-fluoride-co-hexafluoropropylene) (PVH) [88], poly(propyl sulfonate dimethylammonium propylmethacrylamide) (PPDP) [89, 90], poly methyl methacrylate (PMMA) [91, 92, 93, 94], poly(ethylene glycol dimethacrylate) (PEGDMA) [95], polyvinyl alcohol (PVA) [96] to achieve the required conductivity. It is to be noted here that ECDs are subjected to repeated coloration-decoloration cycles, varying temperature, humidity and mechanical handling during their service life. These exposures induce damage, cracks, and cuts in GE. It is really difficult if not impossible to repair these cuts/cracks in GE and more often than not, the ECD needs to be replaced. Therefore, it is essential to develop strategies to repair cuts and cracks in GE to enhance the operational life of ECDs. Efforts have been made in this work to induce self-healing capabilities in GE akin to living organisms.

Even though, many studies have reported the use of gel electrolytes in ECDs [81, 82, 83, 87], inducing self-healing capabilities in GE is rather less explored [97]. Few studies have reported the self-healing behavior in hydrogel electrolyte [98, 99, 100]. A blend of glycerol monomethacrylate (GMA) and acrylamide in an aqueous solution of borax and lithium perchlorate shows self-healing by dynamic cross-linking of borate-diol complexation. Borax is used here as a healing agent to crosslink with the GMA [99]. Self-healable polyvinyl alcohol (PVA) based hydrogel electrolyte works on intermolecular hydrogen bonding used in supercapacitor [98]. It requires refrigeration and treatment at room temperature for healing. 1-ethyl-3-methylimidazolium chloride (EMIMCl) requires continuous

water addition to achieve the self-recovery of gel electrolyte [101]. In another study, a poly acrylic acid-based hydrogel with self-healing capabilities is prepared for flexible ECDs [100]. Further, poly(acrylamide) based hydrogel is developed for supercapacitors [102]. Researchers also developed PMMA and poly(acrylic acid) based hydrogels [103, 104]. Although, self-healable hydrogel electrolytes are safe and flexible, solvent volatilization and narrow electrochemical window are the primary issues with them [97]. In addition, water solidification adversely affects their electrochemical performance at low temperatures. Efforts have also been made to prepare self-healable ionogels [105] but they have limitations of high cost and poor mechanical properties [97]. Organic gel electrolytes (organogel) with self-healing characteristics are developed to overcome these drawbacks. Single ion polymer gel electrolyte self-heals by forming the supramolecular networks [106]. Self-healable deep eutectic solvent-based GE is developed for lithium batteries. 2-(3-(6-methyl-4-oxo-1,4-dihydropyrimidin-2-yl)ureido)ethyl methacrylate (UPyMA) is responsible for the healing due to the intramolecular hydrogen bonding [107]. However, the fabrication is tedious and requires blends of multiple polymers for healing. Poly methyl methacrylate (PMMA) shows excellent self-healing behaviour [108, 109, 110] and finds application in preparing capsules for extrinsic healing [111, 112, 113, 114, 115]. Further, it also explored the application in bio-materials [116], coatings [117, 118], dental [119] etc.

1.4 Surrounding detection

Other than developing color-changing hardware, information on surroundings is also required to make it adaptive. Surrounding detection includes the collection of information in terms of color, contrast, texture, etc. Many efforts have been taken in order to collect the information and to make it suitable for the camouflage. Some algorithms are developed to extract the information details of surroundings to prepare the digital camouflage patterns. Mainly, spatial color mixing [120], mathematical morphology [121], two scale decomposition [122], adversarial autoencoder network [123], spot combination [124], color similarity [125], fuzzy C-means clustering [126] and recursive overlapping of pattern templates [127] are used to form the digital camouflage pattern. Majorly, algorithms are worked in two parts in which one part extracts the surrounding information and another one performs the masking. In addition, features of digital images are also used to extract the surrounding information such as contours and surface elements [128] and reflectance of objects [129]. Moreover, facial camouflage patterns are also developed to make the faces hard to detect [130]. Distributed camouflage algorithm enables

the swarm robots to understand the environment [131].

1.5 Key issues

There are some issues which are not addressed in the previous studies. Transparent materials are mainly applicable for underwater applications for camouflaging. It is a very tedious task to achieve transparency for all the associated parts of the land. In addition, dynamic texture change alone is not sufficient for active camouflaging. Materials that are designed to change the texture dynamically have limited application for particular surroundings. There is also a requirement to exhibit color change properties with texture. Other color-changing devices have high input power requirements due to the use of hydraulic and pneumatic actuation. Liquid dyes have a high response time and leakage issue. Other solid color-changing devices do not focus on achieving pattern formation which is one of the important requirements to mimic natural vegetation. Thermochromic materials require a heat source for actuation. Electrochromic devices are suitable to address these issues and to use for this work. They do not focus on to acquire shades of green color. They are also lacking in developing the combination of green and brown color shades which is another requirement of natural vegetation due to the presence of dry leaves, sand, mud, etc. The performance of ECD is degraded due to the cracks and cuts that occur in gel electrolytes. Very limited efforts are made to improve the operational life of ECD by self-repairing gel electrolytes. Hydrogel electrolytes have the issue of water solidification and narrow electrochemical windows. On the other hand, organogels have very tedious fabrication and require different polymers to introduce self-healing. In order to sense the surrounding information details, algorithms do not consider the limitations of hardware therefore they are not useful to integrate with the color-changing materials. These algorithms are mainly for passive camouflage applications like printing and painting.

Even though there are few studies on the design of materials with active camouflage abilities, their applications are rather limited, due to the associated complexity and lack of modularity. Therefore, there is a need to develop a unified solution that is capable of detecting the surroundings and then adapt accordingly to provide effective camouflaging. Developing such a modular strategy using a multitude of analytical and experimental tools is the main objective of the present study. To this end, a detailed study is performed to design, fabricate and characterize a device capable of performing active camouflage in forest surroundings by sensing and adapting accordingly. This concept is realized through the development and integration of an electrochromic modular architecture and the pattern detection

algorithm. An electrochromic device (ECD) is capable of changing the color at different excited states. Its use as a module in a modular system provides the capability for the formation of different patterns. In addition, the concept of an electrochromic modular system provides ease of fabrication, easy replacement, etc. The pattern detection algorithm is used to collect the information surrounding and to make this information suitable for the modular system.

1.6 Objectives

To address these issues, the objectives of the present thesis are defined as,

1. To develop a strategy for self-repairing of gel electrolytes that increases the operational life of electrochromic devices.
2. To develop a technique for acquiring various green shades in electrochromic devices.
3. To develop a method for achieving the combination of green and brown shades in electrochromic devices.
4. To develop an algorithm for the collection of surrounding information and to perform the system integration of algorithm and color changing modular electrochromic devices.

1.7 Organization of thesis

The research work performed in the present thesis is organized into seven chapters. A chapter-wise breakup of the thesis work is as follows,

Chapter 1: Introduction

Chapter 1 provides an introduction to the active camouflage phenomenon and details the motivation of the present study. Extensive literature on recent progress in to design and development the camouflage systems is discussed which includes the development of camouflaging materials, methodologies, and digital patterns. Further, the operating principle and configuration of the electrochromic device are described in detail. Features of green vegetation are also discussed, which are required in the development of pattern detection algorithms and electrochromic modular architecture. This sets the purpose and objectives of the present study to design and fabricate the active camouflage device.

Chapter 2: Materials and methods

Chapter 2 includes various materials, processing methods, and characterization techniques followed in the present study.

Chapter 3: Exploiting self-healing characteristics of polymethyl methacrylate (PMMA) in gel electrolyte

Chapter 3 studies the self-repairing characteristics of electrochromic devices. It discusses the self-healing feature of gel electrolyte layer of ECD. Recovery in tensile strength and ionic conductivity of GE is measured after healing. Further, recovery in color contrast is also tested in ECDs. The optimized weight percentage of PMMA is used subsequently in the fabrication of ECD.

Chapter 4: Modulation of optical properties of electrochromic device

Chapter 4 presents a strategy to develop the shades of green color which is one of the requirements of the present study. It includes the material and device fabrication with detailing of characterization techniques employed.

Chapter 5: Design and fabrication of dual electrochromic device with broader color space

A method is proposed in Chapter 5 to achieve the combination of green and brown color which is another requirement of green vegetation. Two electrochromic polymers are used in this work. It also includes the material and device fabrication with detailing of characterization techniques employed.

Chapter 6: Design and fabrication of modular active camouflage device

Chapter 6 includes the designing, fabrication and testing of proposed active camouflage device which is presented as a proof-of-concept. First, the preparation of electrochromic modular architecture is described in detail. Then, pattern detection algorithm is developed to collect the surrounding information. Further, the system integration is discussed along with the simulation of digital modular architecture, followed by testing of proposed device.

Chapter 7: Conclusions and future scope

Finally, the findings of the study are concluded in Chapter 7. Future prospects of this work are also presented in this chapter.

Chapter 2

Materials and methods

2.1 Materials

Polymethyl methacrylate (PMMA), propylene carbonate (PC) and Poly (3-hexyl thiophene) (P3HT) are purchased from the TCI chemicals and are used as received. Lithium perchlorate (LiClO_4) is purchased from sigma aldrich and heated at 100°C for 30 minutes to remove any moisture content. Aniline and dichlorobenzene are purchased from Loba Chemie. Aniline is first de-oxidized at 150°C and 10^{-2} bar for 2.5 hours before using it for further use. ITO coated flexible PET sheet of specific resistivity $15\Omega/\text{sq}$ and transmittance $> 75\%$ is purchased from Techinstro ltd.

2.1.1 Gel electrolyte (GE)

Gel electrolyte is prepared following the fabrication steps shown in Figure 2.1. In the first step, liquid electrolyte (LE) is prepared by adding 1.5 M of LiClO_4 in PC solution. Mixing is performed at 80°C and 400 rpm for 30 minutes. Next, PMMA is added in the LE and the solution is stirred at 450 rpm for 8 hours. After stirring, solution is degassed in vacuum for 4 hours. The solution is then poured in 10 cm x 4 cm x 2 mm size silicon mold cavity. Cavity is prepared on the glass slide to avoid the stickiness with surface. 15 % PMMA is used for the fabrication of ECD while 15 %, 25 %, 35 % and 50 % PMMA is used for the self healing tests. The mold is placed in vacuum for 4 hours to remove trapped air and then allowed to cure in atmospheric conditions for 20 days (refer Figure 2.1)) before testing. Four types of GE are prepared by varying the weight percent of PMMA in the range of 15%, 25%, 35% and 50% to prepare GE15, GE25, GE35 and GE50 respectively which are used for self healing tests. While GE15 is used for the fabrication of ECD.

2.1.2 Preparation of PANI and P3HT electrochromic polymers

Polyaniline (PANI) is prepared by the electropolymerization process using the cyclic voltammetry (CV) technique. Electropolymerization is performed in three-electrode electrochemical cells with ITO as the working electrode, platinum as the counter

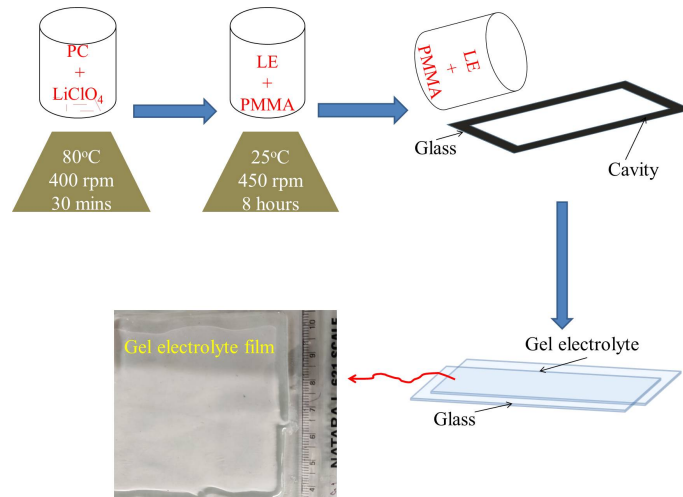


Figure 2.1: Processing steps followed for fabrication of gel electrolyte.

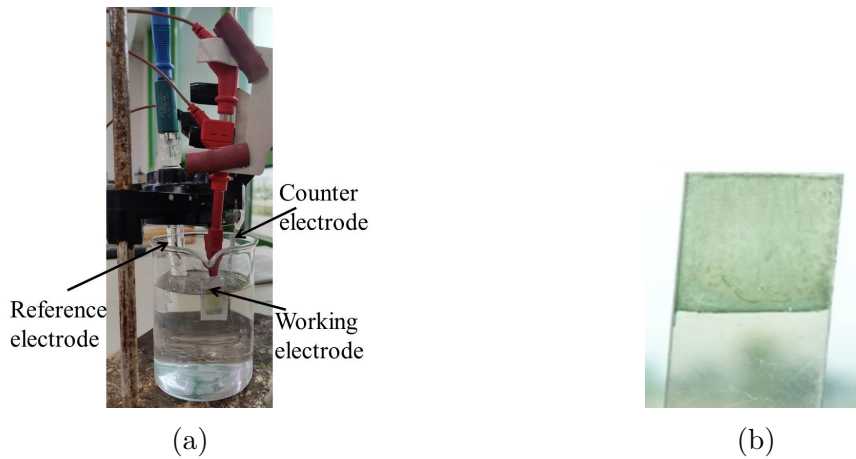


Figure 2.2: (a) Photographic image of electrochemical set up used for electrochemical polymerization of polyaniline (PANI) and (b) green color polyaniline (PANI) film on ITO/PET sheet after electro polymerization process

electrode, and Ag/AgCl as the reference electrode (Fig. 2.2a). For the electropolymerization of PANI, a monomer solution is prepared by mixing the 0.2 M of distilled aniline in 0.2 M H_2SO_4 in DI water followed by the sonication for 45 minutes to uniformly mix the solution. ITO/PET sheet is cleaned by rinsing in a 1:1 mixture of ethanol and acetone followed by DI water [132] before dipping into the monomer solution. ITO side is faced towards the platinum plate at a distance of 5 cm. The potential is applied for 5, 10, 15, and 20 CV cycles to get different thicknesses of PANI for the study of shades in Chapter 4. In each cycle, potential sweeps from -0.2 V to 1.0 V to -0.2 V linearly at a scan rate of 50 mV/s. After the deposition, PANI film is rinsed with DI water to remove the unreacted monomer and oligomer followed by drying in open air [133]. The green color on the ITO substrate after the electropolymerization process confirms the presence of an

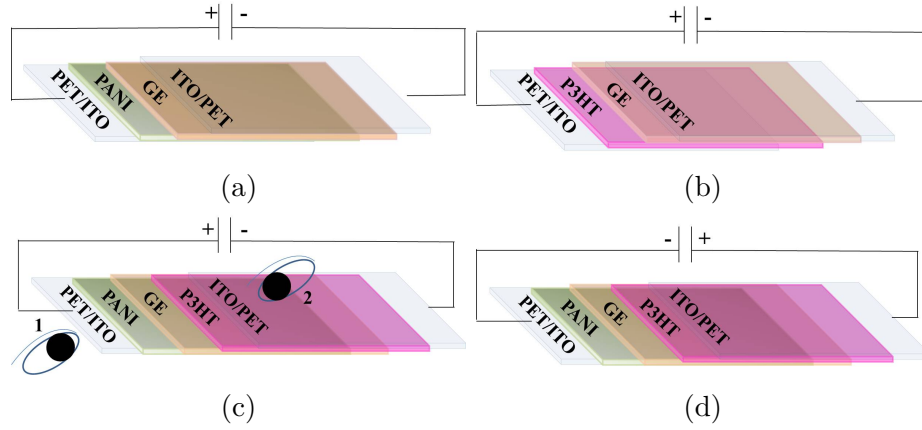


Figure 2.3: Schematic of different electrochromic devices (ECD) showing architecture of (a) ECD1(PET/ITO/PANI/GE/ITO/PET), (b) ECD2(PET/ITO/P3HT/GE/ITO/PET), (c) ECD3(PET/ITO/PANI/GE/P3HT/ITO/PET) showing side 1 and side 2 to take the separate measurements from both sides and (d) ECD4(PET/ITO/PANI/P3HT/GE/ITO/PET).

emeraldine form of PANI as shown in Fig. 2.2b. Poly (3-hexyl thiophene) (P3HT) is used as received for the spin coating on the electrode. 0.9 wt % of P3HT is added to the dichlorobenzene and stirred manually to use the solution for spin coating. It is spin-coated at 450 rpm for 90 s. P3HT is coated on the ITO side of the ITO/PET sheet for the fabrication of single ECD and complementary dual ECD and on PANI film for the hybrid dual ECD.

2.1.3 Fabrication of single and dual electrochromic devices

For this work, four types of electrochromic devices are prepared of which two are PANI and P3HT-based single ECDs and two are dual ECDs using PANI and P3HT simultaneously. For the complementary dual ECD, both the electrochromic polymers are deposited on the opposite electrodes and the same electrode for the complementary and hybrid dual ECD. After the preparation of electrochromic polymers, a 450-micron-deep cavity is created using acrylic double-sided tape to fill the GE. A cavity is created on a PANI-coated ITO/PET sheet for the fabrication of PANI-based single ECD (ECD1) and complementary dual ECD (ECD3). For the P3HT single ECD (ECD2) and hybrid dual ECD (ECD4), the cavity is prepared on P3HT coated ITO/PET sheet and PANI/ITO/PET sheet, respectively. After filling, the GE, ECD1, ECD2, and ECD4 ECDs are covered by another ITO/PET while ECD3 dual ECD is covered with P3HT coated ITO/PET sheet. Then, it is allowed to be cured for 1 week before characterization. The architecture of ECD1, ECD2, ECD3, and ECD4 ECDs are PET/ITO/PANI/GE/ITO/PET, PET/ITO/P3HT/GE/ITO/PET, PET/ITO/PANI/GE/P3HT/ITO/PET and

PET/ITO/PANI/P3HT/GE/ITO/PET. Further connections on the ITO electrode are made with copper tape and conductive silver paste for testing.

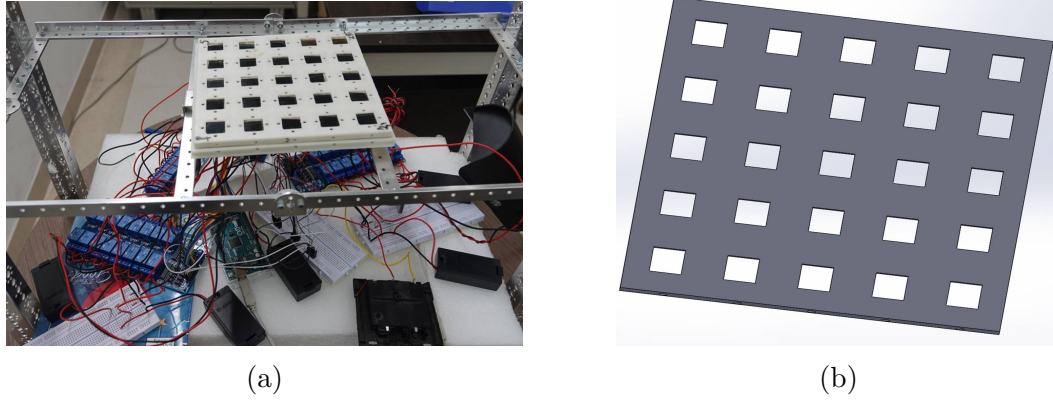


Figure 2.4: (a) Setup of active camouflage device showing electrochromic modular architecture with integrated circuit and (b) casing of electrochromic modular architecture contains 25 cavities prepared on the solid-works.

2.1.4 Active camouflage device

Active camouflage device consists of two units; pattern detection algorithm (PDA) and Pattern formation hardware (PFH). PDA is developed on MATLAB to collect the surrounding information and to process it to form a Modular image (MoI). On the other hand, PFH generates the patterns accordingly with the help of electrochromic modular architecture (MoE_A). MoE_A is prepared using the combinations of different ECDs (Figure 2.4a). The frame is modeled on the Solidworks as shown in Figure 2.4b and fabricated on the 3-D printer using PLA material. The frame consists of 25 (5 x 5) cavities for ECD of size 1.5 cm x 1.5 cm each. ECDs are fixed in the cavities using hot glue. On the other hand, a pattern detection algorithm (PDA) is developed in MATLAB. MoI and MoE_A are integrated using Arduino MEGA 2560 for controlling, relays for switching the potential, 1.5 V Duracell batteries (2 batteries in series), resistors, and bread-boards. Arduino is controlled by MATLAB using a hardware supporting package for Arduino. Initially, the bare ITO side of ECDs is kept at ground state and potential is applied on the ECP side.

2.2 Characterizations

Cyclic Voltammetry (CV), Electrochemical Impedance Spectroscopy (EIS), and chronoamperometry are performed on an electrochemical workstation (Metrohm Multi autolab M204, Netherlands). CV is used to evaluate the redox behavior of ECD in the potential range of -2.5 V to 2.5 V at the scanning rate of 20 mV/s and step potential of 2.44 mV. EIS is an electrochemical technique used to study the ion conduction mechanism in ECD. Data is recorded in the form of real and complex impedance for the applied frequency range of 0.1 - 10^5 Hz. AC conductivity (σ) is measured using $\sigma = l/(R \times A)$, where ' R ' is the intercept of the curve on the x-axis (real impedance), ' l ' is the distance between electrodes and ' A ' is the cross-sectional area of the electrode. Measurements, post analysis and curve fittings are performed on software NOVA 2.1. All the experiments are carried out in potentiostatic mode. Chronoamperometry is performed to evaluate the cyclic stability. By varying the redox potentials, a change in current density is recorded with time. Characterization of ECD is performed using a two-electrode configuration in which PANI/ITO and P3HT/PANI/ITO are used as working electrodes and ITO on another side is used as a counter electrode.

Atomic force microscopy (AFM) (Bruker, USA) analysis is performed in tapping mode on a scan area of $5 \mu\text{m} \times 5 \mu\text{m}$ to measure the thickness and surface roughness of electrochromic films. Peak force and deformation measurements at cross-section of PANI and PANI-P3HT films are performed in contact mode. Surface morphology is studied with a scanning electron microscope (SEM) (Jeol 6610LV Japan) and FESEM (Jeol JSM-7610FPlus). Absorptance, transmittance and reflectance spectra of PANI are recorded (PerkinElmer LAMBDA 950 UV/Vis/NIR spectrophotometer, USA) in the range of 380 nm – 780 nm. Spectroelectrochemical measurements of ECDs are performed with an in-situ UV-Vis spectrophotometer (Cary 60 of Agilent) electrochemical workstation (Keithley 2450).

Fourier transform infrared spectroscopy (FTIR) measurements are performed in the range of 400 cm^{-1} to 4000 cm^{-1} with Bruker Optik spectroscope. Dynamic mechanical analysis (DMA) is carried out to determine the glass transition temperature (T_g) using the DMA-1 star system (METTLER TOLEDO) under shear mode. Tensile tests are performed on the mini-universal testing machine (SHIMADZU EZ-LX). A 5 N load cell is used and a minimum of 3 samples of size 10 mm x 4 mm x 2 mm are tested for each case at the strain rate of 5 mm/min at room temperature [84]. Digital images are captured by the camera (Sony - RX10) using ISO 640 at a shutter speed of $\frac{1}{100}$ s and aperture F3.2 while microscopic images are taken with a Dinolite USB camera. All the curves are plotted in MATLAB.

Next, the efficiency of self-healing process is characterized by performing the tensile

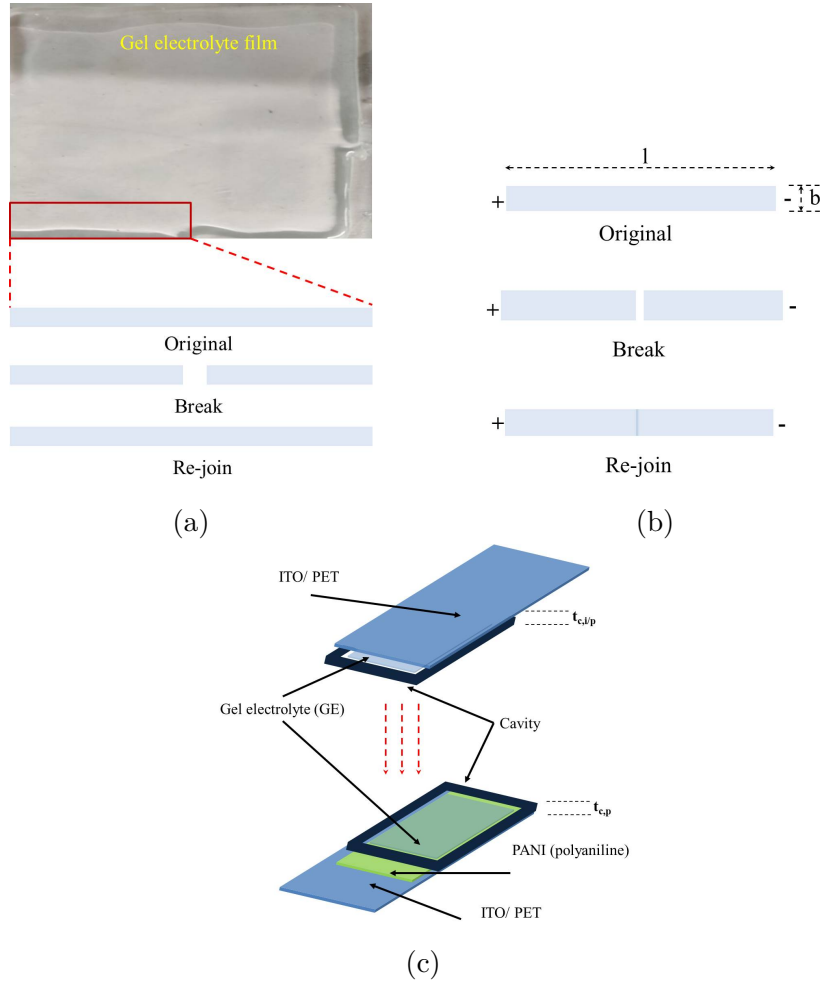


Figure 2.5: Schematic showing original and healed GE specimens for (a) tensile test, (b) ionic conductivity test and (c) electrochromic device.

testing and ionic conductivity measurements on original and healed GE samples. To this end, identical specimens are taken from the GE sheet. While the original samples are kept as such, a few samples are cut in two halves and placed side by side keeping their cut ends touching each other as shown in Figure 2.5. These samples are allowed to self-heal for 10 min, 30 min, 1 hour, 2 hours and 6 hours. The tensile test (Figure 2.5a) and ionic conductivity (Figure 2.5b) of original and self-healed samples are measured following the details described earlier.

To investigate the healing efficiency at the device scale, the optical and color contrast analysis of ECDs prepared using original and self-healed GE15 is also compared. Since it is relatively difficult to cut the GE exactly from mid-plane and perform self-healing experiments, the two 300 microns thick GE layers (one on the PANI side of the PANI/ITO sheet and another on the ITO side of the ITO/PET sheet) are prepared. They are then allowed to self-heal for 10 min and 6 hours and the self-healed GE layer of 600 microns thickness is used to fabricate ECD shown in Figure 2.5c.

Chapter 3

Exploiting self healing characteristics of polymethyl methacrylate (PMMA) in gel electrolyte for application in electrochromic devices

In line with the first objective of this proposed work, self-healing is induced in gel electrolytes to increase the operational life of ECD. In this chapter, the healing properties of poly methyl methacrylate (PMMA) are investigated and exploited, including the fabrication and characterization of GE with self-healing capabilities. Comparative mechanical and electrochemical analysis of original and healed GE samples is performed to determine the optimum PMMA concentration and healing time. Experimental results show that the GE with 15 wt % of PMMA (GE15) recovers 98% of its mechanical strength within 10 minutes of healing time. The ionic conductivity of healed samples is found to be the same as that of the original sample at all PMMA concentrations and healing times. It is observed that the healing time, viscosity, number of uncoiling polymer chains, and mobility of Li^+ ions critically influence the healing efficiency of GE. The color contrast analysis of ECD fabricated with original and healed GE is performed to demonstrate the applicability of self-healable GE. It is recorded that for longer healing time, the color performance of self-healed ECD approaches to that of original ECD.

3.1 Introduction

Electrochromic devices (ECD) change color on the application of voltage. They find application in flexible displays [134], smart textiles [135, 134], smart windows [136], energy storage [137, 138] etc. In an ECD, the electrolyte layer is sandwiched between two conductive electrodes [74, 29]. While indium tin oxide (ITO) coated polyethylene terephthalate (PET) and glass sheets act as conductive electrodes,

liquid, as well as semi-solid electrolytes with varying chemical compositions, have been used in ECDs. Among these, gel electrolytes (GE) are preferred due to their ease of handling, mechanical properties, and sufficiently high ionic conductivity. GE consists of salt, solvent, and polymer. Salt provides the ions while solvent acts as a medium for ion movement. The addition of polymer solidifies the electrolyte and improves its mechanical strength. The use of GE also avoids the leakage and contact issues associated with the liquid electrolytes [29] and solid electrolytes [139, 140] respectively. It is to be noted here that ECDs are subjected to repeated coloration-decoloration cycles, varying temperature, humidity, and mechanical handling during their service life. These exposures induce damage, cracks, and cuts in GE. It is really difficult if not impossible to repair these cuts/cracks in GE and more often than not, the ECD needs to be replaced. Therefore, it is essential to develop strategies to repair cuts and cracks in GE to enhance the operational life of ECDs. Efforts have been made in this work to induce self-healing capabilities in GE akin to living organisms.

Even though, many studies have reported the use of gel electrolytes in ECDs [81, 82, 83, 87, 141, 142, 143, 144], inducing self healing capabilities in GE is rather less explored [97]. Few studies have reported the self-healing behavior in hydrogel electrolyte [98, 99, 100]. A blend of glycerol monomethacrylate (GMA) and acrylamide in an aqueous solution of borax and lithium perchlorate shows self-healing by dynamic cross-linking of borate-diol complexation. Borax is used here as a healing agent to crosslink with the GMA [99]. Self-healable polyvinyl alcohol (PVA) based hydrogel electrolyte works on intermolecular hydrogen bonding used in supercapacitor [98]. It requires refrigeration and treatment at room temperature for healing. In another study, a poly acrylic acid-based hydrogel with self-healing capabilities are prepared for flexible ECDs [100]. Although, self-healable hydrogel electrolytes are safe and flexible, solvent volatilization and narrow electrochemical window are the primary issues with them [97]. In addition, water solidification adversely affects their electrochemical performance at low temperatures. Organic gel electrolytes (organogel) with self-healing characteristics are developed to overcome these drawbacks. Single ion polymer gel electrolyte self-heals by forming the supramolecular networks [106]. Self-healable deep eutectic solvent-based GE is developed for lithium batteries. 2-(3-(6-methyl-4-oxo-1,4-dihydropyrimidin-2-yl)ureido)ethyl methacrylate (UPyMA) is responsible for the healing due to the intramolecular hydrogen bonding [107]. However, the fabrication is tedious and requires blends of multiple polymers for healing.

Poly methyl methacrylate (PMMA) shows excellent self-healing behaviour [108, 109, 110] and has been used in bio-materials [116], coatings [117, 118] etc. However, to the best of our knowledge, the self-healing capabilities of PMMA are not yet exploited

in GE developed for ECDs. Therefore, the focus of this study is to evaluate the self-healing behavior of PMMA-based gel electrolytes. Due to the high mobility and small size of lithium-ion, lithium perchlorate salt is used to fabricate GE. Propylene carbonate (PC) is used as a solvent due to its low molecular weight, high dielectric constant, and non-volatile behavior. PMMA polymer is used to provide mechanical strength to PC and self-healing characteristics to GE. The concentration of PMMA in PC is optimized through well-designed healing experiments to strike a balance between mechanical strength, ionic conductivity, healing rate, and healing efficiency. It is shown that the GE layer having an optimum concentration of PMMA recovers more than 90 % of its strength and conductivity in about 10 mins. To characterize the effect of self-healing, a comparative color contrast analysis is performed on ECDs fabricated using the original and self-healed GE layer. It is recorded that the color contrast of ECDs having self-healed layers decreases in comparison to ECDs prepared using the original GE layer. Moreover, self-healing is achieved at room temperature without any external stimulus or healing agent. It is envisaged that the finding of the present study will be helpful to fabricate ECDs that are capable to self self-healing and thus have better service life.

3.2 Experimental

3.2.1 Materials and preparation

GE is prepared following the fabrication steps shown in Figure 2.1. Poly methyl methacrylate (PMMA) (Average $M_W = 35000$) and propylene carbonate (PC) are purchased from TCI chemicals and are used as received. Lithium perchlorate (LiClO_4) is purchased from Sigma Aldrich and heated at 100°C for 30 minutes to remove any moisture content. GE is fabricated in two steps. In the first step, liquid electrolyte (LE) is prepared by mixing 1.5 M LiClO_4 salt in PC solvent at 80°C and 400 rpm for 30 mins. After cooling down, PMMA is added to the LE solution and stirred at 450 rpm for 8 hours in the second step. The solution is then poured into 10 cm x 4 cm x 2 mm size silicon mold cavity to prepare the gel electrolyte layer. The mold is placed in a vacuum for 4 hours to remove trapped air and then allowed to cure in atmospheric conditions for 20 days (see Figure 2.1) before testing. To determine the optimum concentration, PMMA weight percent in GE is varied in the range of 15%, 25%, 35%, and 50% to prepare GE15, GE25, GE35, and GE50 respectively.

ECD is fabricated following the procedure reported in an earlier study [145]. 0.2 M of distilled aniline is added to 0.2 M of H_2SO_4 and the mixture is sonicated for 45 minutes to perform the electro-polymerization using cyclic voltammetry. ITO/PET

sheet is dipped in the monomer solution and potential is applied for 20 CV cycles in the range of -0.2 V to 1.0 V at a scan rate of 50 mV/s. After electro-polymerization, the green color on the ITO substrate confirms the formation of the PANI layer. A 600-micron-deep cavity is created on the PANI-coated ITO/PET sheet using acrylic double-sided tape. A cavity is filled with uncured GE15 and covered by the ITO/PET sheet on the other side. Then ECD is allowed to cure for 1 week before characterization.

3.2.2 Characterization

Fourier transform infrared spectroscopy (FTIR) measurements are performed in the range of 400 cm^{-1} to 4000 cm^{-1} with Bruker Optik spectroscope. Dynamic mechanical analysis (DMA) is carried out to determine the glass transition temperature (T_g) using the DMA-1 star system (METTLER TOLEDO) under shear mode. Tensile tests are performed on the mini-universal testing machine (SHIMADZU EZ-LX). A 5 N load cell is used and a minimum of 3 samples of size 10 mm x 4 mm x 2 mm are tested for each case at the strain rate of 5 mm/min at the room temperature [84]. Ionic conductivity is measured using,

$$\lambda_{ionic} = \frac{l}{R_b A} \quad (3.1)$$

where l is the distance between electrodes, A is the area of cross-section and R_b is the bulk resistance of the GE sample. R_b is measured in the frequency range of 60 Hz to 10^5 Hz at 1 V using LCR meter. Cyclic Voltammetry (CV) is performed on an electrochemical workstation (Metrohm Multi autolab M204, Netherlands). CV is used to evaluate the redox behavior of ECD in the potential range of -2.5 V to 2.5 V at the scanning rate of 20 mV/s and step potential of 2.44 mV. Data is recorded on Nova 2.1 while all the curves are plotted on MATLAB. Digital images are captured by a camera (Sony - RX10) using ISO 640 at a shutter speed of $\frac{1}{100}$ s and aperture F3.2 while microscopic images are taken with a Dinolite USB camera. Next, the efficiency of self-healing process is characterized by performing the tensile testing and ionic conductivity measurements on original and healed GE samples. To this end, identical specimens are taken from the GE sheet. While the original samples are kept as such, a few samples are cut in two halves and placed side by side keeping their cut ends touching each other as shown in Figure 2.5a. These samples are allowed to self-heal for 10 min, 30 min, 1 hour, 2 hours, and 6 hours. The tensile test (Figure 2.5a) and ionic conductivity (Figure 2.5b) of original and self-healed samples are measured following the details described earlier. To investigate the healing efficiency at the device scale, the optical and color contrast analysis of ECDs prepared using original and self-healed GE15 is also compared. Since it is relatively

difficult to cut the GE exactly from mid-plane and perform self-healing experiments, the two 300 microns thick GE layers (one on the PANI side of the PANI/ITO sheet and another on the ITO side of the ITO/PET sheet) are prepared. They are then allowed to self-heal for 10 min and 6 hours and the self-healed GE layer of 600 microns thickness is used to fabricate ECD shown in Figure 2.5c.

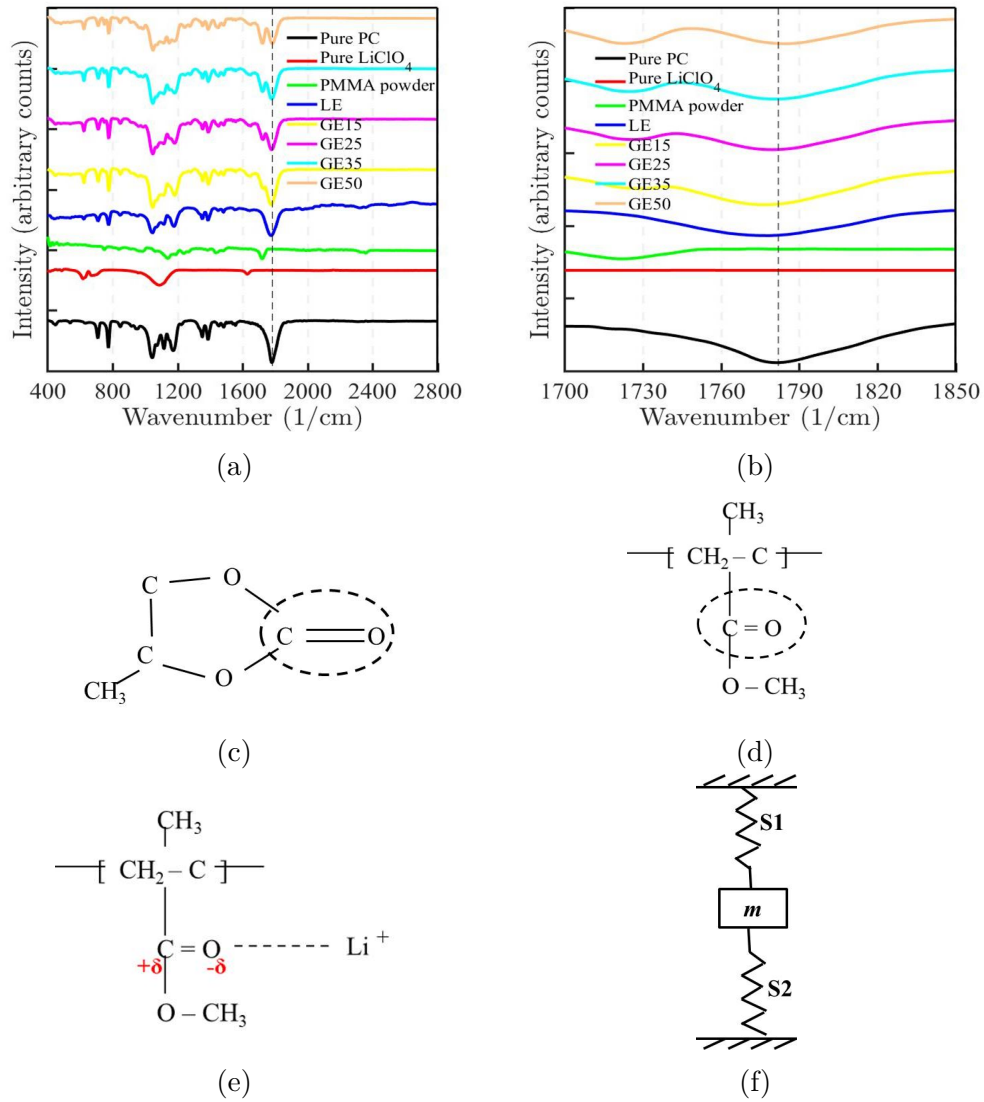


Figure 3.1: (a)FTIR curve and (b) its zoomed view comparing pure PC, pure LiClO₄, PMMA powder, liquid electrolyte (LE), GE15, GE25, GE35, and GE50 in the range of 400 - 2800 cm⁻¹ and 1700 - 1850 cm⁻¹ respectively. Molecular structure of (c) PC and (d) PMMA. Schematic showing the (e) Li⁺ - PMMA interaction and (f) spring-mass system represents m as Li⁺, S1 and S2 as (C=O) group of PC and PMMA respectively.

3.3 Results and discussion

3.3.1 Fourier transform infrared spectroscopy (FTIR)

FTIR measurements of all GEs with PMMA powder, pure LiClO_4 , pure PC, and liquid electrolyte (LE) are compared in Figure 3.1a and its zoomed view in the range of $1700 - 1850 \text{ cm}^{-1}$ is shown in Figure 3.1b. Stretching of the carbonyl (C=O) group in PC is associated with the vibrational frequency of 1782 cm^{-1} [146] (Figure 3.1c). This band shifts to 1775 cm^{-1} in LE ($\text{LiClO}_4 + \text{PC}$) due to the interaction of lithium-ion and carbonyl group of PC ($\text{Li}^+ - \text{PC}$) [146, 147]. After adding varying weight fractions of PMMA, this peak is shifted from 1775 cm^{-1} to 1778 , 1782 , 1784 , and 1788 cm^{-1} for GE15, GE25, GE35, and GE50 respectively. It indicates that the $\text{Li}^+ - \text{PC}$ interaction weakens due to the presence of another interaction between Li^+ and the C=O group of PMMA (Figure 3.1d). Stronger interaction of Li^+ and C=O group of PMMA (Figure 3.1e, ($\text{Li}^+ - \text{PMMA}$)) may be due to the higher electro-negativity of 'O' of C=O group in PMMA than 'O' of C=O group in PC. Therefore, peak upshifts with the increase in PMMA amount. These observations may also be understood by replacing the chemical interactions with the spring (S) and mass (m) system. Carbonyl group of PC and PMMA may be assumed as springs S_1 and S_2 . The natural frequency (f) (wavenumber) of the interaction depends on the stiffness k (directly proportional) and mass m (inversely proportional). The natural frequency f of S_1 (C=O of PC) decreases after the addition of m (Li^+) that is manifested in the downshift of C=O peak in LE (Figure 3.1). However, in the presence of S_2 (C=O of PMMA), the average stiffness of the system (Figure 3.1f) increases, and hence we observe an upshift in the natural frequency of C=O bond stretching in FTIR analysis in Figure 3.1b. Apart from these, some other types of interactions such as salt-polymer ($\text{Li}^+ - \text{PMMA}$) interaction, and dipole-dipole ($\text{PMMA} - \text{PMMA}$) interaction among the polymer chains may also contribute towards shifting of C=O peak [94, 87]. However, it is difficult to explicitly identify them in the FTIR analysis due to the overlapping of spectral contribution from the carbonyl groups of PMMA and PC.

3.3.2 Effect of PMMA on the glass transition temperature of GE

It is reported that thermoplastics like PMMA shows excellent self healing behaviour above their glass transition temperature (T_g) [97]. Therefore, T_g of different GE compositions is measured by performing the temperature sweep in DMA. The temperature is varied in the range of -100°C to 25°C at $3^\circ\text{C}/\text{min}$ and 1 Hz frequency.

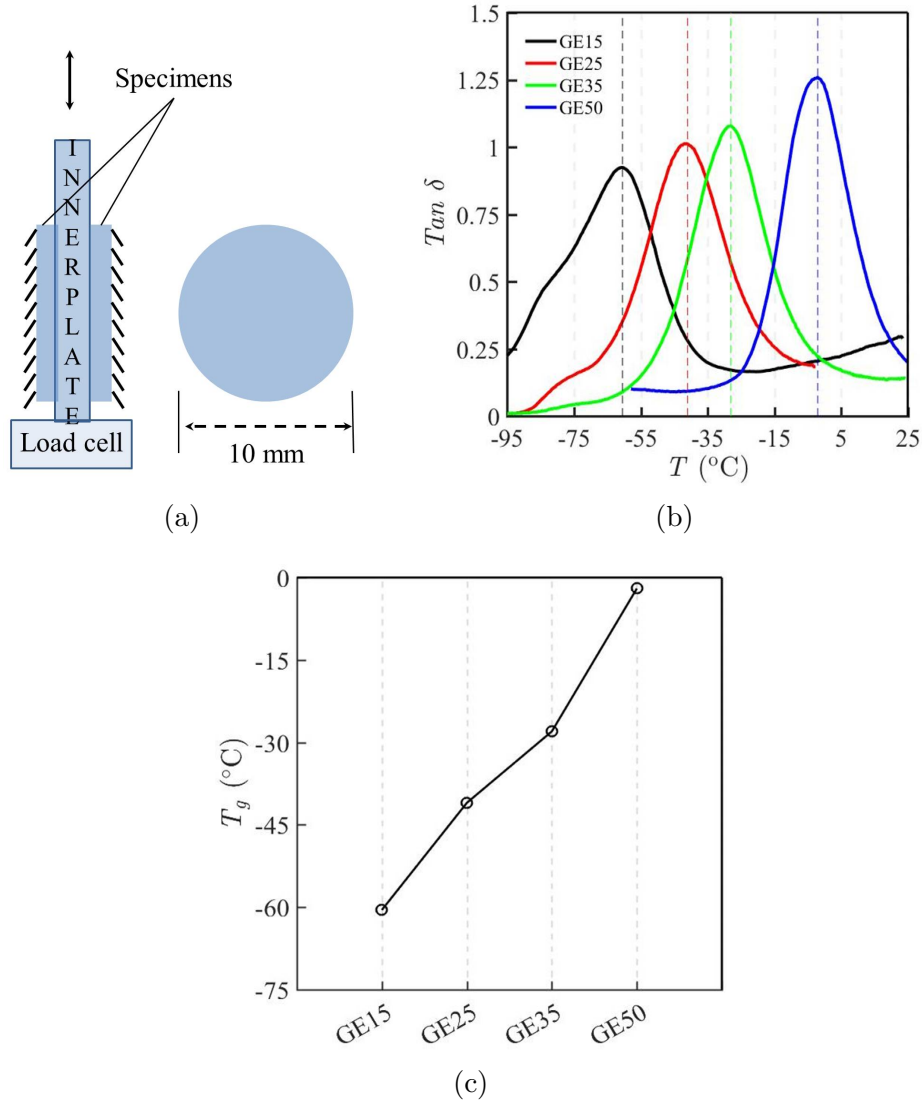


Figure 3.2: (a) Loaded sample for shear test in DMA to perform the temperature sweep, (b) $Tan \delta$ vs temperature curves and (c) Glass transition temperature (T_g) of GE15, GE25, GE35 and GE50.

GE50 is tested from -55°C to 25°C to avoid the exceeding of DMA load cell limit. Two specimens of 10 mm diameter and 2 mm thickness are cut from the gel electrolyte layer and placed on both sides of the plate attached to the load cell (Fig 3.2a) to obtained the $Tan \delta$ curves. The glass transition temperature of GEs is measured from the peak of their respective $Tan \delta$ (Figure 3.2b) curves and compared in Figure 3.2c. It shows that T_g increases from -60.5°C for GE15 to -2°C for GE50 on increasing the the PMMA concentration in GE samples. It may be attributed to the higher viscosity of GE samples containing larger amount of PMMA (or lower concentration of PC solvent). Moreover, the T_g of PMMA is reported to be in the range of $105^{\circ}\text{C} - 120^{\circ}\text{C}$. Thus, increasing the concentration of PMMA in GE enhances their T_g following the ‘rule-of-mixture’ principle.

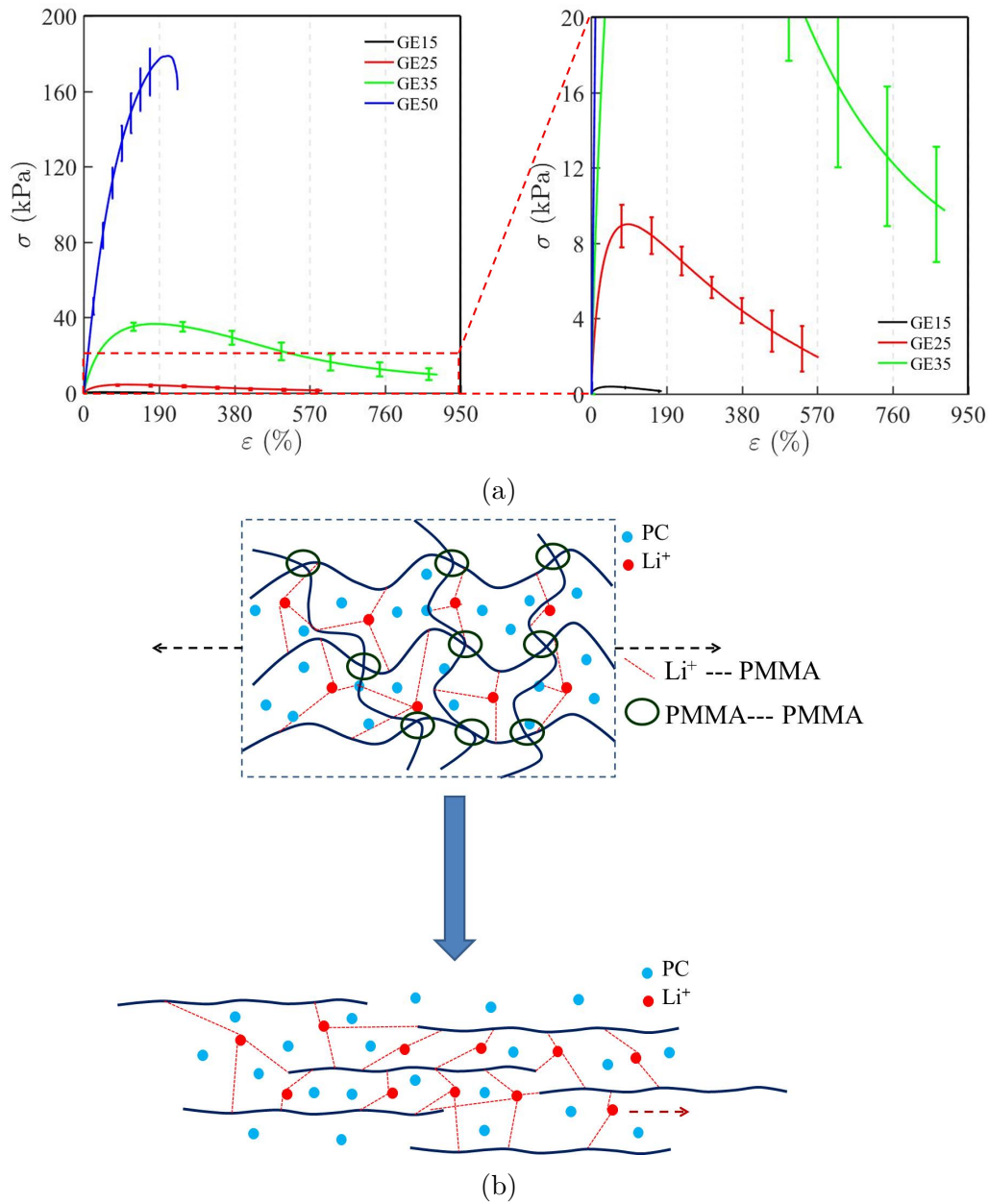


Figure 3.3: (a) $\sigma - \epsilon$ curve of GE as a function of PMMA wt% and its zoomed view. (b) Schematic showing the uncoiling of PMMA chains on the application of tensile load.

3.3.3 Effect of PMMA on the mechanical properties and self healing behavior of GE

Since the self-healing phenomenon is related to the diffusion of ions and re-bonding, it is expected that the stiffness (or viscosity) may influence the self-healing characteristics of the prepared GE. Therefore, tensile testing is carried out to characterize the effect of PMMA addition on the average mechanical properties of GE before self-healing experiments. Figure 3.3 compares the $\sigma - \epsilon$ curves for GE

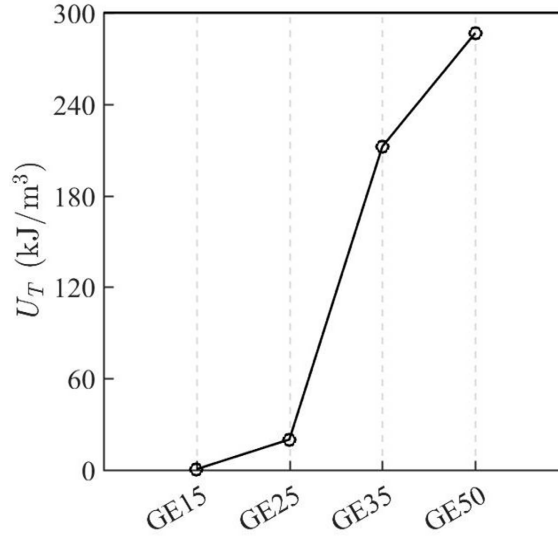


Figure 3.4: Variation in toughness modulus of GE as a function of PMMA concentration.

samples as a function of PMMA concentration. The zoomed view for GE15 and GE25 samples is also included for better clarity. It shows that the modulus (slope of the initial part of $\sigma - \varepsilon$ curves) and tensile strength of GE increases with the addition of PMMA. The tensile strength improves monotonically from 0.4 kPa for GE15 to 178.8 kPa for GE50. Being the stiffer component, the increase in PMMA concentration enhances the tensile strength of GE.

Unlike the variation of tensile strength, the elongation at break first increases from 180 % for GE15 to 890 % for GE35 but then it reduces significantly to 230 % for GE50. Thus, there is an optimum concentration of PMMA to exploit its self-healing properties in GE. The maximum elongation in GE samples is primarily related to the mobility of Li^+ —PMMA crosslinks and uncoiling of PMMA chains as schematically shown in Figure 3.3b. The number of uncoiling chains and movable crosslinks increases on increasing the PMMA up to 35 wt% and results in larger elongation at break. However, on further increasing the PMMA to 50 %, the density of movable Li^+ —PMMA crosslinks decreases and the viscosity of GE increases. The elongation of GE is dominated by stiffer and heavier PMMA—PMMA interaction. In addition, the bulky and dense side chains of PMMA restrict the conformational relaxation (backbone rotation and bending) [148]. A combination of all these factors may reduce the elongation at the break of GE50 samples. Modulus of toughness (U_T) is another important parameter to characterize the mechanical behavior of GE and it reveals the energy absorbing capacity of the GE per unit volume before fracture. U_T is obtained from the area under the $\sigma - \varepsilon$ curves presented in Figure 3.3 and compared in Figure 3.4. It is found to be 0.5 kJ/m³, 20 kJ/m³, 212.2 kJ/m³ and 286.7 kJ/m³ for GE15, GE25, GE35 and GE50 respectively. It follows the variation

of tensile strength with PMMA concentration and shows that stiffer GE samples are able to absorb higher energy before failure.

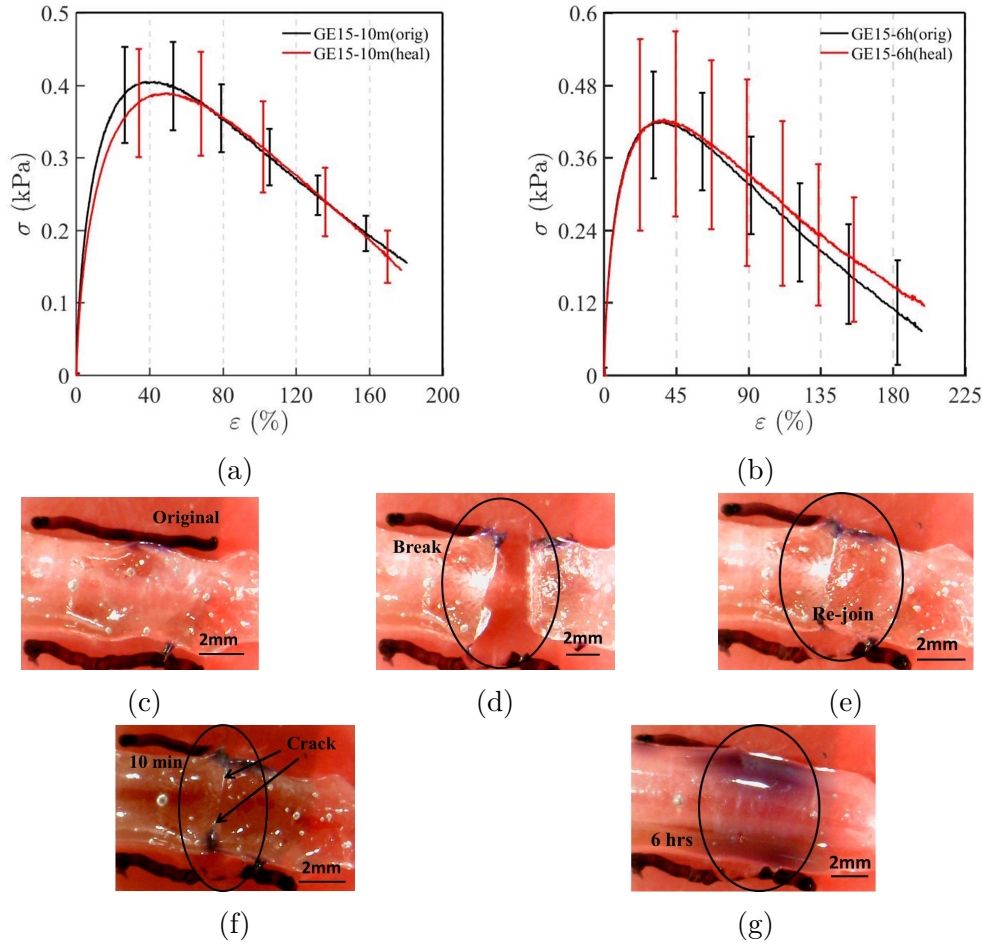


Figure 3.5: Comparative σ - ϵ curve of original and healed specimen of GE15 for (a) 10 min and (b) 6 hours healing time. Optical images of GE15 as (c) original, (d) after break, (e) after rejoin, (f) after 10 mins and (g) 6 hours of healing.

After evaluating the mechanical properties of GE, self-healing experiments are performed following the procedure outlined in the characterization section. Specimens are cut into two pieces and are allowed to rejoin (or heal) by putting their cut ends in contact as shown in Figure 2.5a. The healing time is varied for 10 min, 30 min, 1 hour, 2 hours, and 6 hours to understand the self-healing process and time required for efficient self-healing of different GE samples. To minimize the effect of environmental factors, two specimens, one without cut and one after cut, are kept together for the same time under the same conditions before their testing. The sample without cut is labeled original and the other samples are labeled as healed in comparative plots. Minimum 3 tests are conducted for each case and their average is used in comparative analysis. Figure 3.5a and 3.5b show the comparison of σ - ϵ curves for original and healed GE15 after 10 min and 6 hours of healing time respectively. Even though, all the experiments are performed at the same

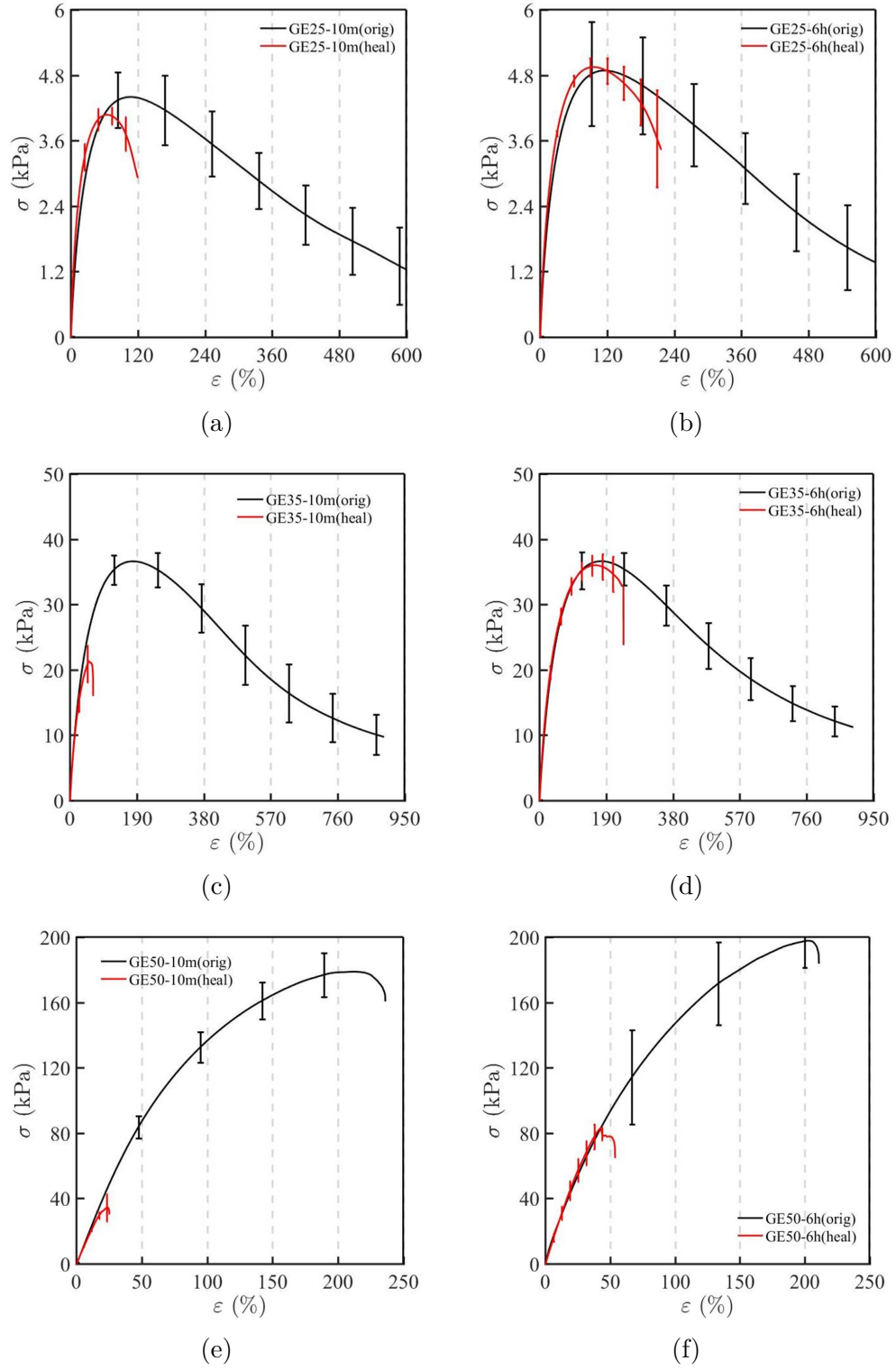


Figure 3.6: Comparing σ - ϵ curve of original and healed specimens of GE25, GE35 and GE50 at healing time of (a, c, e) 10 min and (b, d, f) 6 hours respectively.

atmospheric conditions, a large standard deviation among one type of samples is recorded in Figure 3.5 and 3.6. This may be due to the fact that the healing process may initiate at different sites in different samples. While the tensile strength of the healed sample is slightly lower for 10 mins healing time, the GE15 sample shows complete recovery of tensile strength for 6 hrs healing time. Self-healing experiments are performed at room temperature which is above the T_g of all GEs (Figure 3.2c). The healing occurs primarily due to the diffusion and reptation of PMMA chains at the joined interface [149, 150, 110]. In addition, the diffusion of Li^+ at the interface also contributes to the healing. While Li^+ —PMMA interaction can be viewed as dynamic and reversible cross-links which are beneficial for the self-healing [97], new physical cross-links (Li^+ —PMMA) are formed at the healed interface and contribute to the strength of the healed sample. Thus, 10 minutes of healing time is not sufficient for GE15 samples to regain their strength and the healing is found to be more effective for 6 hours of healing time. The optical micrographs of GE 15 in Figure 3.5c - 3.5g show a similar trend with partial healing for 10 min and complete healing for 6 hrs healing time. Contrary to GE15, the mechanical behavior of healed GE25, GE35, and GE50 samples is slightly different. Even though, all these samples show better strength recovery for a larger healing time of 6 hrs, their tensile strength and failure strain reduce at higher PMMA wt% in Figure 3.6a – 3.6f.

The healing time dependent recovery of tensile strength (Figure 3.7a) and elongation (Figure 3.7b) for different GE samples is compared in Figure 3.7. The percentage of strength $\sigma_{recovery}$ and elongation at break $\varepsilon_{recovery}$ recovery is calculated as follows,

$$\sigma_{recovery}(\%) = \frac{\sigma_{max(healed)}}{\sigma_{max(orig)}} \times 100 \quad (3.2)$$

$$\varepsilon_{recovery}(\%) = \frac{\varepsilon_{max(healed)}}{\varepsilon_{max(orig)}} \times 100 \quad (3.3)$$

Figure 3.7a reveals that all healed samples are able to recover higher strength for a longer healing time. Moreover, at a given healing time, the relative gain in strength decreases with PMMA concentration. GE50 sample shows only 19% recovery at 10 min healing time which is lowest among all the samples tested here. GE15 and GE25 recovers completely followed by GE35 (95%) and GE50 (45%) after 6 hrs of healing time. Thus, increasing the weight % of PMMA decreases the healing rate in GE samples. As the healing process depends on the diffusion of Li^+ and PMMA chains, the viscosity of GE and hence the weight % of PMMA (or PC) becomes a critical parameter. On increasing the PMMA weight %, the amount of PC in GE decreases, and its viscosity increases. At higher viscosity, the diffusion of ions and chains becomes difficult and consequently, the healing rate of GE reduces at higher weight % of PMMA. Another factor that may affect the diffusion and may contribute

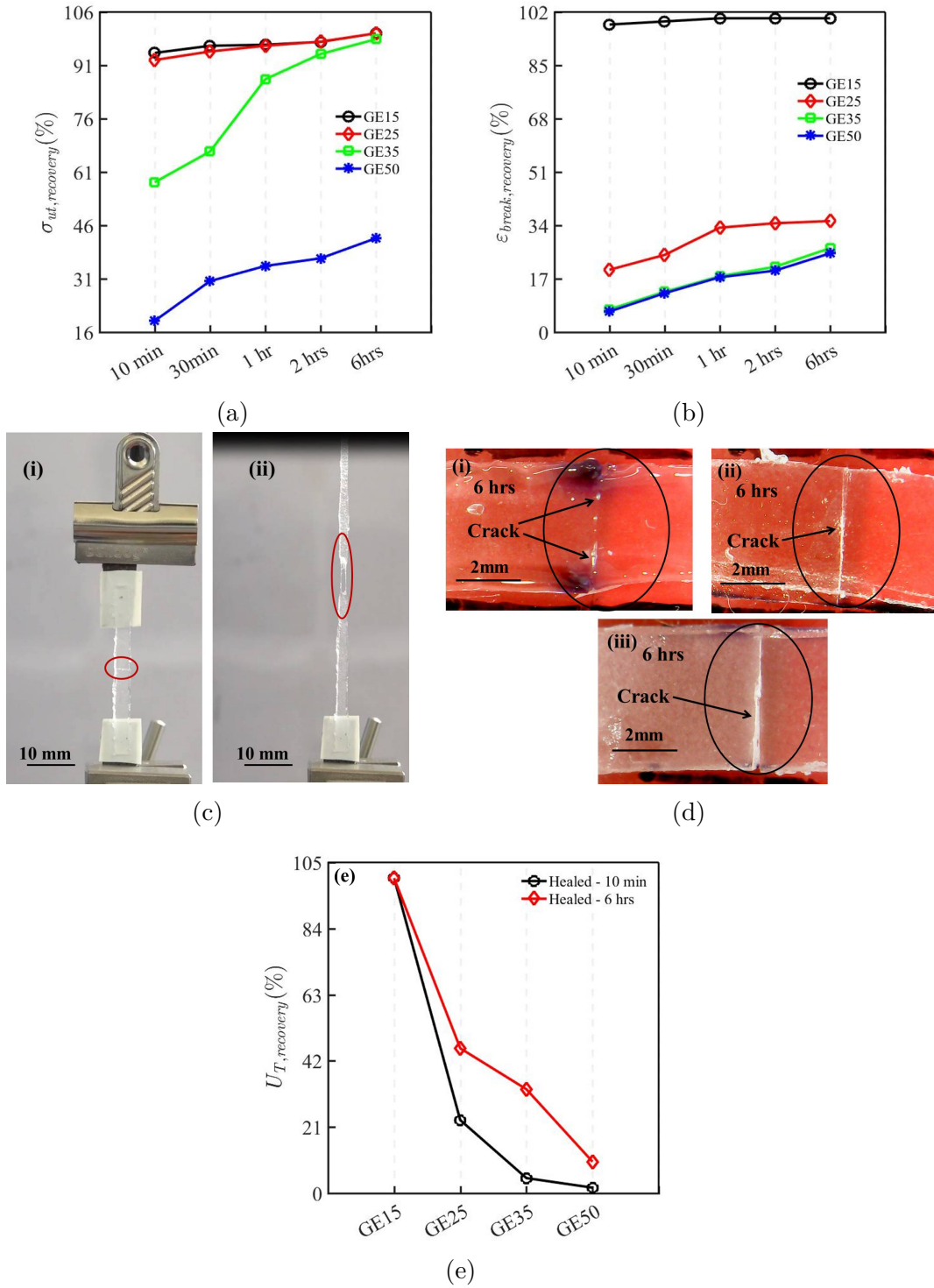


Figure 3.7: Recovery of (a) tensile strength, (b) elongation at break and (e) toughness modulus of GE15, GE25, GE35 and GE50 as a function of healing time. (c) GE25 during the tensile test marked the healed point (i) before stretching and (ii) after failure. (d) Optical images of (i) GE25, (ii) GE35 and (iii) GE50 after 6 hours of healing time.

toward the healing rate is the difference between healing temperature and T_g (ΔT) [151]. ΔT is highest for GE15 (85.5°C) and lowest for GE50 (28°C). Therefore GE15

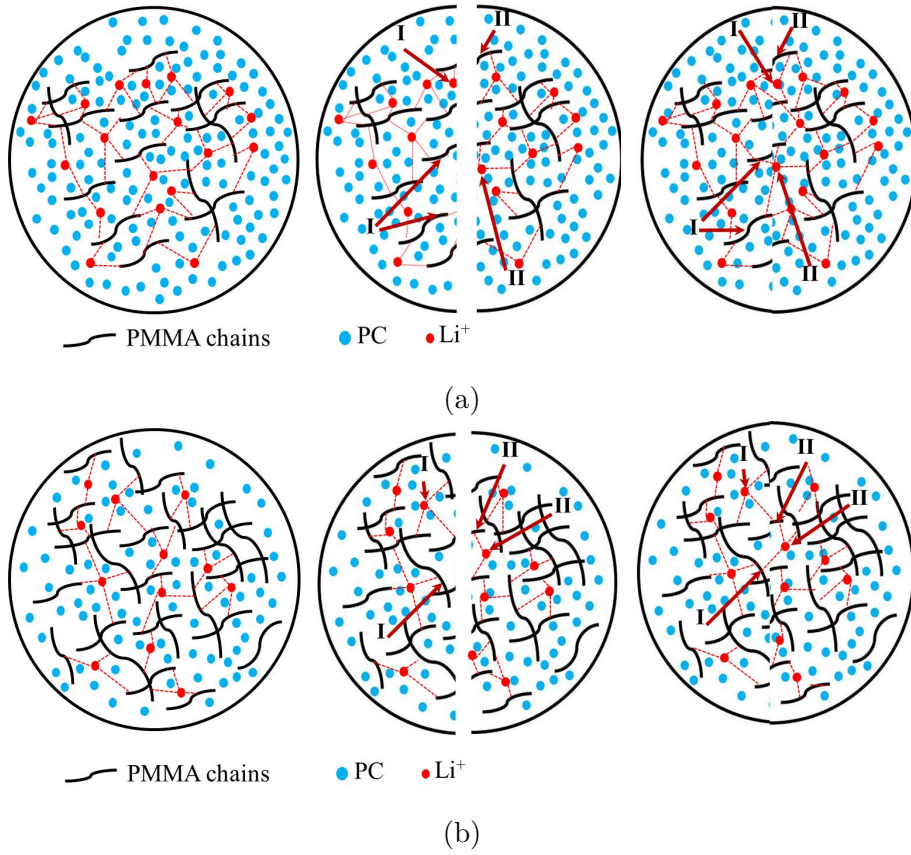


Figure 3.8: Schematic of (a) GE15 and (b) GE25 (original, after break, healed) network showing the re-crosslinking of Li^+ —PMMA at the interface of two parts (I and II).

shows the maximum healing rate while GE50 has the slowest healing rate among all the samples. A similar observation of higher recovery with increasing time has been reported in the literature [152, 150].

The recovery rate of elongation at break ε_{max} is slower than the tensile strength except for GE15 in Figure 3.7b. GE15 recovers 98% after 10 min and shows complete recovery after 6 hrs of healing time. However, ε_{max} reduces significantly for other GE samples prepared with higher PMMA concentration. While GE25 shows maximum recovery of 34%, GE35 and GE50 recover around 20% elongation after 6 hrs. The recovery rate of GE15 samples is found to be similar to that of existing self-healable gel electrolytes [100, 107]. Table 3.1 compares the time-dependent recovery in mechanical properties of GE15 samples with other gel-based ionic systems reported in the literature [100, 107, 106, 153, 99]. The recovery of ε_{max} in healed samples depends on the uncoiling and mobility of Li^+ —PMMA cross-links. Li^+ —PMMA crosslinks contribute more towards elongation in GE15 as there are fewer chains due to a lower concentration of PMMA (see Figure 3.8a). On increasing the PMMA weight%, the relative contribution of PMMA—PMMA interaction towards strain recovery increases. Moreover, the higher viscosity of GE and the presence

Table 3.1: Comparison of current work with the reported gel electrolytes.

S No.	Materials	Healing time	$\sigma_{ut,recovery}$ (%)	$\varepsilon_{break,recovery}$ (%)	$U_{T,recovery}$ (%)	Ref.
1	GE15	10 min 2 hrs 6 hrs	94.5 96.8 100	98 100 100	91.2 - 100	This work
2	SIPE-5	24 hrs	82	99	Not reported	[106]
3	AAHA-IL	1 min	93.1	96.6	90.3	[153]
4	P(GMA2-AAm8)-borate	1 min	Not reported	97	92	[99]
5	P(AA-VIm-VSN)	20 min	90.5	Not reported	Not reported	[100]
6	DSP	2 hrs	Not reported	Not reported	Not reported	[107]

of more PMMA chains decrease the movement of Li^+ (see Figure 3.8b) at the healed interface. Consequently, the GE samples show slower recovery of ε_{max} with increasing weight% of PMMA in GE samples. Moreover, it is observed in Figure 3.7c that the healed samples predominantly fail at the joined interface under tensile testing. Due to inefficient healing, the presence of cracks and voids are also observed in 6 hrs healed GE25, GE35, and GE50 samples in Figure 3.7d(i, ii and iii). These cracks may also contribute towards a reduction in tensile strength and ε_{max} in healed samples.

The variation in toughness U_T of healed samples compared in Figure 3.7e follows a similar trend as observed in Figures 3.7a and 3.7b. It shows that the recovery of U_T decreases with increasing PMMA concentration for a given healing time. Moreover, at a constant PMMA concentration, U_T improves for longer healing times. While the reduced recovery at higher PMMA concentration is due to the increase in viscosity, the better recovery for longer healing times may be attributed to the enhanced Li^+ - -PMMA and PMMA- -PMMA interactions at the interface. Moreover, healing is essentially crack closure due to the re-building of interaction between cracked surfaces. To calculate the energy required for the growth of the crack, a tensile test is performed on the notched specimen of GE50 (Figure 3.9a). Area under $F - \delta$ curve provides the energy required for the crack to grow. It is found to be $\sim 2\text{mJ/mm}^2$ (Figure 3.9b) which is close to the reported value for pure PMMA [154]. The electrostatic interaction between Li^+ and carbonyl group at the crack interface is an exothermic process,

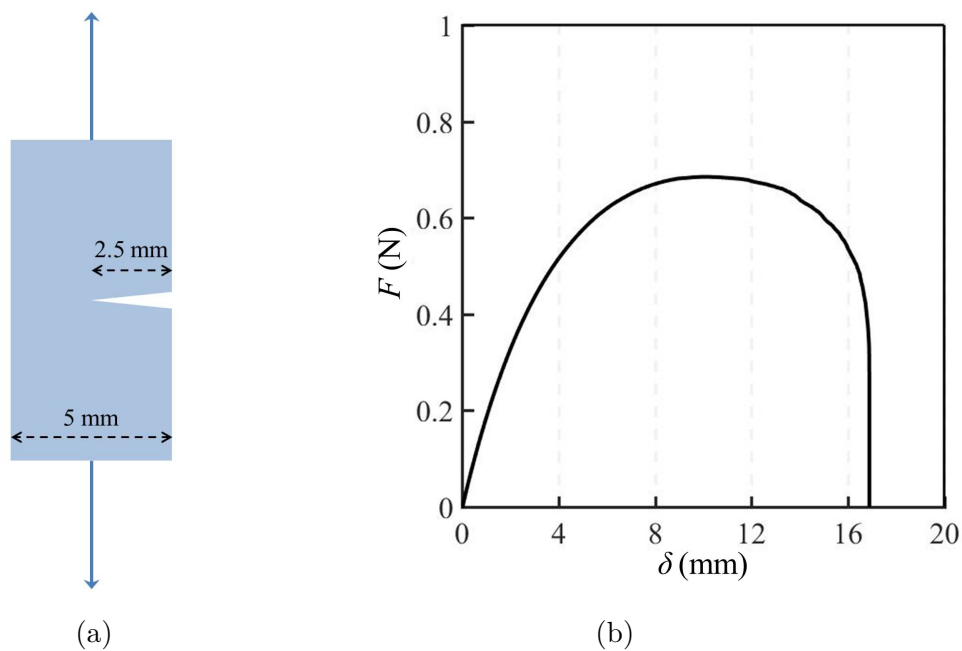
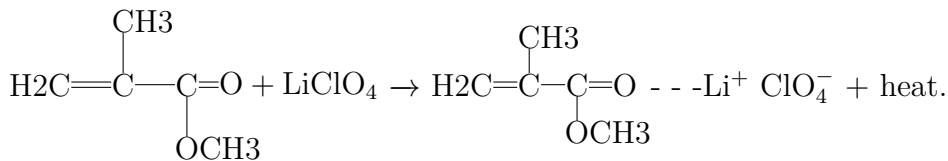


Figure 3.9: (a) Schematic of notched specimen and (b) corresponding $F - \delta$ curve of GE50 sample.



Approximately, 0.4 - 1.1 kJ/mm² energy [155] is released during the interaction among Li⁺ and C=O group. Thus, sufficient energy is available for crack closure during the healing process. The longer healing time promotes more interactions and hence higher recovery in strength, elongation at break, and toughness of healed samples.

Based on the tensile testing of healed samples, GE15 seems to be a better choice as it recovers faster and shows complete recovery after around 2 hours of healing time. However, the mechanical healing of GE is not the only parameter, and ionic conductivity of GE plays an equally important role in the performance evaluation of ECD. Therefore, the effect of PMMA concentration on the ionic conductivity of original and healed GE samples is compared next.

3.3.4 Effect of PMMA concentration on the ionic conductivity of GE

Ionic conductivity (λ_{ionic}) is a key property that determines the choice of GE in an ECD. It should be in the range of 10⁻⁴ - 10⁻³ mS/cm for practical applications [156, 79]. Figure 3.10 shows the variation in ionic conductivity as a function of PMMA concentration in GE. Ionic conductivity decreases at higher weight% of

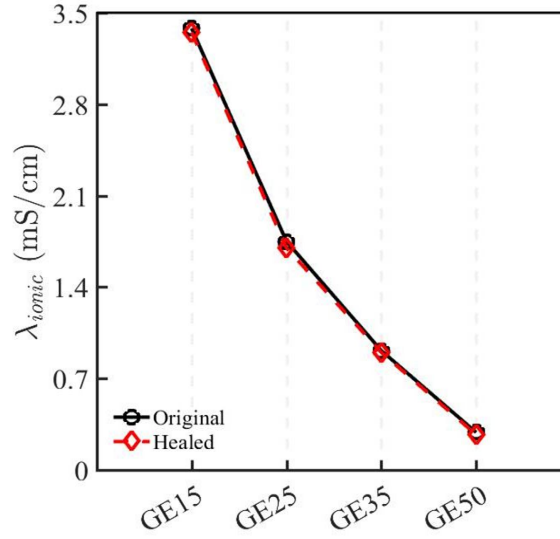


Figure 3.10: Ionic conductivity of original and healed GE specimens.

PMMA and is found to be 3.38 mS/cm, 1.75 mS/cm, 0.91 mS/cm, and 0.29 mS/cm for GE15, GE25, GE35, and GE50 respectively. In gel electrolytes, PMMA forms the matrix and encages the liquid electrolyte (LiClO₄ + Propylene carbonate (PC)). Lithium and perchlorate ions migrate through the solvent (propylene carbonate) domain surrounded by the PMMA matrix. On increasing the PMMA, polymer chains hinder the movement of ions (charge carriers) which reduces the ionic conductivity. As also observed in tensile testing the viscosity of GE increases at higher PMMA concentration. Higher viscosity causes the interruption in the mobility of ions which may reduce λ_{ionic} of GE as recorded in Figure 3.10. Moreover, the ionic conductivity measurements of healed samples suggest that GE is able to regain its original λ_{ionic} after 10 mins of healing time. Thus, the mobility of Li⁺ ions is comparable in original and healed samples. This implies that the healing process is quite efficient with respect to the ionic conductivity in comparison to the mechanical healing recorded in the previous section. Since GE15 has higher λ_{ionic} and it shows a better and faster recovery of tensile strength and elongation at break in a healed sample, a comparative analysis of ECD fabricated using original and healed GE15 sample is performed next as a proof-of-concept.

3.3.5 Comparative analysis of electrochromic device (ECD)

Even though the previous analysis suggests that the addition of PMMA provides self-healing characteristics to GE, the performance of ECD fabricated with original and self-healed GE needs to be compared to show the efficacy of the present approach in practical applications. To this end, ECDs are fabricated with original, 10 mins

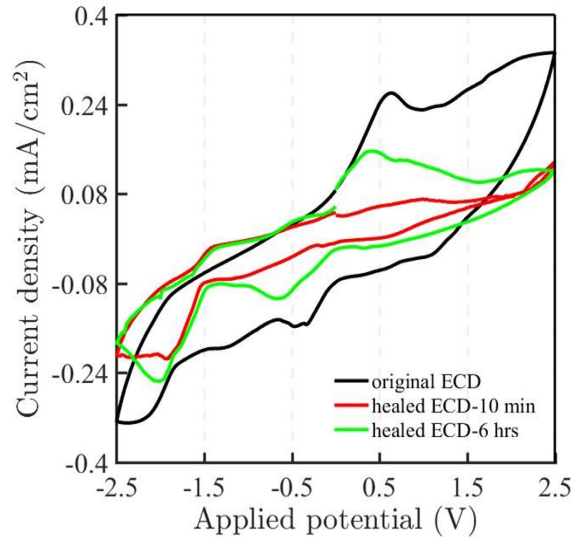


Figure 3.11: Cyclic voltammetry curve of original and healed ECDs.

Table 3.2: Mean square error (MSE) of digital images of GE15, GE25 and GE35 based ECD between neutral and excited states.

ECD	GE15	GE25	GE35
Original _(reduced)	670	373	164
Original _(oxidized)	742	440	279
Healed-6hrs _(reduced)	408	128	52
Healed-6hrs _(oxidized)	592	158	70

and 6 hrs healed GE15 layer. Polyaniline (PANI) is used as an electrochromic layer in all the ECDs manufactured following the procedure described elsewhere [145]. Figure 3.11 compares the cyclic voltammetry response of ECDs. The peak current is lower for healed ECDs than the original ECD. Moreover, the relative decrease is smaller for ECDs that are allowed to heal for 6 hrs in comparison to 10 min healed ECDs. A better-healed interface poses a lower hindrance to the ion movement and thus 6 hrs healed ECD shows higher peak current as compared to 10 min healed ECD. The ionic conductivity of original and healed ECDs follows similar variations. It is $60 \mu\text{S}/\text{cm}$ for the original and decreases to $21 \mu\text{S}/\text{cm}$ and $52 \mu\text{S}/\text{cm}$ for 10 min and 6 hours healed ECD respectively. It again supports the idea of better healing of ECD (or GE) at larger healing times.

To get further insights, the digital images and color contrast analysis of original and healed ECDs are carried out next. Figure 3.12 compares the images of original, 10 min and 6 hrs healed ECDs at their respective reduction, neutral, and oxidation potentials. The original ECD in Figure 3.12a changes color from greenish to yellow at reduced and greenish to blue at oxidized state. The 10 min and 6 hrs healed ECDs (Figure 3.12b and 3.12c) show similar color change albeit of a different shade.

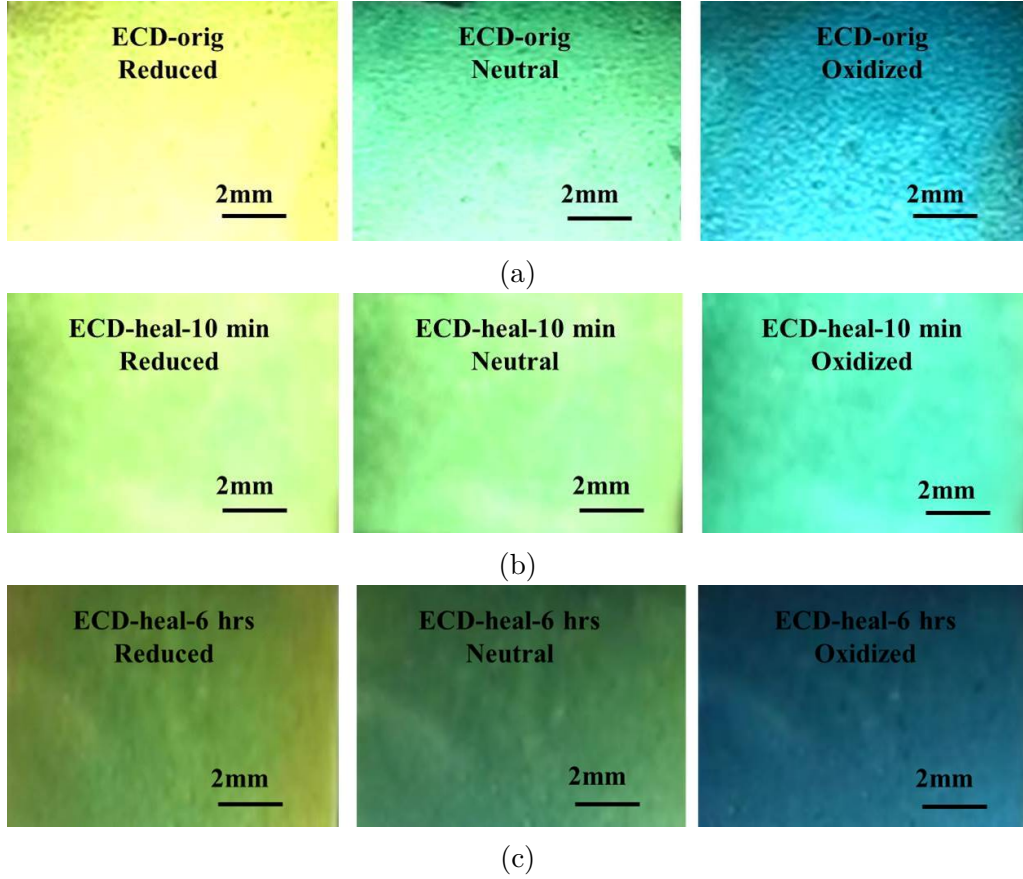


Figure 3.12: Digital images of (a) original ECD and (b) 10 min and (c) 6 hours healed ECDs at different excited states.

Therefore, the color contrast analysis of these ECDs is presented in Figure S3 to have a quantitative comparison. To calculate the color contrast, $L^*a^*b^*$ (L^* : lightness, a^* : green-red axis, b^* : blue-yellow axis) color coordinates of digital images are taken into consideration. Mean square error (MSE) is calculated between neutral and excited states using the following relation.

$$MSE = \frac{1}{L \times a \times b} \sum_{n=1}^{L \times a \times b} (p_{neutral} - p_{excited})^2 \quad (3.4)$$

where p is the pixel intensity of digital images. For the original ECD, MSE is 670 and 742 at reduced and oxidized state respectively (Figure S3a). The MSE decreases to 51 and 264 at reduced and excited states for 10 min healed ECD (Figure S3b). After 6 hrs of healing time, the MSE of healed ECD increases to 408 and 592 at reduced and oxidized states (Figure S3c). The lower MSE indicates that it will be relatively difficult to notice the color difference in 10 min healed ECD in comparison to the original and 6 hrs healed ECD. Thus, increasing healing time not only improves the recovery of GE, it also enhances the color performance of healed ECD with respect to the original ECD. Further, GE25 and GE35 are also used in ECD to

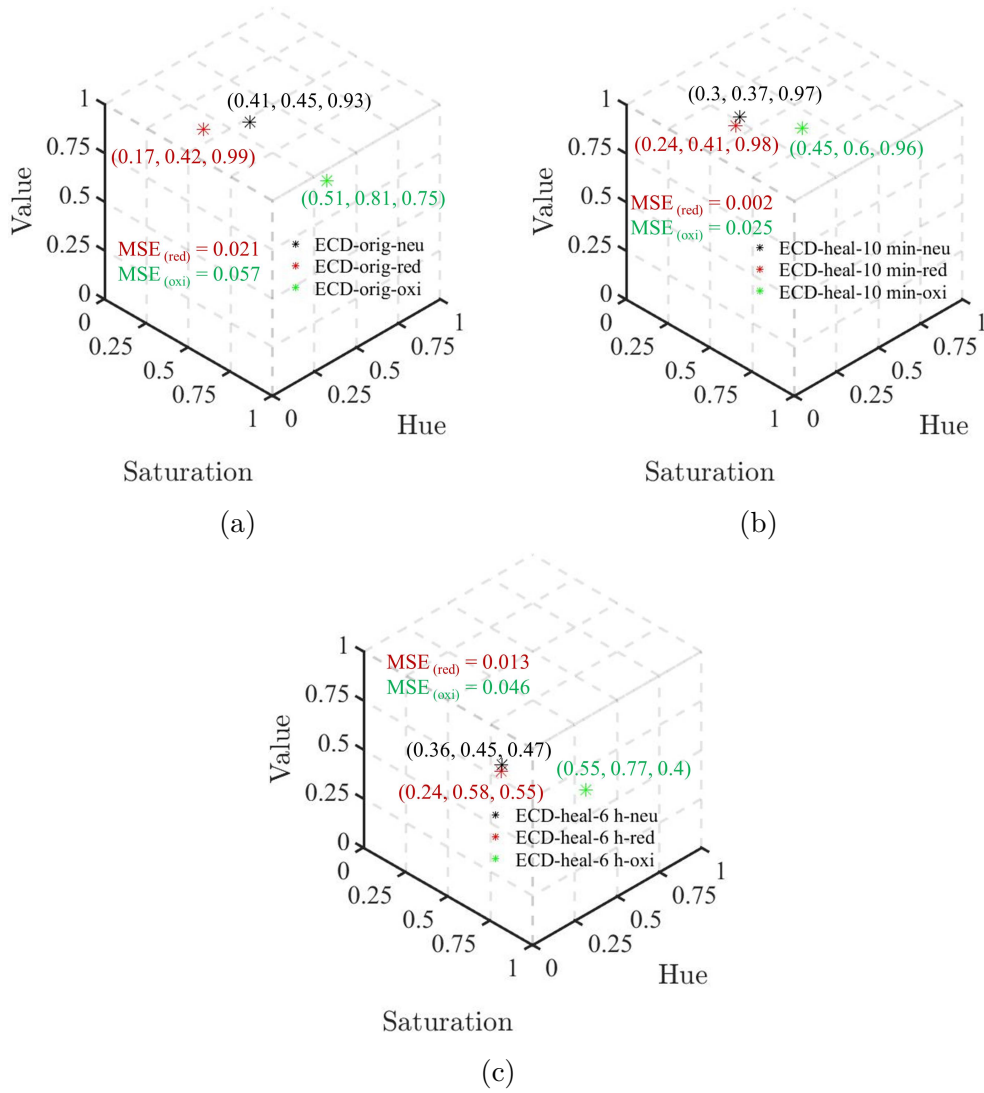


Figure 3.13: Mean of the color coordinates of digital images of (a) original ECD, healed ECDs after (b) 10 min and (c) 6 hours of healing at different excited states in HSV color space.

understand the effect of PMMA concentration on color contrast recovery. MSE of ECD is calculated after 6 hours of healing and compared with the original one (see Table 3.2). It is interesting to note that on increasing the PMMA in GE, a color difference (MSE) of ECD reduces at excited states. This may be due to the decrease in ionic conductivity of GE with increasing PMMA (Figure 3.10). Like GE15, the color contrast of GE25 and GE35 increases at a larger healing time.

3.4 Conclusion

During the handling and operational life of ECDs, minor cracks, cuts, and mechanical damage may appear in GE. In such situations, ECDs need to be replaced due to the lack of suitable repair protocols. Self-healable GE is one of

the possible strategies to improve the service life of ECDs. The fabrication of GE with self-healing capabilities is demonstrated in this study. An optimum loading of PMMA allows GE to heal itself when subjected to cuts and fractures. Moreover, it is observed that the healing mechanisms are different with respect to the recovery of mechanical properties and ionic conductivity. While GE shows faster recovery in ionic conductivity, the regain in mechanical properties is relatively slower. Finally, it is shown that the color contrast of ECD prepared with healed GE approaches to that of original ECD with increasing healing time. The findings of the present study will be useful in increasing the service life of ECDs used in flexible displays, smart textiles, etc. Even though self-healable GEs are characterized for ECD application, they may also be explored for energy storage and energy conversion devices.

Chapter 4

Modulation of optical properties of electrochromic device

The focus of this chapter is to develop the technique for acquiring green shades in the required camouflaging devices, which is one of the major requirements of this thesis. An experimental investigation is carried out to modulate the optical properties of electrochromic devices (ECD) by varying the thickness of electrochromic polymer (ECP) layer using composition of self-healable GE optimized in the previous chapter. Polyaniline (PANI) is preferred as ECP due to its ability to change colors from light green to green to blue at different voltages. ECDs are fabricated having varying thickness (250–650 nm) of the PANI layer. Topography, morphology, and optical measurements show that the roughness, porosity, and shade of green color depend on the thickness of PANI layer. The effect of ECP layer thickness on the optical performance of ECDs is evaluated through detailed electrochemical, optical, spectroelectrochemical measurements, and spectral colorimetry. ECD shows different shades of green and blue color with higher color contrast for the thicker PANI layer. The reflectance spectra are later used to define the color space for all the ECDs. While the color difference of the ECD fabricated with 250-nm-thick ECP is small, the ECDs prepared using thicker ECP layers show noticeable color difference of greater than 2.

4.1 Introduction: Electrochromic devices

Electrochromic device (ECD) is a multilayered assembly that switches color on the application of voltage [24, 25, 26]. It finds applications in diverse engineering fields including energy storage, display, smart window, smart textiles, smart fabrics, etc., [27, 28, 29, 30, 31, 32]. An ECD typically consists of gel electrolyte and an electrochromic layer sandwiched between two electrodes. The change in color is induced by the variation in energy states of the electrochromic layer under applied voltage. The color and other performance parameters of the ECD depend on various factors like types of electrodes [33], microstructure [34], band-gap [35] etc. In addition, thickness and chemistry of the electrochromic layer also influence the

electrochromic performance of ECD [36]. Over inorganic materials, electrochromic polymers (ECP) are increasingly used in ECDs [42, 43, 44] as they show multitude of color variations with high color contrast and at low power consumption [45]. The choice of electrochromic material depends on the specific ECD application requirements. Thiophene and its derivatives are used to get red, blue, and brown colors at different excited states [47, 48, 49]. Polynorbornene shows light yellow, green, and blue colors [33]. Poly(3,4-ethylenedioxyphenylene) (PEDOS) converts from a blue color to a transparent state on oxidation [34]. Polyaniline (PANI) undergoes multi-coloration states from light green to green to blue if prepared in an acidic medium [52].

The aim of the present study is to develop ECD that can be integrated with the smart textiles used in greenish surroundings and therefore polyaniline (PANI) is chosen as the ECP layer. Moreover, PANI is preferred due to its facile synthesis, reversible redox chemistry, excellent environmental stability, low cost and high conductivity [68]. It has multiple excited states named as leucoemeraldine, emeraldine and pernigraniline and thus it provides different colors in ECD [67]. Different methods such as chemical oxidation, interfacial polymerization, microemulsion polymerization, and electrochemical polymerization are reported to polymerize PANI [69]. In the chemical method, an oxidizing agent is used to oxidize aniline monomer in an acidic medium which initiates the chain growth of polymer [70]. Drop coating [71], spin coating [72, 73], and dip coating [70] techniques are used to coat PANI on different substrates. Here, a thin layer of PANI is coated on the ITO side of the ITO/ PET sheet by electrochemical polymerization as there is no need for an oxidizing agent in this process. Moreover, it provides easy control over deposition parameters and hence on the thickness and morphology of the PANI layer. The optical behavior of ECD depends on the charge transport and migration of counter ions. Consequently, the optical behavior of ECDs is found to be a function of the morphology of the ECP layer [45]. Fabrication of porous and fibrous PANI films by electrochemical polymerization has provided further motivation to use this process in the present study [157].

Even though many studies have explored different types of materials as an electrochromic layer, the effect of the thickness of the ECP layer on its morphology and optical behavior of ECD is rather less explored. According to Lambert's law, the optical properties of materials depend on their thickness and therefore the thickness of the ECP layer provides a handle to modulate the color of ECD. Consequently, it is important to quantify the effect of the thickness of the ECP layer on the optical performance of ECD and this will be the primary objective of the present study. To this end, PANI-based ECP layers of different thicknesses are prepared by varying the number of deposition cycles in the electrochemical polymerization process. The

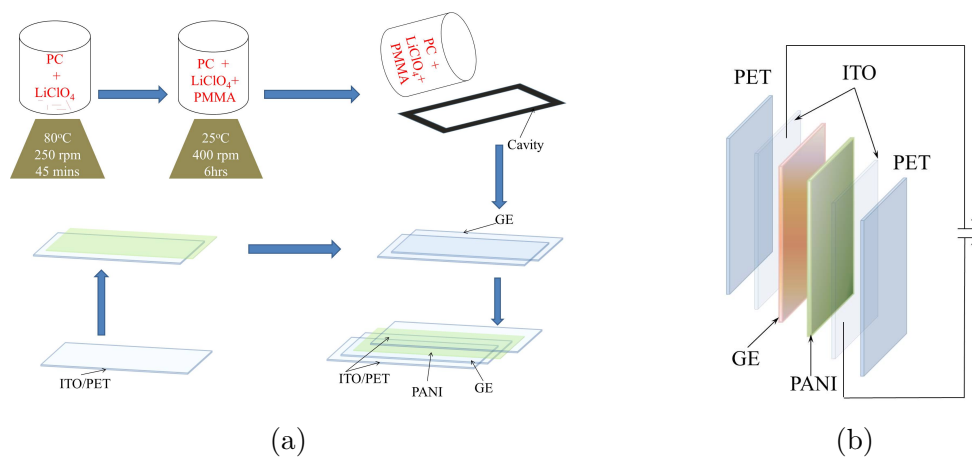


Figure 4.1: (a) Processing steps followed to fabricate ECD, and (b) Schematic of ECD showing all the layers and connections (PET/ITO/GE/PANI/ITO/PET)

morphology and optical characteristics of the ECP layer as a function of thickness are thoroughly investigated. Moreover, the effect of ECP layer thickness on the optical behavior of ECDs is compared with spectroelectrochemical measurements. Later on, spectral colorimetry is performed to quantify the color of ECDs in the visible range (380 nm -780 nm) for varying ECP layer thickness [158, 159]. It is shown that the color contrast and the shade of green color can be suitably modulated by changing the thickness of the ECP layer. The findings of the present study will be useful in developing smart textiles, e-textiles and skin/cover for surveillance robots and equipment employed in forest/green vegetation.

4.2 Experimental details

4.2.1 Materials and preparation

Figure 4.1a - 4.1b shows the processing steps and schematic of the fabricated ECD respectively. The ECD fabrication includes the preparation of PANI film and gel electrolyte (GE) followed by their assembly (Figure 4.1a). Sulphuric acid (H_2SO_4), lithium perchlorate (LiClO_4), poly methyl methacrylate (PMMA), and propylene carbonate (PC) are used as received. Aniline is de-oxidized at 150°C and 10^{-2} bar for 2.5 hours before using it for ECD fabrication. 0.2 M of distilled aniline is added to 0.2 M of H_2SO_4 and the mixture is sonicated for 45 minutes before using it for electro polymerization. ITO-coated flexible PET sheet of specific resistivity $15\Omega/\text{sq}$ and transmittance $> 75\%$ is purchased from Techinstro Ltd. It is cleaned by rinsing in a 1:1 mixture of ethanol and acetone followed by DI water [132]. Electropolymerization is performed in a three-electrode electrochemical cell with ITO as the working electrode, platinum wire as the counter electrode, and Ag/AgCl

as the reference electrode (Figure 2.2a). ITO/PET sheet is dipped in the monomer solution and potential is applied for 5, 10, 15, and 20 cycles. In each cycle, potential sweeps from -0.2 V to 1.0 V to -0.2 V at a scan rate of 50 mV/s. After the deposition, PANI film is rinsed with DI water to remove the unreacted monomer and oligomer followed by drying in open air [133]. The green color on the ITO substrate after electro polymerization process confirms the presence of an emeraldine form of PANI as shown in Figure 2.2b. A 450-micron-deep cavity is created on the PANI-coated ITO/PET sheet using acrylic double-sided tape.

Gel electrolyte (GE) is prepared by first mixing 1.5 M LiClO₄ in PC at C 80 and stirring the solution at 250 rpm for 45 minutes. Later, 15 wt % PMMA is added and the solution is stirred for 6 hours at 400 rpm for uniform mixing. After stirring, the solution is degassed in a vacuum for 1 hour to remove any trapped air and poured in the cavity created on PANI PANI-coated ITO/PET sheet. It is sandwiched by another ITO/PET sheet and allowed to cure for 1 week at atmospheric conditions. The architecture of PET/ITO/GE/PANI/ITO/PET assembly is shown in Figure 4.1b. After curing, the samples are characterized to understand the effect of a number of CV cycles on the ECP thickness, microstructure, and optical properties of ECD.

4.2.2 Characterizations

Cyclic Voltammetry (CV) and Electrochemical Impedance Spectroscopy (EIS) are performed on an electrochemical workstation (Metrohm Multi autolab M204, Netherlands). CV is used to evaluate the redox behavior of ECD in the potential range of -2.5 V to 2.5 V at the scanning rate of 20 mV/s and step potential of 2.44 mV. EIS is an electrochemical technique used to study the ion conduction mechanism in ECD. Data is recorded in the form of real and complex impedance for the applied frequency range of 0.1 - 10⁵ Hz. AC conductivity (λ_{ac}) is measured using $\lambda_{ac} = l/(R \times A)$, where 'R' is the intercept of the curve on the x-axis (real impedance), 'l' is the distance between electrodes and 'A' is the cross-sectional area of the electrode. Measurements, post-analysis, and curve fittings are performed on the software NOVA 2.1. All the experiments are carried out in potentiostatic mode. Characterization of ECD is performed using a two-electrode configuration in which PANI/ITO is used as the working electrode and ITO on another side is used as a counter electrode.

Atomic force microscopy (AFM) (Bruker, USA) analysis is performed in tapping mode on a scan area of 5 μm x 5 μm to measure the thickness and surface roughness of PANI layers as a function of number of CV cycles. The effect of a number of CV cycles on the surface morphology of PANI is studied with a scanning

electron microscope (SEM) (Jeol 6610LV Japan). Absorbance, transmittance, and reflectance spectra of PANI are recorded (PerkinElmer LAMBDA 950 UV/Vis/NIR spectrophotometer, USA) in the range of 380 nm – 780 nm. Spectroelectrochemical measurements of ECDs are performed with an in-situ UV-Vis spectrophotometer (Cary 60 of Agilent) electrochemical workstation (Keithley 2450).

4.3 Results and discussion

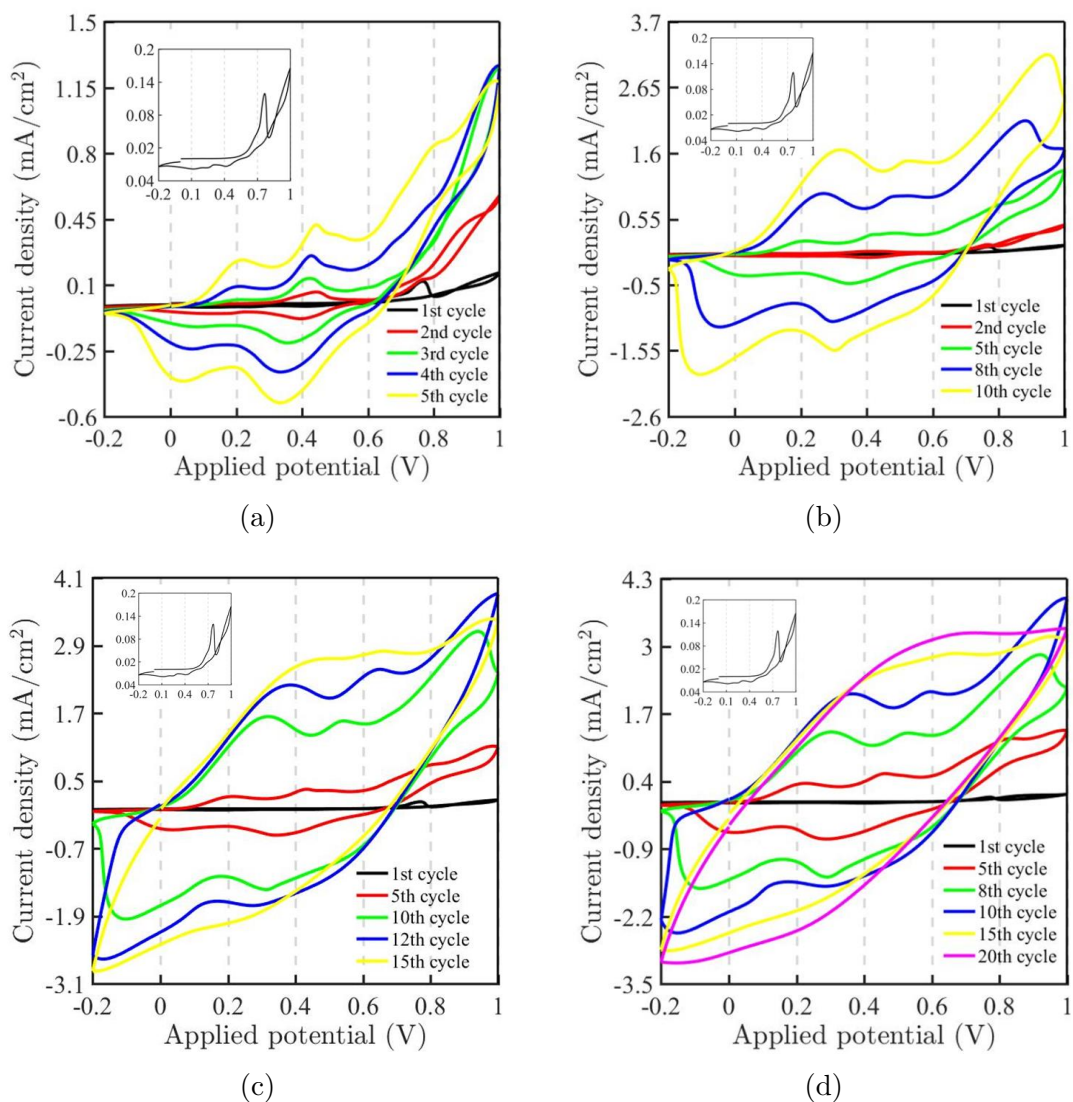


Figure 4.2: (a) Processing steps followed to fabricate ECD. (b) Schematic of ECD showing all the layers and connections (PET/ITO/GE/PANI/ITO/PET) (c) Photographic image of electrochemical set up used for electrochemical polymerization of polyaniline (PANI) and (d) green color polyaniline (PANI) film on ITO/PET sheet after electro polymerization process

4.3.1 Preparation of PANI layer

Deposition of PANI on ITO/PET sheet using electropolymerization is carried out for 5, 10, 15, and 20 CV cycles as shown in Figure 4.2, and the samples are named as PANI5, PANI10, PANI15 and PANI20 respectively. During the first cycle of electropolymerization (inset curve in Figure 4.2), Figure 4.2a shows the irreversible oxidation of aniline at 0.75 V as no reduction peak is recorded in CV plot of PANI5 [160]. In the second cycle, the first peak indicates the oxidation of the fully reduced form at 0.2 V and the second peak at 0.8 V shows the oxidation of the emeraldine form to pernigraniline form of PANI [161]. A peak at 0.45 V relates to the oxidation of intermediate products (p-benzoquinone) [162]. Electropolymerization of polyaniline is an autocatalytic process and the polymer formation on an already deposited layer is faster than on bare electrode [162]. The autocatalytic synthesis is confirmed by the increase in current density after the first cycle of electropolymerization. While the oxidation peaks shift towards the higher potential and reduction peaks shift towards the lower potential on increasing the number of CV cycles. It may be due to the increased iR losses [163]. A similar trend albeit with a different variation in current density with the applied voltage is recorded for PANI10 as shown in Figure 4.2b. Figure 4.2c - 4.2d reveals that the peak current decreases after 12 CV cycles in PANI15 and PANI20 samples. It indicates that the growth of PANI film is relatively slower from 12th cycle onwards as compared to the deposition that occurred during initial CV cycles. Moreover, an area under the CV curve increases with the increase in the number of CV cycles. It shows that the capacitance of the ECP layer increases with a higher number of deposition cycles.

4.3.2 Effect of CV cycles on the roughness and morphology of electrochromic PANI layer

The effect of CV cycles on the surface roughness of the PANI layer is studied using AFM analysis. Optical images with corresponding AFM micrographs and topographs are shown in Figure 4.3a - 4.3l. Film thickness and roughness are measured using these AFM micrographs and topographs respectively. At least 10 readings are taken to measure the average thickness and standard deviation of all the samples as shown in Figure 4.3m. The thickness of PANI film increases from 250 nm to ≈ 650 nm as the number of CV cycles increases from 5 to 20. Moreover, the ECP layer thickness varies non-linearly with the number of CV cycles as revealed by fitting the experimental data with a 2nd order polynomial having goodness of fit (r^2) ≈ 0.99 . Surface roughness (R_a) also increases with the increase in CV cycles

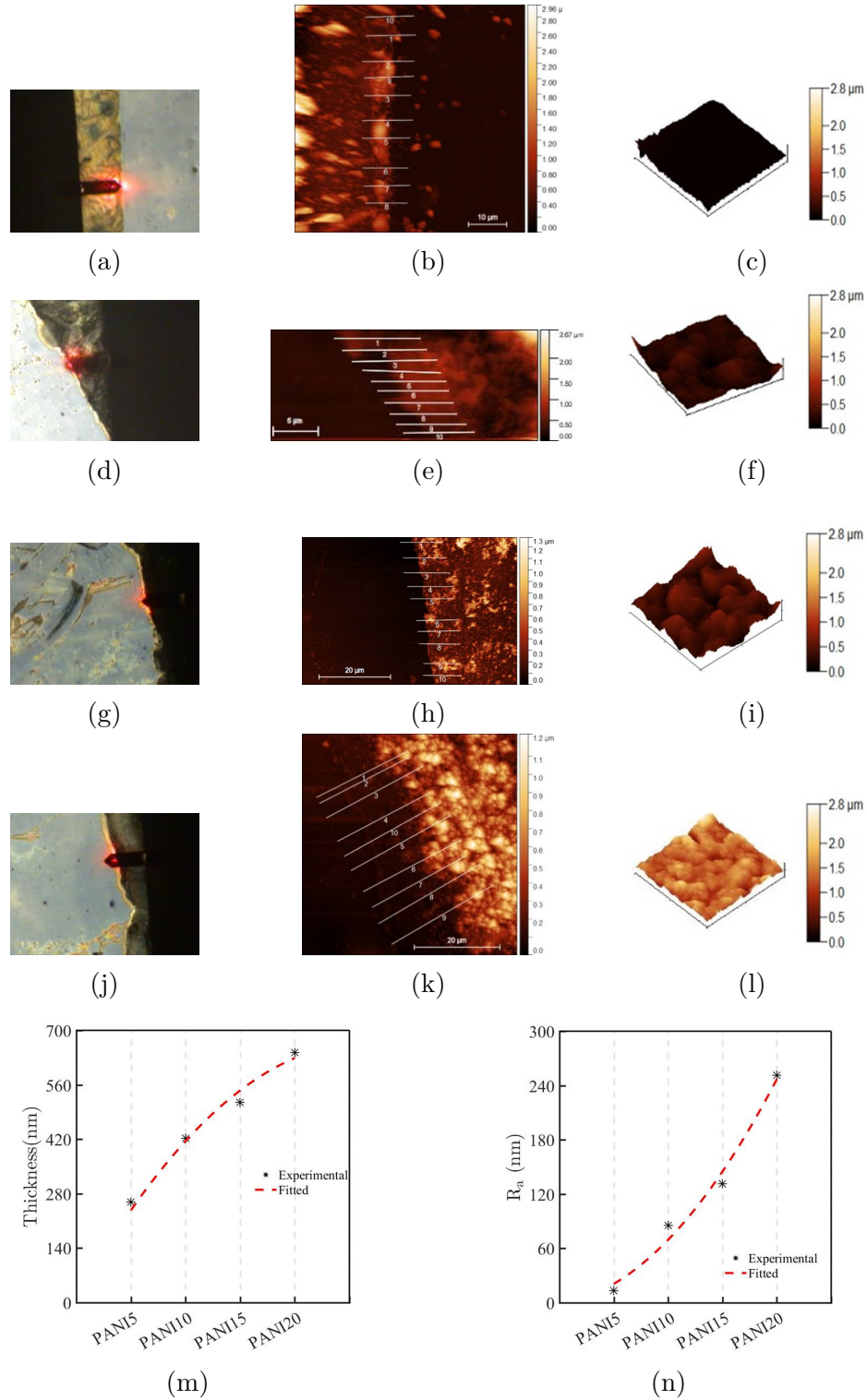


Figure 4.3: Optical images are showing the notch in (a) PANI5, (d) PANI10, (g) PANI15 and (j) PANI20 layer which is created to measure the thickness through AFM analysis. AFM micrographs of (b) PANI5, (e) PANI10, (h) PANI15 and (k) PANI20 layer showing all 10 readings in each film. AFM topographs of (c) PANI5, (f) PANI10, (i) PANI15 and (l) PANI20 films. Variation of (m) thickness and (n) surface roughness of PANI layers with increasing number of CV cycles. 2nd order polynomial used to fit the experimental data points is also included in (m) and (n).

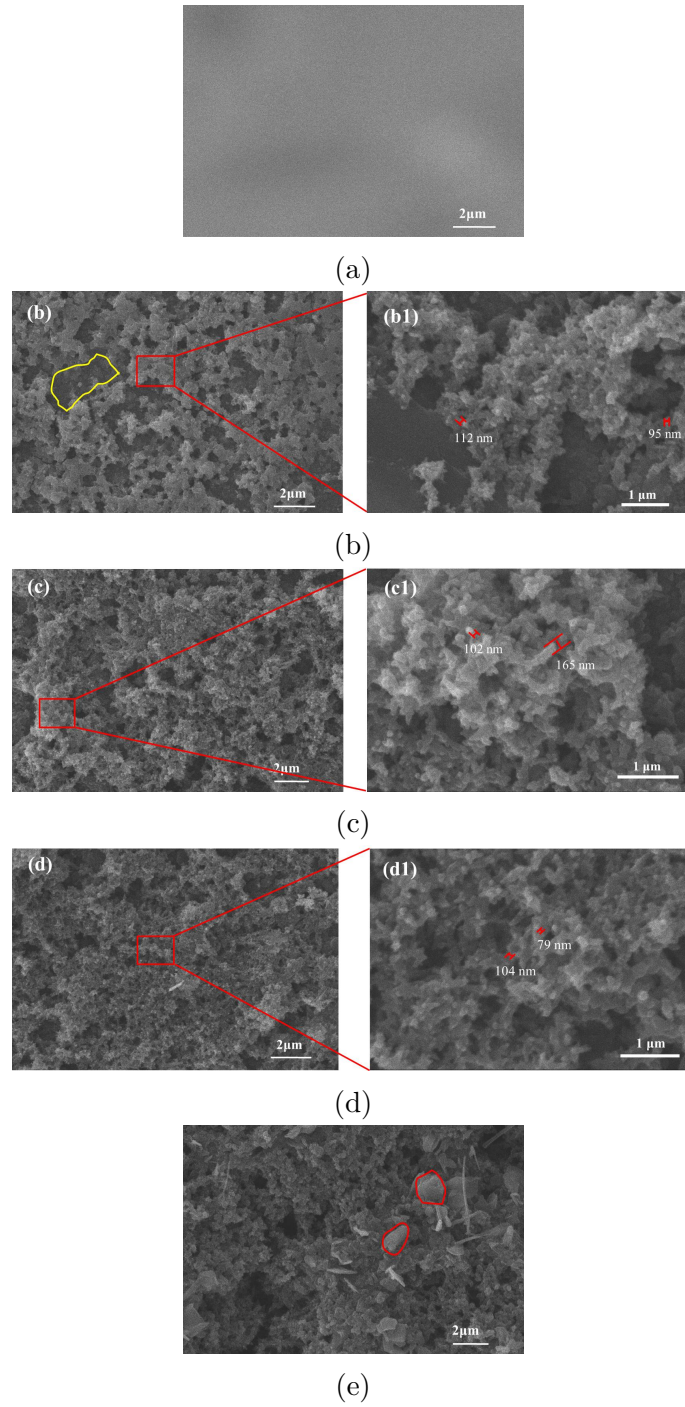


Figure 4.4: SEM micrographs of (a) bare ITO, (b) PANI5, (c) PANI10, (d) PANI15 and (e) PANI20 films. The zoomed micrographs of these samples are also included in (b1 – d1).

as shown in Figure 4.3n. It also shows a similar type of non-linear variation (2^{nd} order polynomial with goodness of fit (r^2) ≈ 0.98 .) with the number of CV cycles as recorded for thickness. The PANI film is deposited layer-wise. The underlying smooth surface of ITO ensures lower roughness for the first PANI layer. However, the roughness of the subsequently deposited layer increases due to the relatively

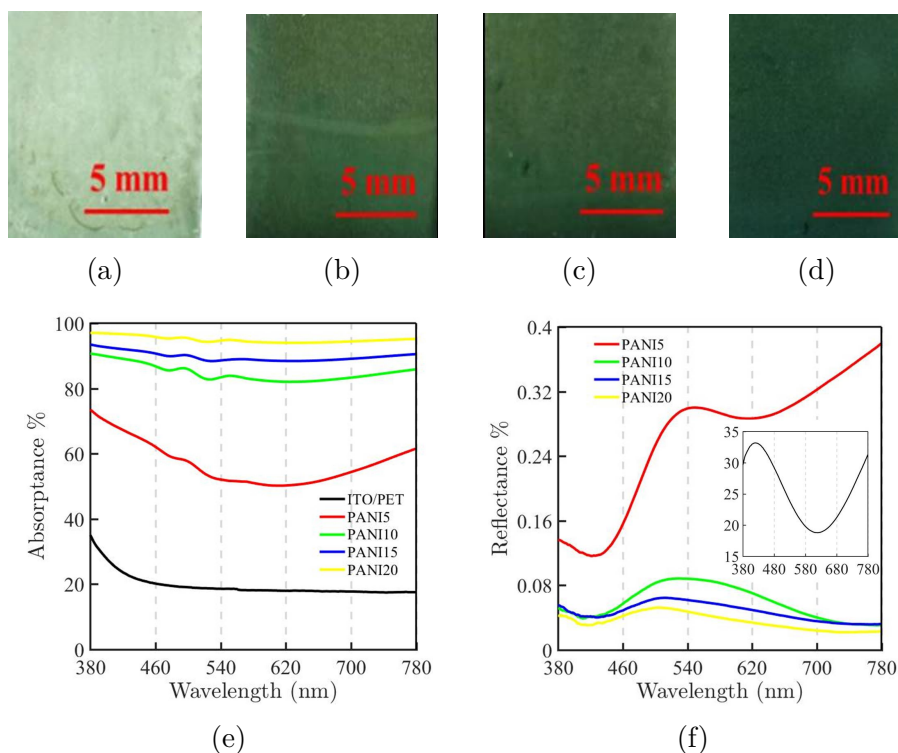


Figure 4.5: Photographic images of (a) PANI5, (b) PANI10, (c) PANI15 and (d) PANI20 films showing the shades of green color. Comparison of (e) Absorbance vs wavelength and (f) Reflectance vs wavelength (curve of ITO/PET is in inset) spectra of all the PANI films.

rougher surface of the pre-existing PANI layer.

The effect of a number of CV cycles on the morphology of PANI films is examined in SEM micrographs as shown in Figure 4.4. Figure 4.4a shows the relatively even surface of the ITO substrate used to deposit the PANI layer. The micrograph of PANI5 film deposited on ITO using 5 CV cycles is observed in Figure 4.4b (zoomed view in Figure 4.4b1). It reveals the porous and fibrous morphology of PANI5 film. The cavities are found between the branched fibrous networks which may be beneficial for the electrochromic applications. The diameter of nanofibers is in the range of 50-200 nm as shown in Figure 4.4b1, 4.4c1 and 4.4d1. On increasing the number of CV cycles, diameter of nanofiber remains in the similar range, the cavities between interconnected fibers are reduced due to the deposition of successive layers in PANI10 and PANI15 films as shown in Figure 4.4c - 4.4d (zoomed view in Figure 4.4c1 - 4.4d1). These observations suggest that the deposition of successive layers occurs due to the formation of a 3-D network by nanofibers with an increasing number of CV cycles. Further, an increase in CV cycles leads to the agglomeration of nanofibers in PANI20 film in Figure 4.4e. This may be the reason for the higher roughness of PANI film deposited with an increasing number of CV cycles recorded in AFM analysis (Figure 4.3).

4.3.3 Optical properties of electrochromic PANI layer

It is recorded in the previous section that the thickness and roughness of the PANI layer increase with the increase in a number of CV cycles. The effect of thickness and microstructure on the optical properties of the PANI layer is compared in Figure 4.5. Visual inspection of photographic images in Figure 4.5a suggests that the thickness does affect the shade of the green color of the PANI layer with a general observation of darker shade for thicker PANI film as shown in Figure 4.5a - 4.5d. To get a quantitative comparison, the absorptance and reflectance spectra of PANI film are compared in Figure 4.5e - 4.5f. In line with Beer-Lambert's law, Figure 4.5e shows that thicker PANI layer absorbs more light in the visible region. Multiple scattering and trapping of incident light in the rough and porous surface (Figure 4.3) is probably the reason behind this observation. Another contribution may come from the polaron and $\pi - \pi^*$ transitions that occur in the PANI layer [164]. For thicker PANI films, larger fraction of light participates in the polaron (higher wavelength) and $\pi - \pi^*$ (lower wavelength) transitions and thus increases the absorbance of irradiation. It is interesting to note that the absorptance of all the samples is relatively higher in the blue (380-490 nm) and red (625-780 nm) region in comparison to the green (490-625 nm) region.

The reflectance spectra in Figure 4.5f further reveal the optical properties of all the PANI films. The reflectance decreases for thicker samples in the entire visible range. Moreover, the reflectance of all the samples is higher in the green region than blue and red regions. However, the PANI5 film shows a strong peak in the red region. This may be due to the lower thickness of PANI5. The incident beam transmits through the layer and gets reflected from the underlying ITO substrate resulting in a peak in the red wavelength region for this sample. The reflectance spectrum of ITO/PET is included in the inset of Figure 4.5f.

4.3.4 AC conductivity of ECD

The preceding analysis shows that the shades of green color depend on the thickness and roughness of the PANI layer. It will be interesting to see how this dependence influences the optical properties of ECD fabricated using different PANI films. To this end, ECDs are fabricated by sandwiching the GE between ITO/PANI and ITO electrodes as shown in Figure 4.1b. Four ECDs, ECD-5, ECD-10, ECD-15 and ECD-20 are prepared by using PANI5, PANI10, PANI15 and PANI20 respectively as ECP layer. EIS is performed to understand the effect of PANI layer thickness on the ion conduction and AC conductivity (λ_{ac}) of ECDs. The ideal Nyquist plot with its equivalent circuit is shown in Figure 4.6a. The ideal curve consists of a

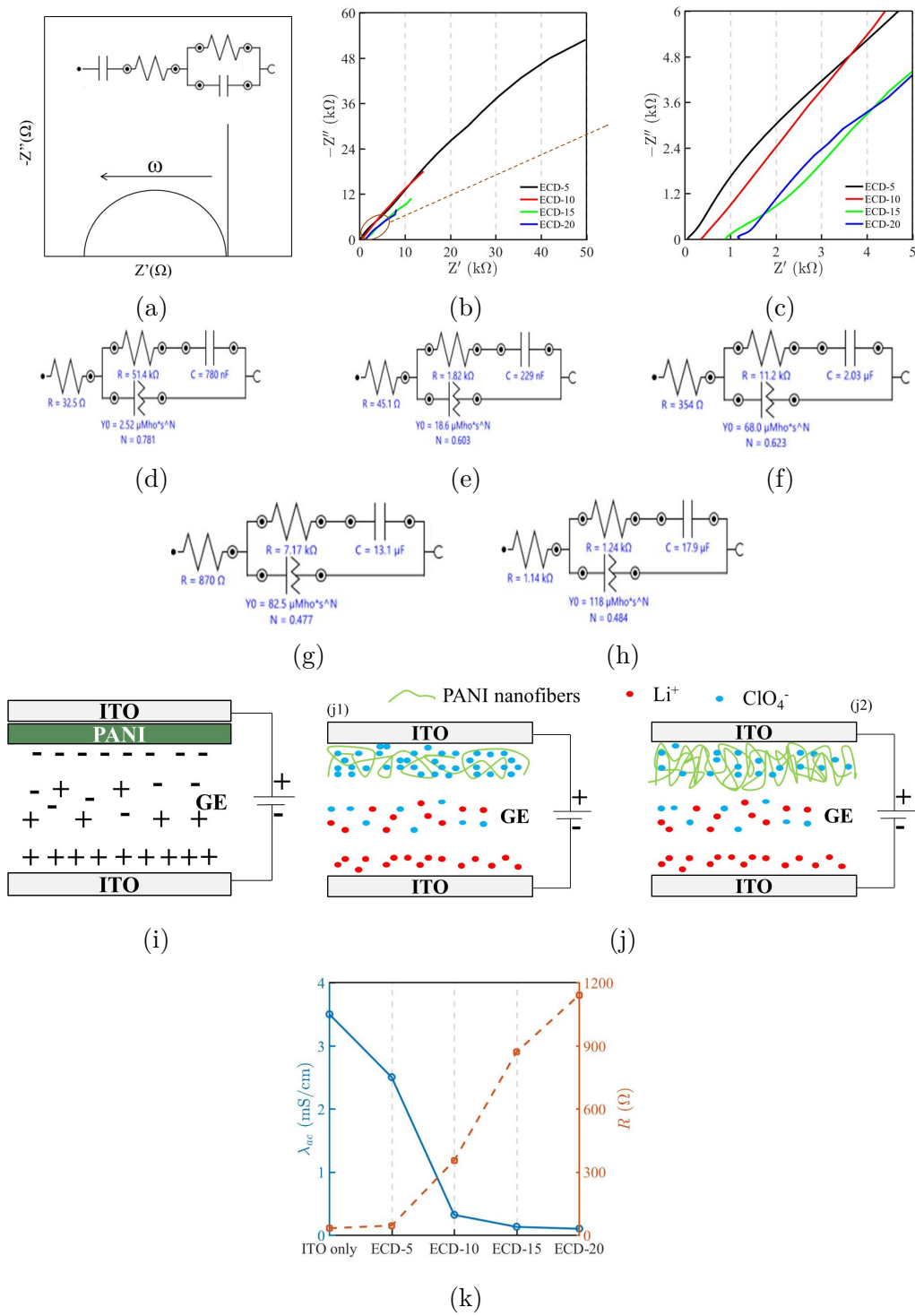


Figure 4.6: (a) Ideal Nyquist plot and its equivalent circuit. (b) Nyquist plot of all the ECDs and their (c) zoomed view. Equivalent circuit of (d) ITO only, (e) ECD-5, (f) ECD-10, (g) ECD-15 and (h) ECD-20. (i) Schematic of charge polarization at electrode/ electrolyte interface and (j) schematic representation of ion diffusion in (j1) ECD-5 and (j2) ECD-20. (k) AC conductivity and equivalent series resistance (R) of ITO and all the ECDs.

semi-circle at high frequency and a vertical spike at low frequency. Nyquist plots of

ECDs and their zoomed view are shown in Figure 4.6b - 4.6c and the corresponding equivalent circuits are given in Figure 4.6d - 4.6h. All the equivalent circuits are fitted using NOVA 2.1 software and they consist of resistor (R) ($Z = R$), capacitor (C) ($Z = 1/j\omega C$), and constant phase element (CPE) ($Z = 1/(Y_o(j\omega)^N)$). Here, Z is the impedance and ω is the frequency in 'Hz'. Y_o and N are constants representing the capacitance and slope, respectively.

The current-carrying ionic species in ECD are blocked at the electrode/electrolyte interface due to the interfacial resistance. The excess ionic charge on the interfacial side of an electrode is balanced by the excess electronic charge on the other side. There is a charge polarization at the interface of electrode/electrolyte which offers capacitance (Figure 4.6i). At low frequency, a spike in the impedance plot (vertical line in Figure 4.6a) is due to the interfacial capacitance [165]. The ideal spike occurs for the homogeneous double-layer capacitance and electrode surface. Due to the lack of homogeneity in the electrode surface, interfacial capacitance is replaced by constant phase element (CPE) [166]. The steepest curve is recorded for ECD-5 in Figure 4.6b and the slope of the curve decreases with the increasing thickness of the PANI layer. This may be attributed to the inhomogeneous electrode surface caused by the higher surface roughness of thicker PANI layers (Figure 4.3). Moreover, the steeper curve at lower frequency also suggests better ion transport and diffusion at electrode material [89]. According to SEM analysis in Figure 4.4, the cavity or free space available in the PANI layer decreases with increasing thickness of the PANI layer. The lower cavity size obstructs the diffusion of ions (schematic in Figure 4.6j) and thus decreases the slope for ECDs fabricated with thicker PANI layers as recorded in Figure 4.6b. The decreasing slope for ECDs having a thicker ECP layer may also be understood from the equivalent circuits in Figure 4.6d - 4.6h. It shows that N in CPE is highest for bare ITO and decreases with an increase in the PANI film thickness. Similarly, the increase in Y_o with the thickness of the PANI layer suggests that the capacitive behavior of ECDs increases with the thickness of the ECP layer.

In addition to the CPE, charge transfer resistance (R_{CT}) and geometrical capacitance (C_{geom}) elements are also present in parallel to CPE (Figure 4.6d - 4.6h). While R_{CT} appears due to the blocking of ions at the electrode/electrolyte interface, the geometrical capacitance (C_{geom}) arises from the multilayered structure of ECDs. The semi-circle at high frequency in Figure 4.6a indicates the bulk response of film and its absence in the impedance plots (Figure 4.6b - 4.6c) suggests that ionic conduction is the conductivity governing mechanism in all ECDs [167]. The intersection of the curve on the real axis at a higher frequency (100 kHz) gives the equivalent series resistance (R) which is the resistance offered by the electrolyte and electrode [89]. It is observed that R of ECDs increases with the increase in thickness

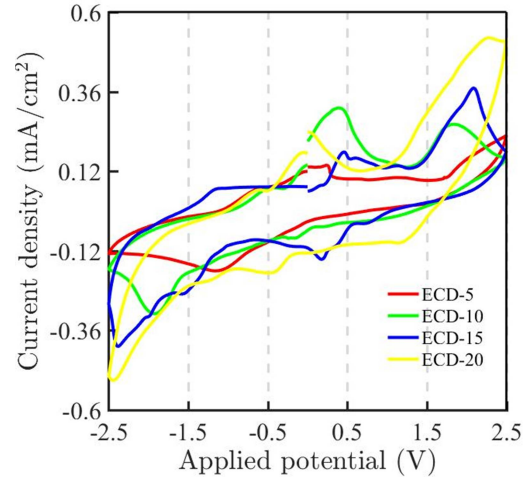


Figure 4.7: CV curves of all the ECDs

of the PANI layer. The AC conductivity of ECDs is related to the R according to Eq. (4.1),

$$\lambda_{ac} = l/(RA) \quad (4.1)$$

Here, $l = 450$ microns and $A = 0.5 \text{ cm}^2$ for all the samples. Figure 4.6k shows that the maximum conductivity is for bare ITO electrodes and decreases with the increasing thickness of the PANI layer. This decrease in AC conductivity may be attributed to the increase in R for ECDs prepared with thicker PANI layer as observed in equivalent circuits of ECDs in Figure 4.6d - 4.6h, 4.6k. It should be noted from Figure 4.6k that there is a sudden drop in λ_{ac} of ECD-10 in comparison to ECD-5. It may be connected to the larger size cavities present in PANI5 as compared to the relatively denser microstructure of the PANI10 layer in SEM micrographs as shown in Figure 4.4. It is easier for the ions (80 pm – 250 pm) to intercalate in PANI and interact with ITO for the thinner PANI5 layer. On the other hand, the interaction of electrolyte with ITO may be restricted due to the smaller size cavities present in the PANI10 layer causing an increase in R and a sudden drop in the ionic conductivity of ECD-10 with respect to ECD-5.

Table 4.1: Oxidation and reduction voltage of ECD-5, ECD-10, ECD-15 and ECD-20.

Samples	Reduction voltage	Oxidation voltage
ECD-5	-1.2	2.5
ECD-10	-2.0	1.9
ECD-15	-2.4	2.1
ECD-20	-2.5	2.3

4.3.5 Electrochemical properties of ECD

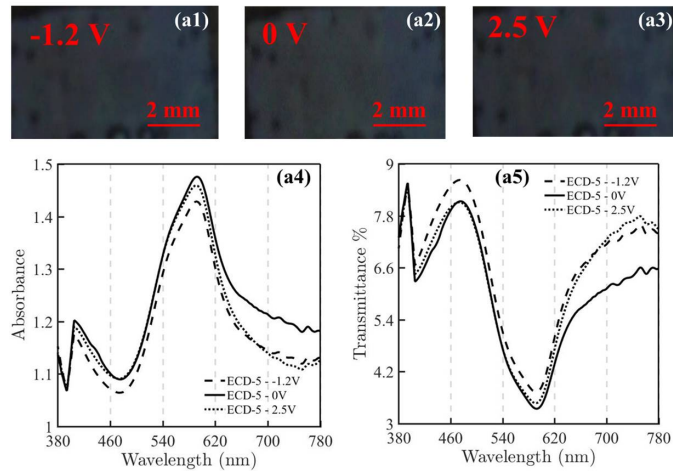
CV is performed in the range of -2.5 V to 2.5 V to find the redox potentials of ECD in Figure 4.7. Voltages corresponding to oxidation and reduction peaks of all the ECDs are given in Table 4.1. During oxidation, the emeraldine form of PANI is converted to pernigraniline form, and during reduction, it is converted to leucoemeraldine form [168]. Shifting of oxidation and reduction voltages towards higher potential is observed in CV curves. The ion diffusion becomes difficult in thicker PANI films and therefore, higher potential is needed for ion intercalation. This may lead to the shifting of the redox potentials. The higher iR loss in thicker PANI films may also contribute to the recorded variation in oxidation and reduction potential. More power is required to complete the ion diffusion process, as a result, peak current and redox potential increases. Moreover, the conjugated length of polymer increases with the increase in thickness of the film, and this may also be responsible for the shift in redox potentials [169].

Table 4.2: Color contrast and response time of all the ECDs at redox potentials.

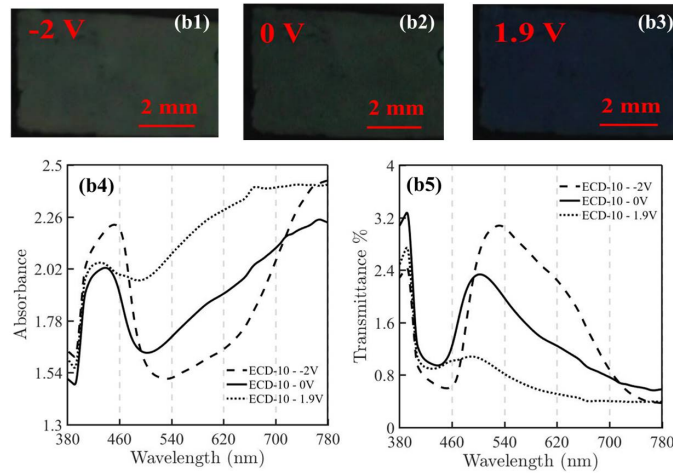
Samples	Applied voltage (V)	Color contrast %	Wavelength (λ_{max})(nm)	Response time (s)	Wavelength (nm)
ECD-5	-1.2	14.11	728	-	-
	2.5	16.80	734	-	-
ECD-10	-2.0	41.76	573	1.5	600
	1.9	56.04	510	16	600
ECD-15	-2.4	79.41	650	8	600
	2.1	69.21	510	14	600
ECD-20	-2.5	74.62	595	15	600
	2.3	79.31	516	19	600

4.3.6 Spectroelectrochemical properties of ECD

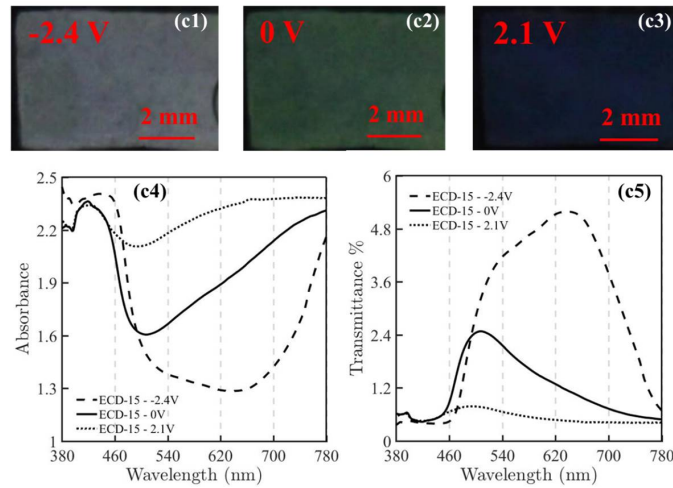
Spectroelectrochemical measurements are performed to evaluate the change in optical spectra of ECDs at different voltages. To this end, the variation in optical properties of ECDs is studied at their respective oxidation and reduction potentials given in Table 4.1. Photographic images, absorbance, and transmittance spectra of ECD-5, ECD-10, ECD-15, and ECD-20 at their corresponding redox potentials are compared in Figure 4.8. The photographic images of ECD-5 show no visually noticeable change at different voltages in Figure 4.8a1 - 4.8a3. The same has been recorded in the absorbance and transmittance spectra of ECD-5 in Figure 4.8a4 - 4.8a5. They are almost similar at all the states. On the other hand, the photographic images of ECD-10 show a shade of blue at an oxidation potential of 1.9 V and



(a)



(b)



(c)

different shades of green at neutral (0 V) and reduced (-2 V) state (Figure 4.8b1 - 4.8b3). The absorbance and transmittance spectra of ECD-10 in Figure 4.8b4 - 4.8b5 are qualitatively similar at 0 V and -2 V with different absorbance and transmittance values. It shows lower absorption and higher transmittance in mid-range wavelength

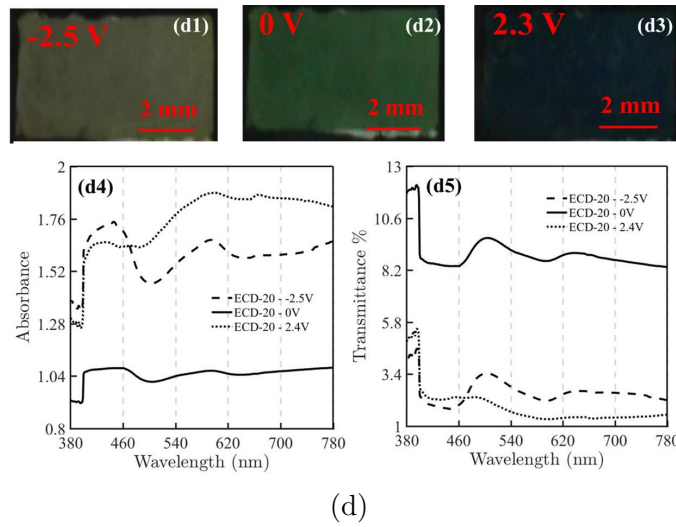


Figure 4.8: Photographic images at reduced, neutral and oxidized states (1-3), absorbance (4) and transmittance (5) spectra of (a) ECD-5, (b) ECD-10, (c) ECD-15 and (d) ECD-20 at their respective redox potentials.

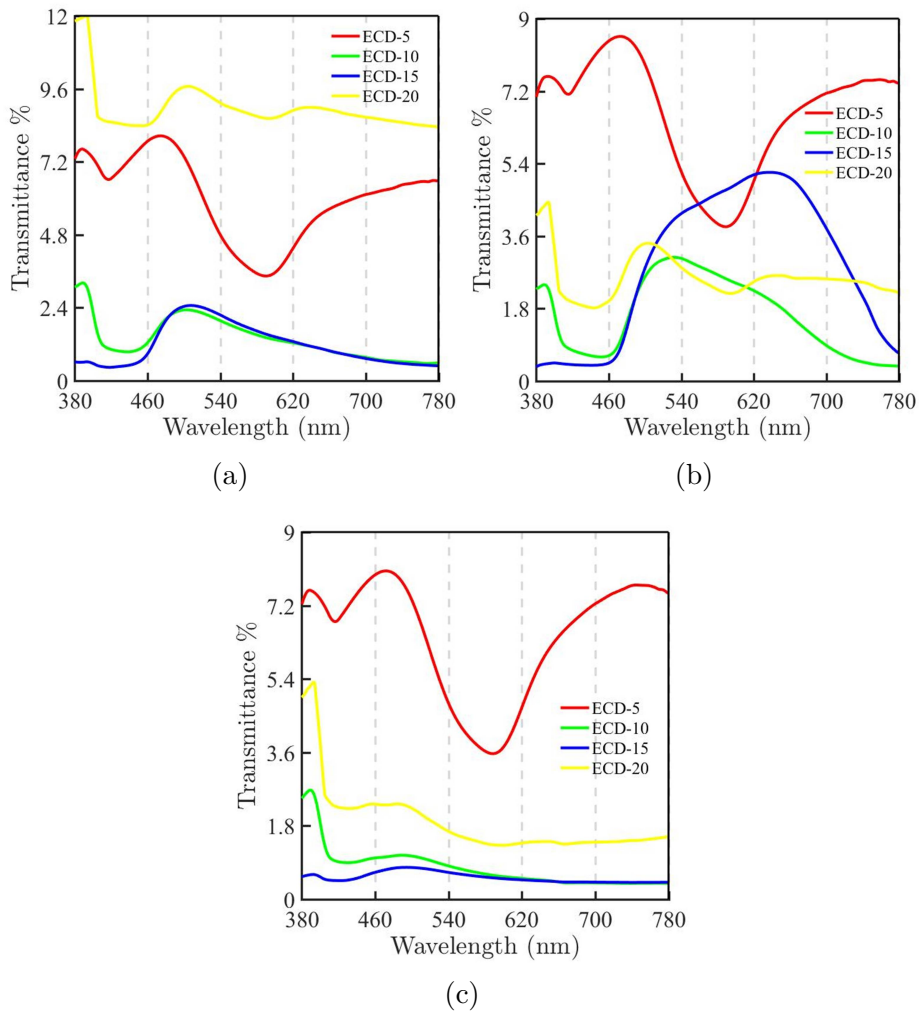


Figure 4.9: Transmittance vs wavelength spectra of all ECDs at (a) neutral, (b) reduced and (c) oxidized state.

of the green region. At the oxidation state (1.9 V), absorbance is increased in the green region and red region indicating lower absorbance in blue region. The transmittance of ECD-10 is relatively higher in the blue region. This results in a change of color from green to light green and blue for ECD-10 at reduction and oxidation states respectively. Similar observations are recorded for ECD-15 and ECD-20 in Figure 4.8c1 - 4.8c5, 4.8d1 - 4.8d5.

To gain insights into the variation in optical properties with thickness, transmittance spectra of all the ECDs at neutral, reduced, and oxidized states are compared in Figure 4.9. ECD-5 shows the different transmittance as a function of wavelength in comparison to other ECDs. At neutral state (Figure 4.9a), ECD-10, ECD-15, and ECD-20 have different transmittance with similar patterns. This observation reveals that ECD-10, 15, and 20 give different shades of the same color at a neutral state as also seen in photographic images presented in Figure 4.8. Similar trends are observed at excited states also (Figure 4.9b, 4.9c). However, according to the relation ($Absorbance = \log_{10}(100/(Transmittance\%))$) and Beer-Lambert's law, transmittance should decrease with the increase in thickness. Unlike the spectra of PANI film (Figure 4.5), the ECDs do not follow this trend in Figure 4.9. This may be due to the scattering of light from the polymer molecules present in the gel electrolyte. Nevertheless, the photographic images and spectra compared in Figure 4.8 and Figure 4.9 suggest that varying thickness of the PANI ECP layer is a feasible strategy to achieve varying shades of green and blue colors in ECDs.

The electrochromic performance of ECDs is further studied through color contrast and response time. Color contrast is evaluated from the transmittance spectra of different ECDs (Figure 4.8) using the Eq. (4.2) [53].

$$Color\ contrast = \frac{(T_1 - T_2)}{T_1} \times 100 \quad (4.2)$$

where T1 and T2 are the transmittance of ECD at different excited states. Table 4.2 presents the color contrast of all the ECDs at redox potentials. The color contrast of ECD-5, ECD-10, ECD-15, and ECD-20 between neutral and oxidation states is 16.80%, 56.04%, 69.21%, and 79.31% respectively. The relatively lower contrast for ECD-5 may be attributed to the thin ECP layer used in this case. The color contrast of ECD-10 is higher than ECD-5 and sufficient enough to distinguish between the colored states (see Figure 4.8). Color contrast increases for thicker PANI layers in ECD-15 and ECD-20 samples. As the thickness of the PANI layer increases, the path length of ion diffusion also increases and this may lead to better color contrast in these ECDs. The color contrast of all ECDs shows similar trends at reduction potential with the minimum color contrast of 14.11% for ECD-5. The color contrast increases to 41.76%, 79.41%, and 74.62% for ECD-10, ECD-15, and

ECD-20 respectively.

Response time of ECDs is defined as the time they take to achieve 60% of transmittance change at each potential. It is measured at the redox potentials for each ECD at 600 nm wavelength and given in Table 4.2. During reduction, response time increases with the increase in thickness of the PANI layer. With the increase in surface roughness (Figure 4.3), the contact area at the PANI/electrolyte interface increases and the diffusion coefficient decreases [170]. Consequently, the rate of diffusion of ions decreases with the increase in thickness. As discussed earlier (Figure 4.6b), better ion transport and diffusion take place for the lower thickness of PANI film. ECD-10 takes minimum time to achieve the maximum change in transmittance and response time increases for ECD-15 and 20. It is also observed that the response time at oxidation potential is more than the time required for switching at reduction state in all the ECDs. Lithium (Li^+) ion intercalates at a reducing state to balance the charge of the electrode while at oxidizing state, perchlorate (ClO_4^-) ion diffuses in the electrode. Due to the bigger size (240 pm) of ClO_4^- , it moves slower than lithium-ion (90 pm) and it may be the reason for the longer response time at the oxidation state.

4.3.7 Spectral colorimetric analysis

Spectral colorimetry analysis is performed next to quantify the shades of green and blue colors in ECDs. This will provide a deeper understanding of the ECP layer thickness effect on the optical performance of fabricated ECDs. Three attributes; hue, saturation (or chroma), and value, are the important parameters for quantification of a color. Hue contains the information regarding dominant wavelength associated with the color. Saturation or chroma defines the purity of the color and the third attribute, value, is associated with the brightness of the color [158]. All the possible colors can be arranged according to the three attributes and organized in a systematic way to represent graphically in two- or three-dimensional color spaces. These attributes are defined by the CIE color system and the most commonly used CIE color space is $L^*a^*b^*$ system [171]. Here, ' L^* ' represents the lightness with 0 as black and 100 as white. Negative ' a^* ' represents the green while positive ' a^* ' indicates the red color. Negative ' b^* ' indicates blue and positive ' b^* ' represents yellow color, as shown in Figure 4.10a. The transformation equations are given below,

$$L^* = 116\left(\frac{Y}{Y_n}\right)^{1/3} - 16 \quad (4.3)$$

$$a^* = 500\left(\frac{X}{X_n}\right)^{1/3} - \left(\frac{Y}{Y_n}\right)^{1/3} \quad (4.4)$$

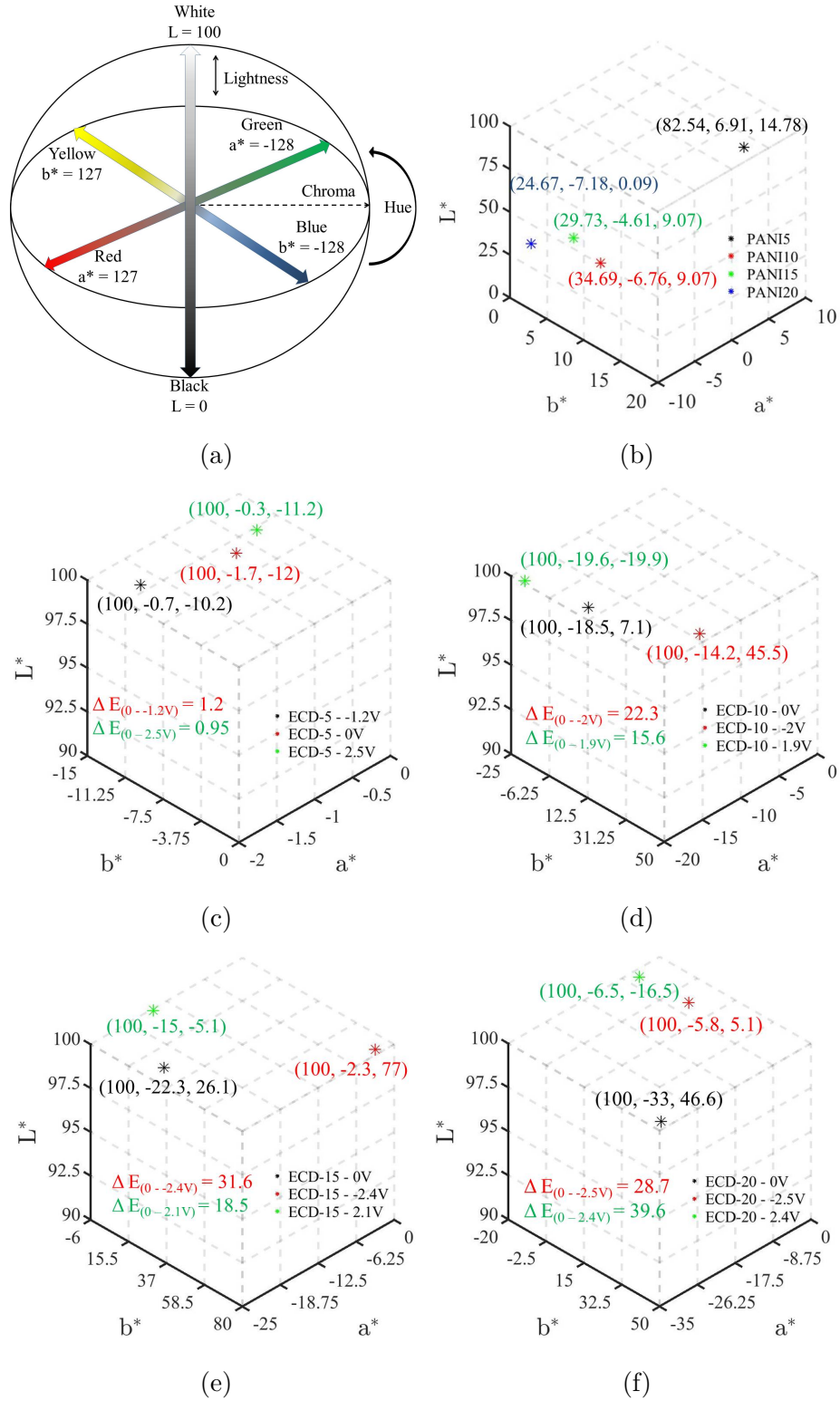


Figure 4.10: Photographic images at reduced, neutral and oxidized states (1-3), absorbance (4) and transmittance (5) spectra of (a) ECD-5, (b) ECD-10, (c) ECD-15 and (d) ECD-20 at their respective redox potentials.

$$b^* = 200\left(\frac{Y}{Y_n}\right)^{1/3} - \left(\frac{Z}{Z_n}\right)^{1/3} \quad (4.5)$$

Here X , Y and Z represent the tristimulus values (three values that are used together to describe color) of the material under consideration, and X_n , Y_n and Z_n represent the tristimulus values of a perfect reflecting diffuser under the same illumination conditions. These are obtained through color matching functions of standard observers using the following relations,

$$X = K \int_{380}^{780} R(\lambda)P(\lambda)\bar{x}(\lambda)d\lambda \quad (4.6)$$

$$Y = K \int_{380}^{780} R(\lambda)P(\lambda)\bar{y}(\lambda)d\lambda \quad (4.7)$$

$$Z = K \int_{380}^{780} R(\lambda)P(\lambda)\bar{z}(\lambda)d\lambda \quad (4.8)$$

Where, $K = 100 / \int_{380}^{780} R(\lambda)P(\lambda)\bar{y}(\lambda)d\lambda$; $\bar{x}(\lambda), \bar{y}(\lambda), \bar{z}(\lambda)$ are the color matching functions, $R(\lambda)$ is the spectral reflectance of the material and $P(\lambda)$ is the spectral distribution of the tungsten-halogen lamp. The parameters L^* , a^* , and b^* for various PANI layers are evaluated from their reflectance spectra (Figure 4.5f) in eqs. (3-5) and compared in Figure 4.10b. L^* is higher for the PANI5 and decreases with the increasing thickness of the PANI layer. Lightness (L^*) is the property of a surface that determines the percentage of light it reflects. Thus, the variation of L^* for different PANI samples agrees with the reflectance spectra shown in (Figure 4.5f). While the PANI5 sample with the highest reflectance shows maximum L^* , the other PANI samples have lower reflectance with L^* ranging from 34 to 24 for PANI10, PANI15, and PANI20 samples in Figure 4.10b. Both, a^* and b^* are positive for PANI5 (Figure 4.10b) while, a^* is negative and b^* is positive for PANI10, PANI15 and PANI20. Color coordinates of PANI5 show a relatively lower fraction of green color and a higher percentage of red color. This is similar to the peaks that appeared in the reflectance spectra of PANI5 (Figure 4.5f). Negative a^* for PANI10, PANI15, and PANI 20 shows the major fraction of green color as previously seen in the optical spectra and optical images (Figure 4.5). The value of b^* of PANI20 is near zero (center axis – gray line) and the only noticeable value is of a^* which means the presence of pure green color with the lowest lightness for the thickest film.

Color difference (ΔE) is another important parameter used to quantify the color of the PANI layer as a function of film thicknesses. ΔE between the colors of oxidized and neutral state and between reduced and neutral state is obtained from the following relation,

$$\Delta E = \sqrt{(\Delta L^*)^2 + (\Delta a^*)^2 + (\Delta b^*)^2} \quad (4.9)$$

Where ' ΔL^* ' is the difference of ' L^* ' coordinates, ' Δa^* ' denotes the difference of ' a^* ' coordinates and ' Δb^* ' represents the difference of ' b^* ' coordinates of two colors [159]. For a standard observer to notice the difference between the two colors, ΔE should be greater than 2 [172]. The ΔE for different PANI layers is evaluated using Eq. (9) and is shown in Figure 4.10c - 4.10f. The ΔE in Figure 10c are smaller than 2 and hence it is difficult for an observer to differentiate between the reduced, neutral, and oxidized state of the PANI5 layer. Thus, it is not suitable for the ECD applications. On the other hand, PANI10, PANI15, and PANI20 are better suited due to their sufficiently large ΔE between different excited states in Figure 4.10d - 4.10f respectively as also recorded in spectroelectrochemical measurements and photographic images in Figure 4.8. The comparison of L^* , a^* , b^* color coordinates and ΔE in Figure 4.10 suggest that it is possible to achieve varying shades of green and blue color in ECDs by varying the thickness of PANI ECP layer.

4.4 Conclusion

The present study demonstrates that it is possible to modulate the shades of green and blue color in ECD by varying the thickness of the PANI ECP layer from 250 nm – 650 nm. While the roughness increases, the porosity decreases with the increasing thickness of ECP layer. The reduced porosity of thick ECP layers causes hindrance to the ion diffusion and hence conductivity of ECD decreases from 2.5 mS/cm for ECD-5 to 0.1 mS/cm for ECD-20. Moreover, the ECP layer thickness also influences the redox potential due to the associated iR losses. Spectroelectrochemical measurements show that ECDs fabricated with varying thicknesses of PANI ECP layer are able to achieve different shades of green and blue at their corresponding redox potentials. It is recorded that a minimum thickness of the ECP layer (≥ 400 nm) is required to obtain any noticeable color change in ECD. Color contrast of ECDs ranges from 14 % to 80 % at both the excited states and it increases with an increase in the thickness of the ECP layer due to the longer ion diffusion path in thicker PANI films. For quantitative comparison, spectral colorimetry is performed and the color coordinates are calculated in CIE $L^*a^*b^*$ color space. $L^*a^*b^*$ color coordinates of PANI5, PANI10, PANI15, and PANI20 are (82.54, 6.91, 14.78), (34.69, -6.76, 9.07), (29.73, -4.61, 9.07) and (24.67, -7.18, 0.09) respectively. Color difference (ΔE) confirms the dependence of ECD color on the thickness of the PANI ECP layer except for the PANI5 layer. It is concluded that the thickness variation of the PANI ECP layer is a suitable strategy to develop shades of green and blue colors in ECDs. It is envisaged that the findings of the present work will be a significant step ahead towards the development of smart fabrics suitable for forest or greenish

surroundings.

Chapter 5

Design and fabrication of dual electrochromic device with broader color space

In the previous chapter, an ECD having a single PANI layer is limited to the narrow color spectrum displaying green and blue colors. It raises the requirement for developing the ECD capable of displaying the broader color spectrum. An ECD's color depends on the energy band gap of the ECP layer. Thus, it is possible to broaden the accessible color space by combining two (or more) ECPs in a single ECD. Here, we report the design and fabrication of dual ECD capable of displaying a broader color spectrum at different voltages. As a proof of concept, we have designed and fabricated dual ECD using two ECPs, polyaniline (PANI) and poly(3-hexyl thiophene) (P3HT). The dual ECD shows a wider color spectrum in comparison to the ECD prepared with only PANI or P3HT alone. Moreover, the color range of dual ECD depends on the arrangement of ECP layers with respect to the gel electrolyte (GE). While the number of colors in hybrid dual ECD (both ECP layers on one side of GE) are same as its redox states, the complementary ECD (GE is sandwiched between two ECPs) shows a much broader color range. In addition, the complementary ECD shows different colors on flipping the viewing side. A combination of these ECDs may be used to design displays with varying color ranges and color intensities. Comparative analysis reveals that the color contrast, response time, and coloration efficiency of complementary dual ECD is better than the hybrid dual ECD. On the other hand, the hybrid dual ECD shows better cyclic stability than the complementary dual ECD. Finally, the present study demonstrates a feasible strategy to widen the color space of conventional ECDs.

5.1 Introduction

An electrochromic device (ECD) is a layered structure that changes color under electrical stimuli [173, 137]. In an ECD, electrochromic (EC) and gel electrolyte layers are sandwiched between two transparent electrodes [174]. The redox reactions

under applied voltage alter the energy band gap of the electrochromic layer and induces color change in an ECD. Thus, the redox states of EC layer determine the color space of ECD. Different types of inorganic and organic electrochromic layers have been explored to achieve different colors in ECDs [139, 175, 24, 62, 176, 99, 53, 177, 178, 179, 180, 181, 182]. Among these, electrochromic polymers (ECPs) are currently preferred due to their flexibility, multicoloration, fast response time and high color contrast [46, 35]. Usually, multiple ECDs with different types of ECP layers are required to display varying colors in an application [135]. Therefore, ECDs capable of displaying color ranges beyond the redox states of an electrochromic layer are highly desirable.

Accordingly, the design and fabrication of an ECD with a broader color space are explored in this study. The idea explores the possibility of inducing multiple colors by combining two or more ECP layers in a single ECD. It is expected that the parent colors of individual ECP layers may combine/overlap to widen the color space of multilayered ECD. As a proof of concept, we have fabricated dual ECD using two ECP layers, polyaniline (PANI) and poly (3-hexyl thiophene) (P3HT). The distribution of two ECP layers with respect to the GE layer is an added design variable in dual ECDs. Therefore, two ECD configurations, complementary dual ECD (one ECP layer on either side of GE) and hybrid dual ECD (both the ECP layers on the same side of GE), are fabricated for the comparative analysis in this study. The architecture of four ECDs (two conventional ECDs with either PANI or P3HT ECP layer and two dual ECD configurations) considered in this work is schematically shown in Figure 2.3.

PANI and P3HT are preferred as these two are the most widely used ECPs. While PANI shows excellent environmental stability, low cost, and high conductivity [68], P3HT is a soluble and complementary polymer to PANI [61]. Moreover, PANI induces light green, green, and blue colors at reduced, neutral and oxidized states [52], P3HT displays magenta and cyan color at redox states [53, 42]. The colors of these two ECP layers are different and thus combining them may provide different colors in dual ECDs. To this end, the color space of reference ECDs having PANI or P3HT layers is compared with that of dual ECDs. Cyclic voltammetry and spectroelectrochemical measurements are performed to determine the color space of hybrid and complementary dual ECDs. The cyclic stability of ECDs is evaluated using chronoamperometry analysis. Experimental results reveal that while complementary dual ECD displays a broader color range, the hybrid dual ECD shows better cyclic stability. Finally, it is shown that combining multiple EC layers is a feasible strategy to broaden the color space of conventional ECDs.

5.2 Experimental Section

5.2.1 Materials and preparation

Four types of ECDs are fabricated in this work and their architecture is shown in Figure 2.3. Preparation of PANI film and gel electrolyte (GE) is done as per the details given in our earlier study [145, 183]. PANI film is electropolymerized using CV technique in the voltage range of -0.2 V to 1.2 V. P3HT and dichlorobenzene are purchased from the TCI chemicals and Loba chemicals respectively. 0.9 wt% of P3HT is mixed in the dichlorobenzene and stirred manually and the solution is spin-coated on ITO at 450 rpm for 90 s. ECD1 (Figure 2.3a) and ECD2 (Figure 2.3b) are prepared by sandwiching the GE between the ITO/ PET electrode and electrochromic films; ITO/PANI and ITO/P3HT; respectively. For ECD3 (Figure 2.3c), GE is sandwiched between the PANI and P3HT films. In ECD4 (Figure 2.3d), P3HT film is spin-coated on the electropolymerized PANI film and GE is sandwiched between the ITO/PET electrode and ITO/PANI-P3HT film.

5.2.2 Characterization

Cyclic voltammetry (CV) is performed on an electrochemical workstation (Metrohm Multi Autolab M204, The Netherlands). CV is used to evaluate the redox behavior of ECD in the voltage range of - 2.5 V to 2.5 V at the scanning rate of 20 mV/s and step potential of 2.44 mV. Cyclic stability is tested by using the chronoamperometry technique. Measurements are performed on software NOVA 2.1. All the experiments are carried out in potentiostatic mode. Atomic force microscopy (AFM) (Bruker, USA) analysis is performed in tapping mode on a scan area of 5 μm x 5 μm to measure the thickness of P3HT and surface roughness of all electrochromic films. Peak force and deformation measurements at a cross-section of PANI and PANI-P3HT films are performed in peak force quantitative nanoscale mechanical characterization (PQNM) mode using force volume imaging (FVI). PQNM mode is used to measure the thickness of PANI and PANI-P3HT films. The morphology of all the electrochromic films is studied before and after the cyclic stability test using a Field Emission scanning electron microscope (FESEM) (Jeol JSM7610 FPlus). In situ energy dispersive spectroscopy (EDS) is performed using a Bruker detector. Spectroelectrochemical measurements of ECDs are performed with an in situ UV-Vis spectrophotometer (Cary 60 of Agilent) electrochemical workstation (Keithley 2450).

5.3 Results and Discussion

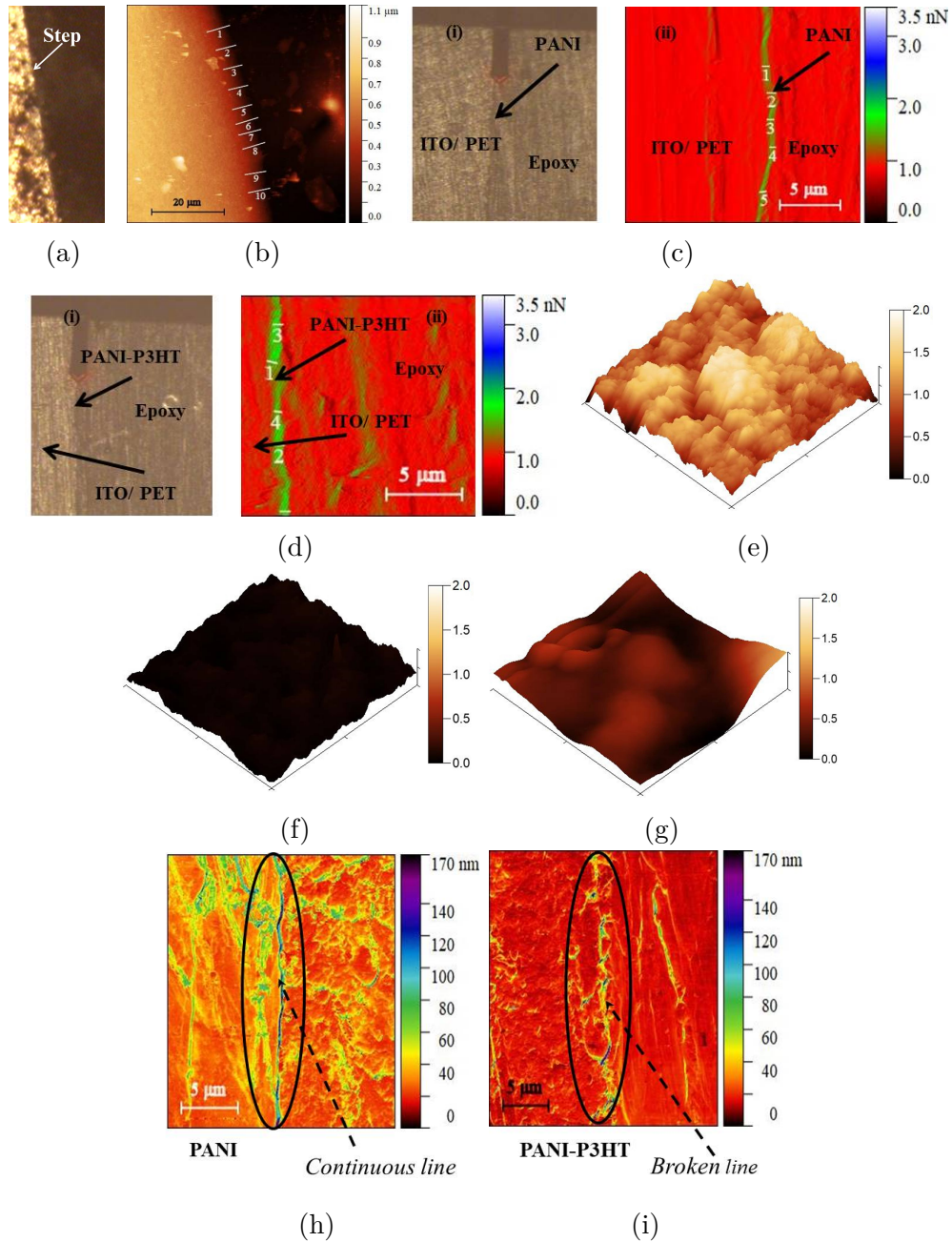


Figure 5.1: (a) Optical image showing the notch and (b) AFM micrograph of P3HT film with 10 readings using height to measure the thickness. Optical images and peak force measurement of a cross-sectional view of (c) PANI and PANI/P3HT films. AFM topographs showing roughness of (e) PANI, (f) P3HT and (g) PANI-P3HT and deformation measurement of (h) PANI and (i) PANI/P3HT.

5.3.1 Thickness, roughness and morphology of PANI and P3HT electrochromic films

The thickness, surface roughness, and morphology of ECP layers determine the performance of an ECD. Therefore, a detailed atomic force (AFM) and scanning electron microscopy (SEM) analysis of PANI, P3HT, and PANI-P3HT dual ECP layer are presented in Figure 5.1 and Figure 5.2. A step (Fig. 5.1a) is created during the deposition of ECP layers on the ITO substrate to measure their thickness. The average thickness of the P3HT layer measured from AFM tapping mode is found to be 310 ± 20 nm (Figure 5.1b). Due to the limitations of piezo scanner movement, the thickness of PANI and PANI-P3HT films are measured in PQNM mode. To perform the measurements, the cross-sectional side of PANI/ITO/PET and P3HT/PANI/ITO/PET sheets is cold mounted with epoxy (Figure 5.1c(i) and 5.1d(i)) and polished with a P1500 sandpaper. The average thickness is obtained from phase contrast micrographs shown in Figure 5.1d(i) and found to be 531 ± 31 nm and 593 ± 62 nm for PANI and PANI-P3HT layers. AFM topographs in Figure 5.1e, 5.1f and 5.1g shows that the surface roughness of PANI, P3HT and PANI-P3HT is 260 nm, 22 nm and 189 nm respectively. The relatively higher roughness of the PANI layer may be related to its deposition process. During electropolymerization, PANI grows at different sites on the ITO substrate which increases its surface roughness. PANI-P3HT dual ECP layer is prepared by spin coating P3HT on top of the PANI layer. The P3HT solution may diffuse inside the cavities of the PANI layer and hence reduce the roughness of dual ECP layer. To confirm this, the deformation of PANI/ITO/PET and P3HT/PANI/ITO/PET sheets obtained from AFM (PQNM mode) is compared in Figure 5.1h and 5.1i. A continuous line representing the PANI/ITO interface is observed in Figure 5.1h. On the other hand, Figure 5.1i shows a discontinuous line for dual ECP P3HT/PANI layer. It is expected that two continuous lines corresponding to the P3HT/PANI interface and the PANI/ITO interface will be present in this case. However, due to the diffusion of P3HT inside PANI, there will be no clear interface, and a single broken line may appear. The thickness of dual ECP layer- (593 ± 62 nm) is lower than the sum of PANI (531 ± 31 nm) and P3HT (310 ± 20 nm) ECP layers. This also implies the diffusion of P3HT in the PANI layer during the deposition of ECP layers.

Figure 5.2 shows the SEM micrographs of ECP layers. The PANI layer appears with porous microstructure in Figure 5.2a. The porous morphology of PANI layer may be responsible for its higher surface roughness observed in Figure 5.1e. Figure 5.2b shows the micrographs of P3HT fibers. These fibers get dissolved in spin coating solution and the surface of P3HT layer appears flat with no pores or cavities

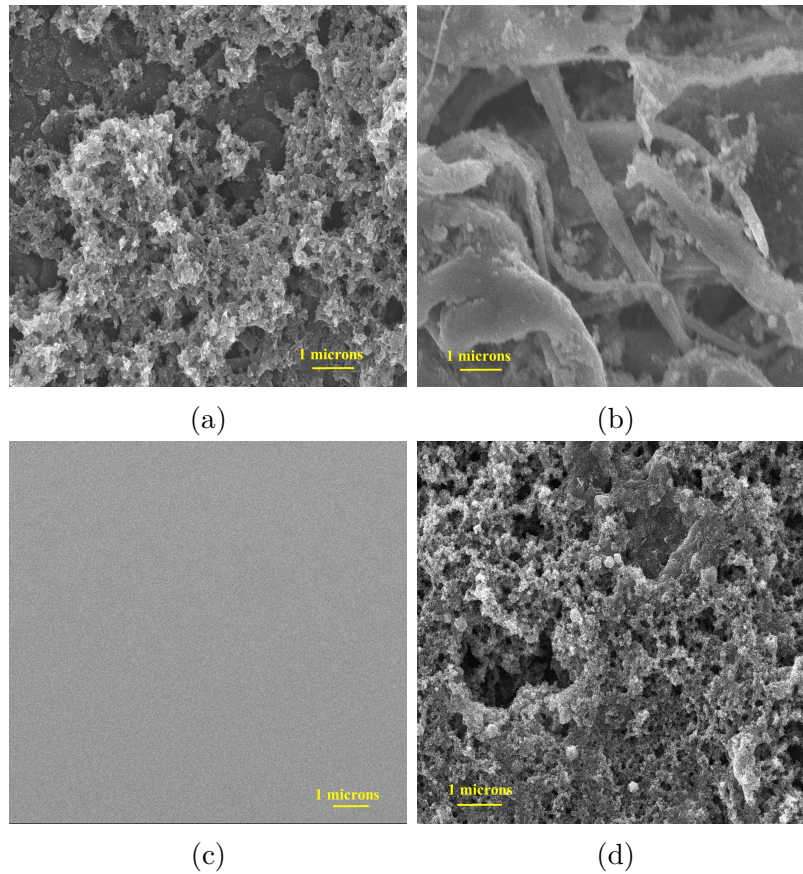


Figure 5.2: Morphology of (a) PANI, (b) P3HT fiber, (c) P3HT after spin coating and (d) PANI-P3HT films.

in Figure 5.2c. Morphology of PANI-P3HT dual ECP layer is shown in Figure 5.2d. The microstructure of dual ECP layer is similar to the PANI layer shown in Figure 5.2a albeit with a lower porosity. It may be attributed to the diffusion of P3HT in PANI layer in dual ECP layer.

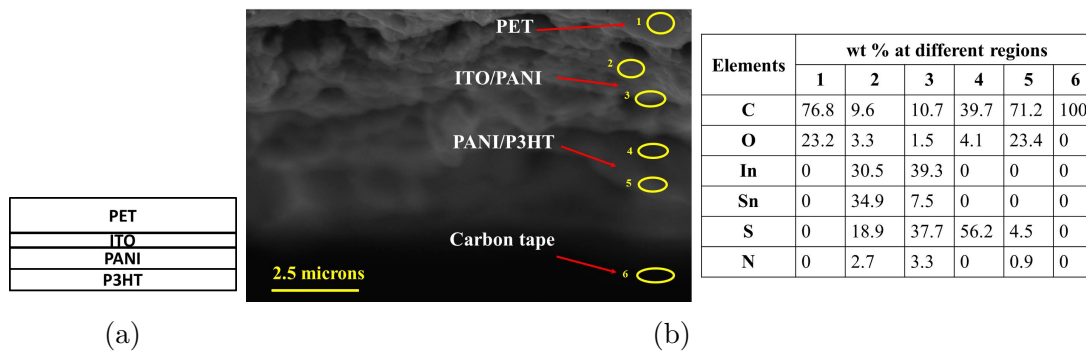


Figure 5.3: (a) Schematic of PANI-P3HT film (PET/ITO/PANI/P3HT) and (b) weight % of different elements is showing in different regions at cross-section of PANI-P3HT film.

Next, the energy-dispersive spectroscopic (EDS) analysis is performed on dual ECP to examine the diffusion of P3HT in PANI film. Schematic of PANI-P3HT

film coated on ITO/PET substrate is shown in Figure 5.3a. Figure 5.3b shows the weight % of elements present at different regions of the cross-section of PET/ITO/PANI/P3HT film. Region 1 has 'C' (Carbon) and 'O' (Oxygen) only due to the PET substrate. 'In' and 'Sn' along with other elements are found in region 2 and 3. PANI film is deposited on the ITO electrode therefore both are present in regions 2 and 3. The element 'N' is associated with PANI only and not with P3HT. While 'N' is present in region 2, 3 and 5, it could not be detected in region 4. This indicate that P3HT might be diffused and present in region 4. Hence, the signature of PANI (presence of 'N') is absent in region 4. Region 6 shows 'C' only due to the carbon tape used to stick the sample with the sample holder.

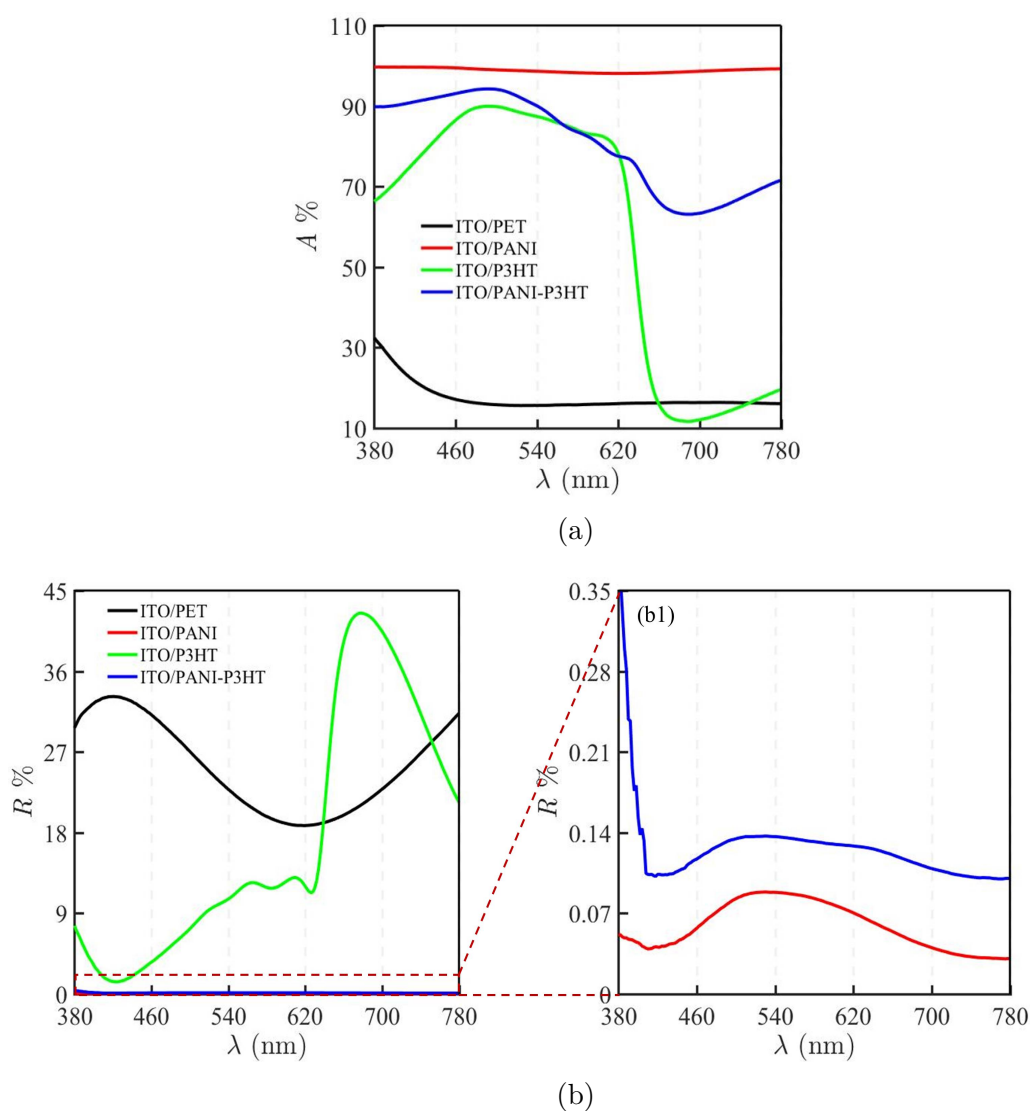


Figure 5.4: (a) Absorbance-wavelength and (b) reflectance-wavelength spectra of ITO/PET sheet, PANI, P3HT and PANI-P3HT films.

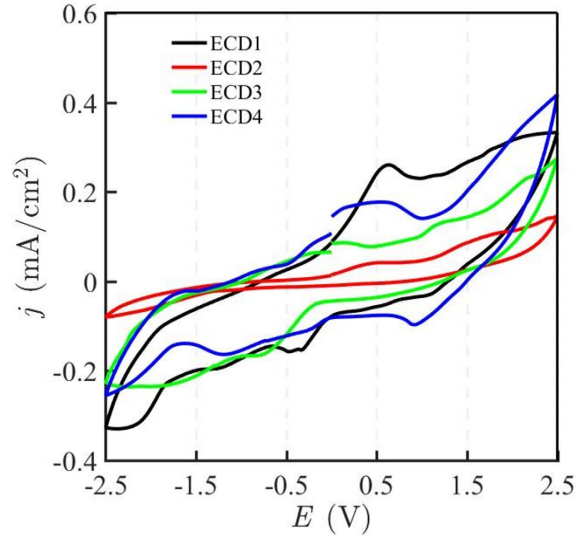


Figure 5.5: Cyclic voltammetry curve of ECDs.

5.3.2 Optical properties of PANI and P3HT electrochromic films

The optical response of ECP layers is studied by recording the absorbance-reflectance spectra with UV-Vis-NIR spectroscopy in Figure 5.4. The spectra of the ITO/PET sheet are also included as a reference. Absorbance-wavelength spectra in Figure 5.4a reveal low absorption (15%) of incident light in the ITO/PET sheet. The blue color of the ITO/PET sheet is due to a peak in the low wavelength region (Figure 5.4b). The deposition of the P3HT layer increases the absorption to around 90% in 460 - 620 nm wavelength. At higher wavelengths, the absorption capacity of P3HT coated ITO/PET sheet decreases to 15%. It may be due to the high reflectance of the P3HT layer in the red color (color of P3HT layer) region as observed in reflectance spectra of ECP layers shown in Figure 5.4b. In comparison to the P3HT layer, the relative improvement in absorbance is higher for the PANI layer. The coating of the PANI layer increases the absorbance of the ITO/PET sheet to 95% in the whole visible range. It may be attributed to the multiple scattering and trapping of incident light in the porous structure (Figure 5.2a) of the PANI layer. The absorption decreases to 90% or lower for the PANI-P3HT dual ECP layer. The diffusion of P3HT reduces the porosity and thus decreases the light-trapping capacity of the PANI layer. The reflectance spectra in Figure 5.4b corresponds to green color (maximum reflectance in mid-region) of the PANI layer and the red color (maximum reflectance at higher wavelength region) of the P3HT layer.

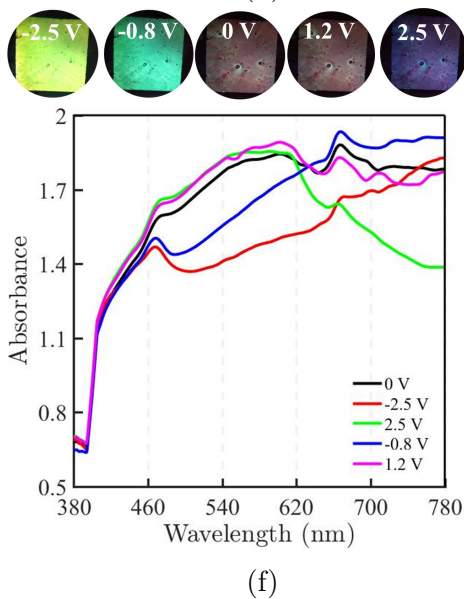
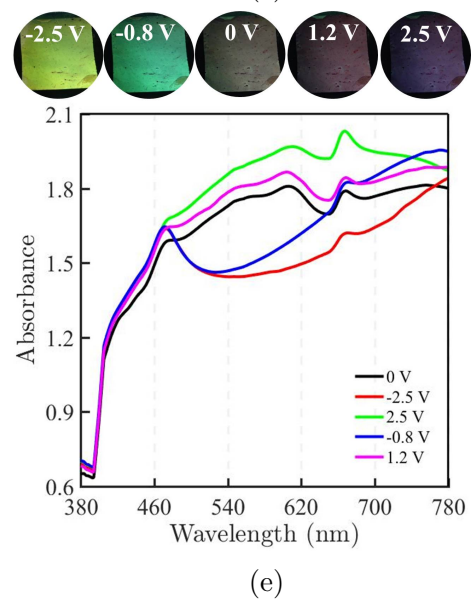
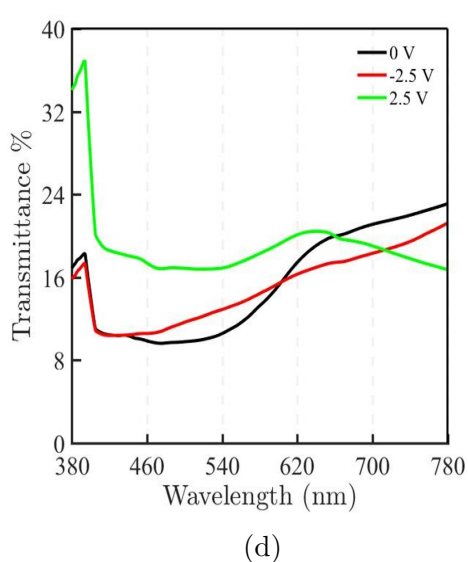
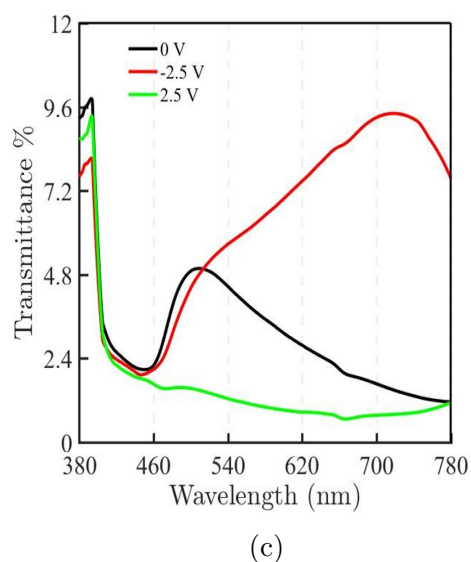
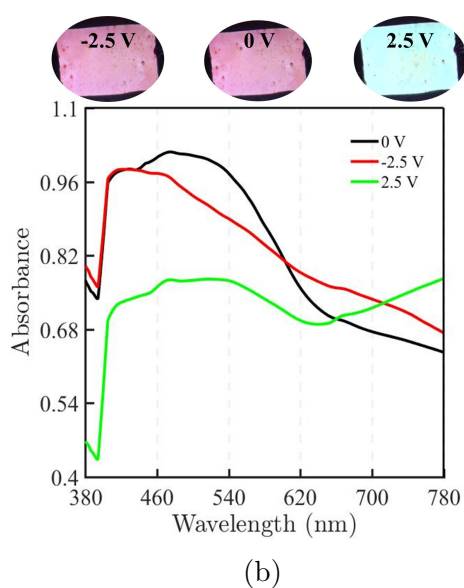
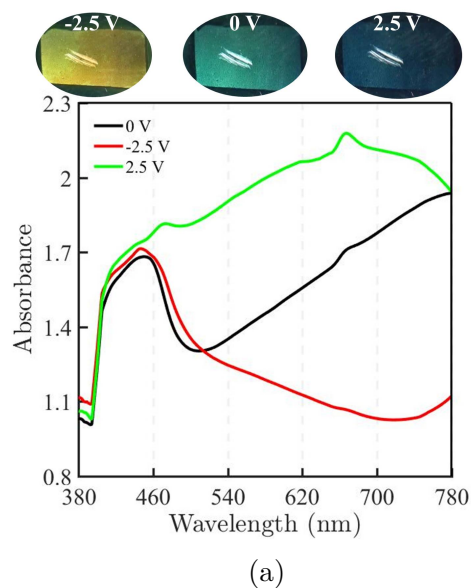
5.3.3 Electrochemical properties of ECDs

The UV-Vis-NIR spectroscopy analysis shows that the optical characteristics of the dual PANI-P3HT layer differ from the individual PANI and P3HT layers. Hence, the electrochemical properties of all four types of ECDs are characterized next. Figure 5.5 compares the cyclic voltammetry (CV) curves of dual ECDs with conventional ECDs having a single ECP layer. Maximum current density in ECD1 is recorded at 2.5 V and -2.5 V corresponding to the oxidizing and reducing states of the PANI layer. Since P3HT has only an oxidation state, ECD2 shows a relatively higher current density at +2.5 V. The porous structure of the PANI layer is better accessible to ions and hence ECD1 shows higher current density than ECD2. The ECD configuration seems to affect the current density of dual ECDs. The peak current density of complementary ECD (ECD3) is lower than that of hybrid ECD (ECD4). In ECD3, the PANI film oxidizes and the P3HT film reduces simultaneously as they are connected to different electrodes (Figure 2.3c). On the other hand, both the ECP layers in ECD4 are connected to the same electrode (Figure 2.3d) and thus they oxidize simultaneously. Consequently, the peak current density of ECD4 is higher than the ECD3 as well as base ECDs (ECD1 and ECD2).

5.3.4 Spectroelectrochemical properties of dual ECDs

Spectroelectrochemical measurements on ECDs are performed to evaluate the change in optical spectra at redox voltages. The color space of conventional ECDs is compared with the dual ECDs in Figure 5.6. The digital images of the ECDs at the applied voltages are also included. The Absorbance - wavelength spectra are recorded at -2.5 V, 0 V, and +2.5 V corresponding to the reduction, neutral, and oxidation states of the ECP layer. ECD1 shows low absorbance in the green color wavelength region at a neutral state (Figure 5.6a). At a reduction voltage of -2.5 V, the yellowish-green color of ECD1 is due to the low absorbance at a higher wavelength region. The absorbance of ECD1 increases in green and red regions and it appears blue at the oxidized state (+2.5 V). The peaks at 470 nm (2.6 eV) and 670 nm (1.8 eV) in ECD1 at +2.5 V are due to the polaron transitions [164]. ECD2 shows cyan color at 2.5 V and magenta at 0 and -2.5 V. Color at 0 V and -2.5 V is the same because it has only one oxidation state at 2.5 V (Figure 5.6b). The absorbance range of ECD2 is lower than ECD1 due to the higher absorbance of PANI film as discussed in the previous section (5.4a). The transmission spectra of ECD1 and ECD2 in Figure 5.6c and 5.6d are in accordance with their colors in the given potential range.

Absorbance spectra of complementary dual ECD (ECD3) (Figure 5.6e and 5.6f) are



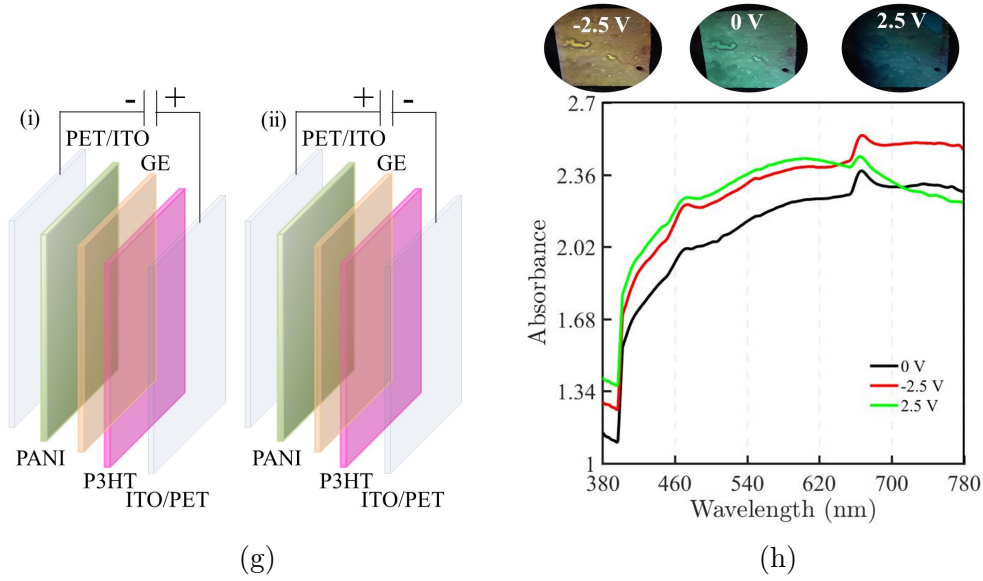


Figure 5.6: Absorbance-wavelength spectra of (a) ECD1, (c) ECD2, ECD3 from (e) side 1 and (f) side 2; and (h) ECD4. Transmittance-wavelength spectra of (b) ECD1 and (d) ECD2. (g) Schematic of ECD3 showing (i) negative and (ii) positive electrodes connected to the PANI layer.

recorded from side 1 and side 2 in Figure 2.3c. PANI film works as the working electrode in both measurements. From side 1 (PANI layer side, see Figure 2.3c), absorbance spectra at 0 V, -0.8 V, -2.5 V, 1.2 V, and 2.5 V are different from each other (Figure 5.6e). Digital images in the absorbance spectra (Figure 5.6e) show varying colors and shades of ECD3 at the given potentials. The absorbance spectra of ECD3 (PANI-P3HT complementary dual ECD) may be understood from the spectra of ECD1 (PANI layer) and ECD2 (P3HT layer). ECD1 and ECD2 show their original color at a neutral state. Their absorbance spectra differ in the wavelength range of 460 nm to 780 nm and they are affecting the spectra of ECD3 in the high and mid wavelength region respectively 5.6e. Even though, the colors of both the ECP layers contribute to the appearance of ECD3, the PANI layer seems to dominate in the digital images 5.6e. This is due to the fact that the PANI layer is towards the viewing side. When the negative electrode is connected with the PANI layer side (Figure 5.6gi), complementary P3HT film undergoes the oxidizing state. At -0.8 V and -2.5 V, the ECD3 spectra are similar to that of ECD1 at -2.5 V till 500 nm (Figure 5.6a) wavelength. Beyond this, the absorbance of ECD1 decreases and it transmits a larger fraction of light. The transmitted light is trapped by the P3HT film and the absorbance spectra of ECD3 are similar to ECD2 at -2.5 V in the larger wavelength region. However, due to the higher transmittance (Figure 5.6c) of ECD2 at 2.5 V, it does not contribute significantly to the visual appearance of ECD3 at negative voltages. At positive potentials (PANI layer is connected with positive electrode (Figure 5.6gii)), the spectra of ECD3 is similar to ECD1 (2.5 V)

up to the wavelength of 650 nm. At higher wavelengths, the absorbance spectra of ECD3 differ from ECD1 (2.5 V) and ECD2 (-2.5 V). The drop in the absorbance of ECD3 is relatively lower than in ECD1 and ECD2 after 650 nm. This implies that both the ECP layers contribute to the absorbance spectra of ECD3 beyond this wavelength. Unlike the oxidized state (2.5 V), the contribution of P3HT is significant at a reduced state (-2.5 V) due to its comparatively lower transmittance (Figure S1). The photographic images of ECD3 show the appearance of blue (ECD1) and magenta (ECD2) (magenta) at 2.5 V.

The color space of ECD3 is further characterized by recording the optical spectra from side 2 (P3HT film side, Figure 2.3c) in Figure 5.6f at varying voltages. As the P3HT layer is towards the viewing side, magenta color dominates in the side 2 image of ECD3 at 0 V. At the negative voltages, the ECD3 from side 2 appears similar to side 1. The green shade of PANI dominates in the digital images of ECD3. This may be due to the high transmittance (Figure 5.6d) of P3HT at positive voltage. The P3HT remains in a neutral state at negative voltages and thus it does not contribute in the color of ECD3 at negative voltages. However, the P3HT layer participates in the coloration of ECD3 and the absorbance spectra of ECD3 from side 2 differs from side 1 at positive voltages. The combination of images taken from side1 and side2 reveals that ECD3 shows a broader color space in comparison to ECD1 and ECD2. It is primarily due to the arrangement and variation in transmittance and absorbance of PANI and P3HT ECP layers in complementary dual ECD3. This observation supports the idea that the use of multiple ECPs in a single ECD is a feasible strategy to achieve colors that are more than the excited states of individual ECPs.

The effect of ECP arrangement in dual ECD is next studied by performing the spectroelectrochemical measurements on hybrid dual ECD4 in Figure 5.6h. The images of ECD4 show that it induces 3 colors which corresponds to the three excited states (2 for PANI and 1 for P3HT) of ECP layers. However, it is interesting to note that ECD4 shows a brown color at a reduced state (-2.5 V) which is not the parent color of either PANI or P3HT at any excited state (5.6h). Since both the ECP layers are placed on the same electrode, they reduce simultaneously at -2.5 V. At this voltage, P3HT shows magenta (Figure 5.6b) and PANI induces light green (Figure 5.6a) color. Magenta color has the components of red and blue primary colors. The brown color is formed by adding the light green color of PANI to the red and blue components of magenta P3HT. The mixing of these colors may be happening due to the diffusion of P3HT in the PANI layer during fabrication as pointed out in section 5.3.1. At neutral (0 V) and oxidizing state (2.5 V), ECD4 attains green and dark blue color. While PANI dominates at 0 V, both the ECP layers oxidize simultaneously to achieve a dark blue color (Figure 5.6h) at an oxidation state (2.5 V). Absorbance

Table 5.1: Comparing electrochromic properties of ECD1, ECD2, ECD3 and ECD4.

ECDs	Potentials (V)	Color contrast (%)	Wavelength (λ_{max})(nm)	Response time (s)	Wavelength (nm)
ECD1	0 - -2.5	72.1	550	24	700
	0 - 2.5	86.1	750	7.5	700
	2.5 - -2.5	92.3	667		
ECD2	0 - 2.5	43.8	450	13	515
	2.5 - -2.5	41	450	5.5	515
ECD3 (side 1)	0 - -0.8	47.4	550	9.5	600
	0 - 1.2	22	780	8	600
	0 - -2.5	53.6	603	6.5	600
	0 - 2.5	43.2	664	7.5	600
	2.5 - -2.5	67.6	607		
ECD3 (side 2)	0 - -0.8	39.2	543	15	600
	0 - -2.5	58	550	30	600
	0 - 2.5	60.1	780	15	600
	2.5 - -2.5				
ECD4	0 - -2.5	80.7	444	38	600
	0 - 2.5	64.2	775	27	600
	2.5 - -2.5	85.5	775		

in ECD4 is highest among all the ECDs in the whole visible range (Figure 5.6). It is attributed to the higher thickness (Figure 5.1d), multiple scattering, and light trapping in two ECP layers that are deposited on the same side of the electrode.

Electrochromic properties of conventional and dual ECDs are further investigated by comparing their Color contrast and response time in Table 3.2. Color contrast quantifies the variation in colors at different excited states and it is obtained from the transmittance spectra using the relation,

$$Color\ contrast(\%) = \frac{(T_1 - T_2)}{T_1} \times 100. \quad (5.1)$$

where T_1 and T_2 are the transmittance of ECDs at different excited states. Minimum 20% color contrast is required to accurately differentiate the colors at redox states [62, 176, 104, 74, 184]. ECD1 shows the maximum color contrast of 72.1 % and 86.1 % at the wavelength λ_{max} of 550 and 750 nm for reduced (-2.5 V) and oxidized (2.5 V) states respectively. Color contrast of ECD2 is found at 43.8 % at 450 nm between neutral and oxidized states. Similar color contrasts of conventional ECDs fabricated with PANI and P3HT layers are reported in the literature [173, 53, 42, 74, 65, 185]. The color contrast signifies that color recognition is better in PANI than in P3HT at different excited states. This may explain the domination of the PANI layer in dual ECDs observed in absorbance spectra and digital images (Figure 5.6). The

color contrast of ECD3 is evaluated for both side 1 and side2. It varies in the range of 22% to 60% at different voltages with a general observation of increasing contrast at higher voltage. ECD4 shows a color contrast of more than 60% at reduced and oxidized states. Thus, both the dual ECDs show shades of colors that are easily differentiable due to sufficiently high color contrast at all the applied voltages.

Response time ' τ ' quantifies the speed of color modulation in ECDs. It is defined as the time ECD takes for 65 % of the total transmittance change at λ_{max} . Response time of ECD1 and ECD2 agrees well with the reported literature [173, 175, 186]. The response time of ECD3 from side 1 (PANI side) is lower than from side 2 (P3HT). The color change in ECD3 is faster from the PANI side due to the higher color contrast of PANI (ECD1) than P3HT (ECD2). ECD4 takes the highest time among all the ECDs to respond to any color change. The thicker dual ECP layer in ECD4 increases the path length and thus delays the ion intercalation. This leads to a relatively higher response time in ECD4 in comparison to other ECDs. Coloration efficiency η_{ce} is another important criterion to assess the performance of ECP layers and ECDs. It estimates the change in optical density $\delta(OD)$ per unit of charge (Q) intercalated from the EC layer using the following equation,

$$\eta_{ce} = \frac{\Delta OD}{Q}. \quad (5.2)$$

where $\delta(OD)$ is related to the absorbance at neutral A_n and excited A_e states $\Delta OD = A_n - A_e$ and Q is the charge density. η_{ce} of ECD1 (45 cm²/C) and ECD2 (104 cm²/C) is similar to the reported values in literature for conventional ECDs [175, 104, 65, 187]. Coloration efficiency of ECD3 (60 cm²/C) lies within the η_{ce} of ECD1 and ECD2 due to the complementary arrangement of PANI and P3HT layers. η_{ce} decreases to 17 cm²/C when both the ECP layers are put together on the same side of electrode in ECD4. The thicker dual ECP layer in ECD4 hinders the ion intercalation and hence higher energy is required for color modulation in ECD4. The repeated cycles of ion inter- and de-intercalation may degrade the performance of ECDs in-service conditions. The cyclic stability of conventional and dual ECDs is studied using chronoamperometry. While ECD1, ECD2, and ECD4 are tested at 2.5 V and -2.5 V, voltages of 2.5 V, 1.2 V, -0.8 V, and -2.5 V are applied in ECD3 to record the variation in current density with time. Figure 5.7 shows that the current density decreases with increasing cycles for all the ECDs. While the stability of ECD1 is 3-4 cycles (Figure 5.7a), ECD2 suffers 80 % current drops after 15 cycles (Figure 5.7b). The cyclic stability of ECD3 is similar to that of ECD2 and it shows 80 % current density drops after 11 cycles (Figure 5.7c). It may be due to the better cyclic stability of the P3HT layer present in ECD3. The hybrid arrangement of ECPs in ECD4 records better stability with current drop after 30 cycles (Figure 5.7d). To

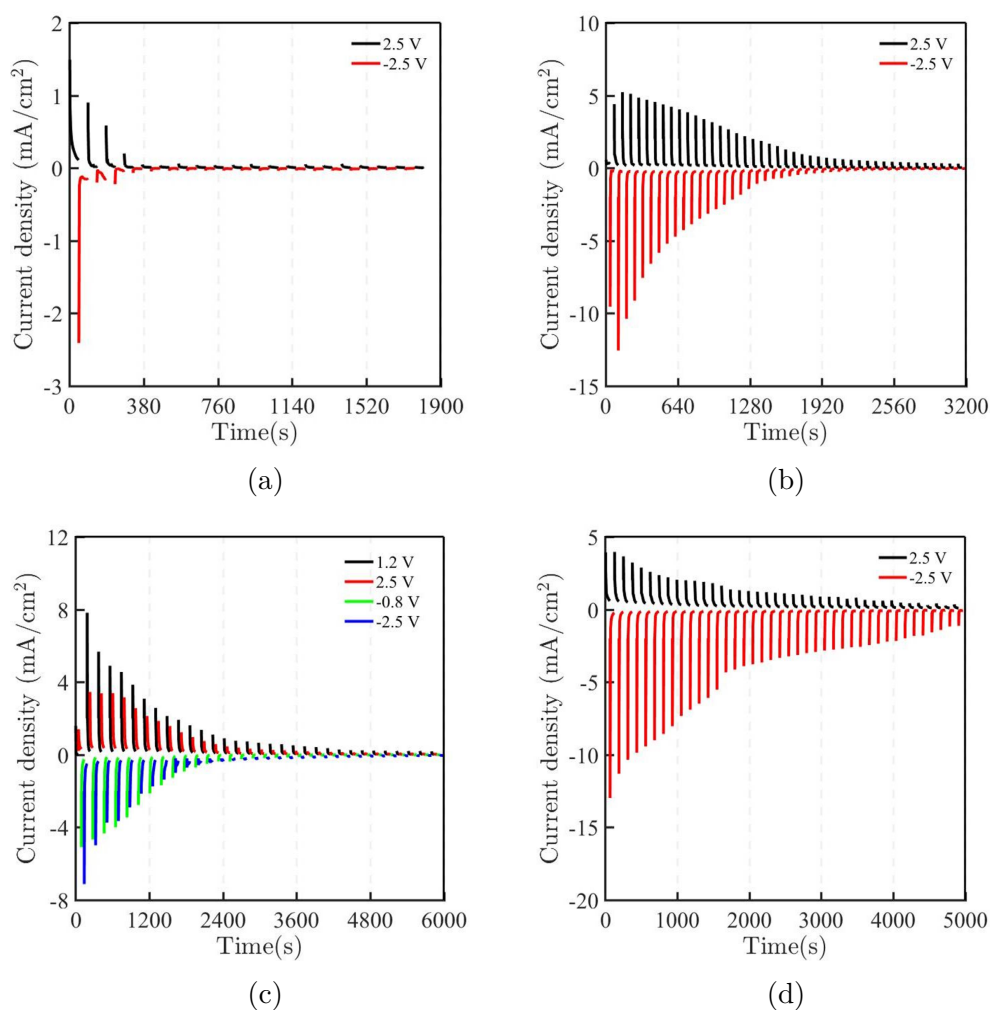


Figure 5.7: Current density -time curve of (a) P8, (b) P3, (c) P8GEP3 and (d) P8P3 to find the cyclic stability.

understand this, the microstructure of PANI and P3HT films is investigated after the cyclic stability tests in Figure 5.8. Figure 5.8a reveals that the porosity of the PANI layer has reduced after the tests in comparison to its microstructure before the test in Figure 5.2a. A similar change in the microstructure is observed in the P3HT layer after the test (Figure 5.8b). The hybrid dual ECP layer of PANI-P3HT shows a reduction in the porous structure and the presence of void-like damage in its microstructure after the test in Figure 5.8c. The degradation in microstructure may be attributed to the intercalation and deintercalation of ions in the ECP layer. During intercalation and deintercalation of ions into the electrochromic material, there is a change in the volume of structure which induces mechanical stresses and results in a change in microstructure. Porosity and large cavities in microstructure are reduced after cyclic stability. The same observation is found on comparing the morphology of pristine PANI-P3HT hybrid film (Figure 5.2d) and after the cyclic stability test (see Figure 5.8c).

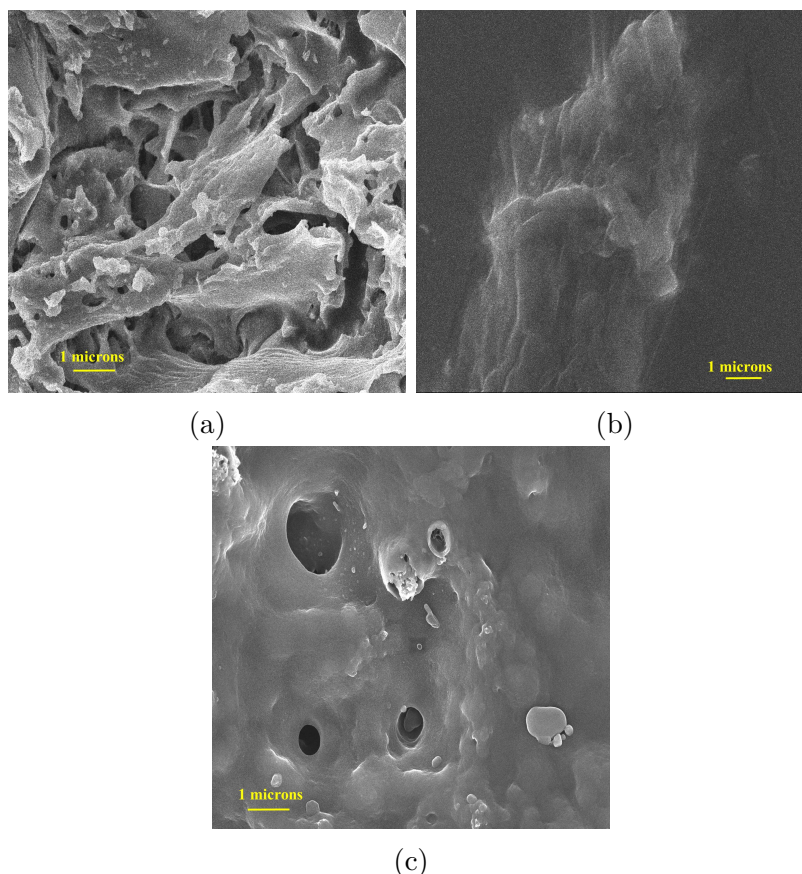


Figure 5.8: Morphology of (a) PANI (P8), (b) P3HT (P3) and (c) PANI/P3HT (P8P3) films after the cyclic stability test.

5.4 Conclusion

The color space of conventional ECDs is limited due to the single ECP layer used to fabricate them. This study demonstrates a feasible strategy to broaden their color space by integrating multiple ECP layers in a single ECD. To this end, two ECP layers, PANI and P3HT, are used to design and fabricate dual ECDs that are able to access a wider color domain than conventional ECDs. Electrochemical characterization reveals that the color space of dual ECD depends on the arrangement of two ECP layers. The complementary dual ECD configuration (GE is sandwiched between the two ECPs) provides a larger color spectrum than the hybrid dual ECD configuration (both the ECP layers are deposited on the same side of an electrode). The diffusion of P3HT into PANI layers induces a brown color which is different from the parent colors of PANI and P3HT. Moreover, the response time of complementary dual ECD is found to be lower than the hybrid dual ECD. However, the hybrid configuration shows better cyclic stability than the complementary configuration of dual ECDs. It is envisaged that even though only two ECP layers are used here as a proof of concept, the idea may be extended to

include more ECP layers to improve the color space of conventional ECDs. The poor cyclic stability of the dual ECDs needs to be investigated in future work. The findings of the present study will be useful in designing better display panels, smart textiles, etc.

Chapter 6

Bio-inspired active camouflage device: A modular design approach

Self-healable ECDs are developed for a broader spectrum in the previous chapters. It is required to utilize them to achieve the last objective. This chapter includes the design and development of the device capable of achieving active camouflaging in forest vegetation. The concept of modularity is used here to design the active camouflaging device (ACD) and present the prototype for the proof of concept. ACD is the integrated system of pattern detection algorithm (PDA) and pattern formation hardware (PFH). PDA collects the information of surrounding using digital images and converts it into the modular image (*MoI*) and PFH is capable of generating patterns accordingly using electrochromic modular architecture (*MoE_A*). Different types of electrochromic devices (ECD) are used as the modules in *MoE_A* to give the green and brown color shades at different excited states. Further simulation is performed to get the desired applied voltage for the particular surroundings to achieve the best-suited color shade of ECDs. The similarity in the patterns formation of *MoI* and *MoE_A* is also evaluated under two types of light sources: skylight and sunlight. It is found that the proposed concept achieves better active camouflaging under skylights than sunlight using visual inspection and SSIM performance measures. Then, PDA and PFH are integrated to form the ACD and the simulated results are used as input signals to dynamically change the patterns with varying the surroundings. The proposed concept in this thesis is found to be a feasible strategy for achieving active camouflaging for applications such as surveillance, wildlife discoveries, etc in forest vegetation.

6.1 Introduction

The survival probability of personnel and other assets in a hostile environment critically depends upon their ability to camouflage themselves in the natural surroundings. Fundamentally, camouflaging is of two types; passive and active. Passive camouflage refers to matching colors, contours, patterns, or texture of the object with the surroundings, e.g. patterning of security personnel uniforms,

equipment and landscapes, etc. One of the major drawbacks of passive camouflage is that it needs to be uniquely designed for each type of surrounding, making it less cost and time-effective. On the other hand, active camouflage refers to the dynamic phenomenon where an object changes its color or texture to blend with the surroundings. The major application of active camouflaging is found in surveillance, security of personal assets, and wild-life discoveries. Most of the applications are associated with the forest surroundings. It is observed that many natural species blend with the environment by changing their color and/or texture. Some of the examples are paradise whiptail [2], cephalopods [6, 7], chameleons [12], leptocephallis etc. Curiosity-driven understanding of natural materials/species has led to advancements in many technologically important areas and developing artificial camouflage is no exception. These natural species offer a clue to design an artificial camouflage strategy to cater to our security needs. Artificial chromatophores and protochromic devices are developed with the cephalopods' skin-inspired design [8, 9, 10, 11]. Chameleon-inspired structural-color actuator, bimetallic nanodot arrays and the soft robot work on the vapochromism and thermochromism [13, 14, 17]. Utilization of vapors and thermal energy is not feasible for the remote application. Taking a clue from *Leptocephallis* larvae, transparent actuators are developed to camouflage in water [3, 4]. Poly dimethyl siloxane (PDMS) based transparent structural film mimics the transparent wings of insects [5]. Application of transparent materials in the field of camouflaging is limited to the under-water.

Other than bio-inspired materials, researchers have also tried some other strategies to achieve camouflage by dynamically changing the texture. Controlled bistable silicon cells were prepared with locally reinforced regions for morphing application [15]. The use of synthetic tissue groupings was reported which allows the programmable transformation of two-dimensional stretchable surfaces into targeted three-dimensional shapes [16]. Due to the presence of a multitude of variations in the colors of natural vegetation, a change in texture is not sufficient without the association of colors. Efforts are also being taken to evolve the color-changing strategies such as by using liquid dye, a microfluidic network was developed for camouflaging [18] which may have the leakage issue. Moreover, a color-changing device is also developed based on the plasmonic effect that works on applying pressure [19]. Silicon metastructure is utilized to change the color from green to orange on stretching [20]. Chou et al. developed a stretchable electronic skin using electrochromic materials that work on tactile testing [23]. Existing color-changing devices are associated with a lack of pattern formation and some of them require high input power.

Even though there are few studies on the design of materials with active camouflage

abilities, their applications are rather limited, due to the associated complexity and lack of modularity. Moreover, reported camouflaging materials are not likely to be associated with the information of surroundings. Therefore, there is a need to develop a unified solution that is capable of detecting the surroundings and then adapting accordingly to provide effective camouflaging. Developing such a modular strategy using a multitude of analytical and experimental tools is the main objective of the present study. To this end, a detailed study is performed to design, fabricate, and characterize a device capable of performing active camouflage in forest surroundings or green vegetation by sensing and adapting accordingly. The concept of developing an active camouflage device (ACD) is realized through the development and integration of the pattern detection algorithm (PDA) and pattern formation hardware (PFH). PDA is developed to gather the information of surroundings and PFH enables the dynamic pattern changes based on the environment. PDA and PFH both use the concept of modularity to provide the capability of different pattern formations in ACD. In addition, the concept of modularity provides ease of fabrication, easy replacement, etc.

6.2 Materials and method

6.2.1 Fabrication of electrochromic device (ECD)

A PANI-based electrochromic device is fabricated by the method reported earlier [145]. 0.2 M of distilled aniline is added to the 0.2 M of H_2SO_4 to prepare the monomer solution. ITO-coated flexible PET sheet is dipped in the monomer solution and electropolymerization is performed using cyclic voltammetry (CV) technique for 10, 8, and 6 cycles to prepare three PANI-based modules (M^1 , M^2 , and M^3). For M^4 , P3HT is purchased from TCI chemicals and spin-coated at 450 rpm for 75 s on the electropolymerized PANI film. Then, Gel electrolyte (GE) is prepared by the method reported by us earlier [183]. In the end, GE is sandwiched between the ITO/PET and PANI/ITO/PET electrodes to prepare the M^1 , M^2 , and M^3 . While M^4 is fabricated by sandwiching the GE layer between ITO/PET and P3HT/PANI/ITO/PET sheets.

6.2.2 Characterization

Cyclic voltammetry (CV) is performed using an electrochemical workstation (Metrohm Autolab). Spectroelectrochemical measurements are performed using electrochemical workstation in situ UV-Vis spectroscopy (Keithley). Digital images are captured using a camera (Sony). The code is prepared on the MATLAB R2022b.

6.2.3 Development of active camouflage device

Active camouflage device (*ACD*) is prepared by integrating the electrochromic modular architecture (*MoE_A*) and the modular image (*MoI*) (Figure 2.4a). The casing of *MoE_A* is prepared by the 3-D printing. The drawing of the casing is prepared on the Solidworks as shown in Figure 2.4b. Casing contains the 25 (5 x 5) holes of size 1.5 cm x 1.5 cm and the back cover is provided to protect the modules with the arrangement of wire connections. Modules are placed in all the cavities such that the PANI/ITO/PET and P3HT/PANI/ITO/PET electrodes are toward the viewer. A 3 V power supply is connected to each module using Duracell batteries. 10-ohm and 47-ohm resistors in series are used to lower the potential to 2.5 V. Each module is connected to the two relay modules for switching the required potentials. The pattern detection algorithm is controlled by the input parameters using Arduino MEGA2560. Each relay is connected to one digital pin of Arduino and two pins are assigned to one module; one for 2.5 V and another for -2.5 V.

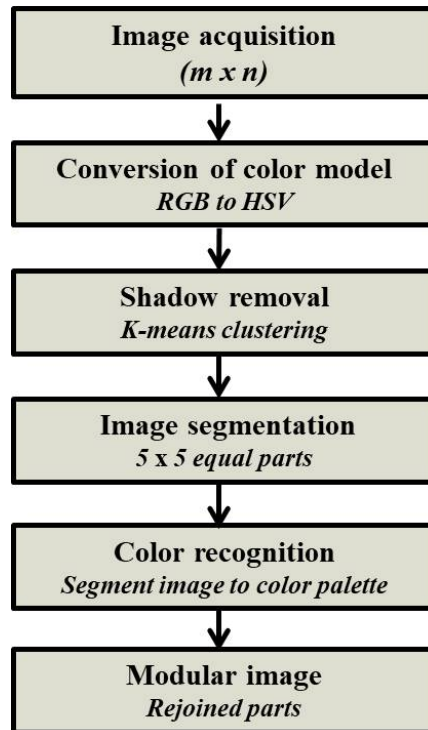


Figure 6.1: Flow chart of pattern detection algorithm.

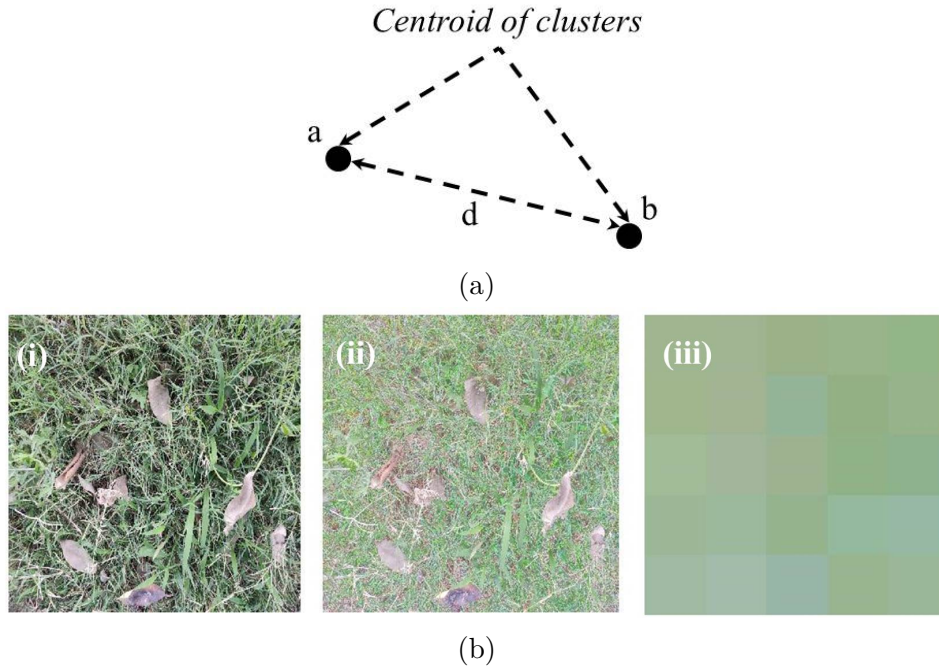


Figure 6.2: (a) Showing difference ‘ d ’ between centroid of two clusters ‘ a ’ and ‘ b ’ in k-means clustering algorithm and (b) comparing (i) original image, (ii) image after shadow removal and (iii) modular image of green surroundings.

6.3 Results

6.3.1 Pattern detection algorithm: an environment representation

Understanding of natural active camouflaging phenomena is necessary to develop synthetic materials. There are two important requirements highlighted from the fascinating phenomena of natural camouflaging. The first important requirement is the ability to sense the surroundings and another one is to achieve pattern formations accordingly. Pattern detection algorithm (PDA) is developed to fulfill the first requirement, which collects the information of surroundings and processes it to make it appropriate for the PFH so that the patterns can be changed accordingly. The flow diagram of the algorithm is shown in Figure 6.1. In the first step of image acquisition, digital images of surroundings are captured by the camera. Since image size ($m \times n$) depends on the configuration of the camera, images are resized to 2520×2520 pixels using the bicubic interpolation method to make the PDA camera independent. The bicubic interpolation method uses the weighted average of the 16 closest neighboring pixels to calculate the pixel values of resized images. Image acquisition is performed in RGB (Red, Green, Blue) color space in MATLAB. Color information in RGB color space is described by the intensities of Red, Green, and Blue components.

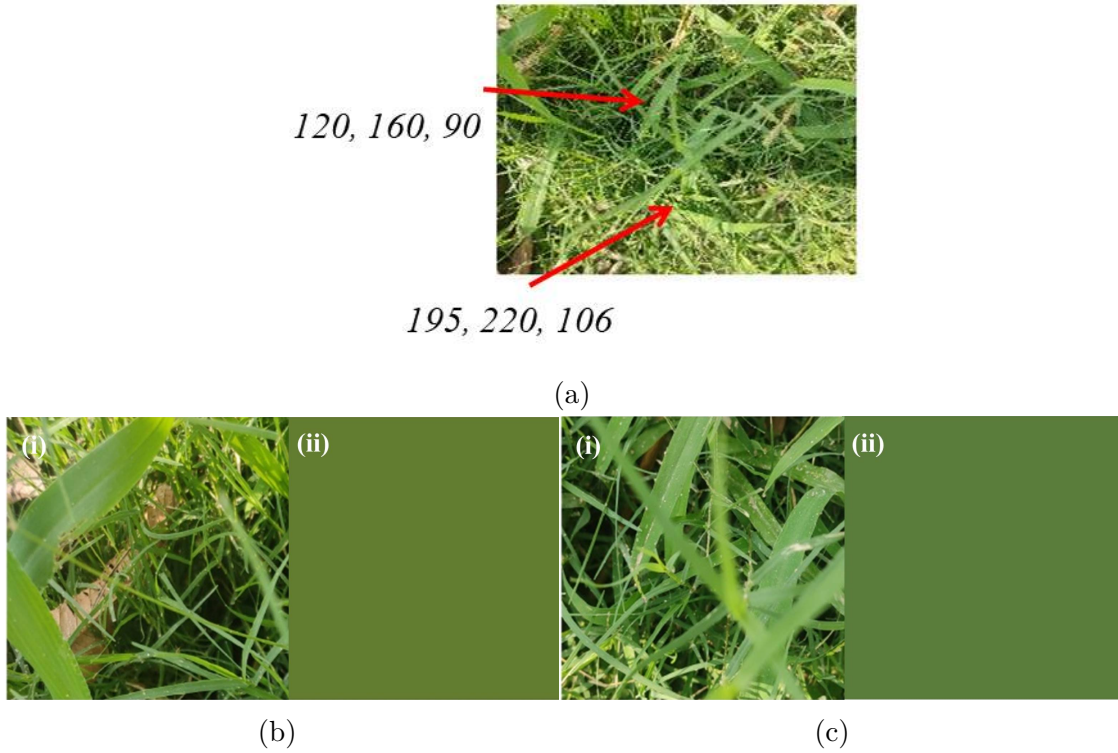


Figure 6.3: (a) Image of forest vegetation showing multiple shades of green color. Two points showing different RGB color coordinates, (b) and (c) are the examples of (i) segmented part of surrounding image and (ii) color recognition from segmented part.

Red, Green, and Blue components contain the combined information of pure color and brightness which makes it difficult to analyze both the features separately. To overcome this issue, images are converted into the HSV (Hue, Saturation, Value) color space which separates the information of hue (color) and value (brightness). In line with the focus of this study on greenish surroundings, digital images of grass leaves are captured. Shadows of grass leaves are hard to detect by the naked eye but distort the color information of images. As a result, the shadow removal algorithm is performed in the next step. Since the shadow is dependent on the brightness of the pixels, the shadow removal algorithm is applied to the V (value) channel of HSV color space. k-means clustering algorithm with 2 clusters is applied to remove the shadow of grass leaves. The purpose of the two clusters is to differentiate the bright and dark pixels. Say, $a > b$, 'a' and 'b' are the centroids of bright and dark pixels respectively and their difference 'd' is calculated by $d = a - b$ (Figure 6.2a). The difference 'd' is added to the intensity of dark pixels; $Iv_{new} = Iv_b + d$, where Iv_{new} and Iv_b are the new and old pixel intensities of dark pixels in V channel respectively. The original image compared with the image after removing the shadow is shown in Figure 6.2.

Forest vegetation contains many green color shades in leaves (Figure 6.3a) which

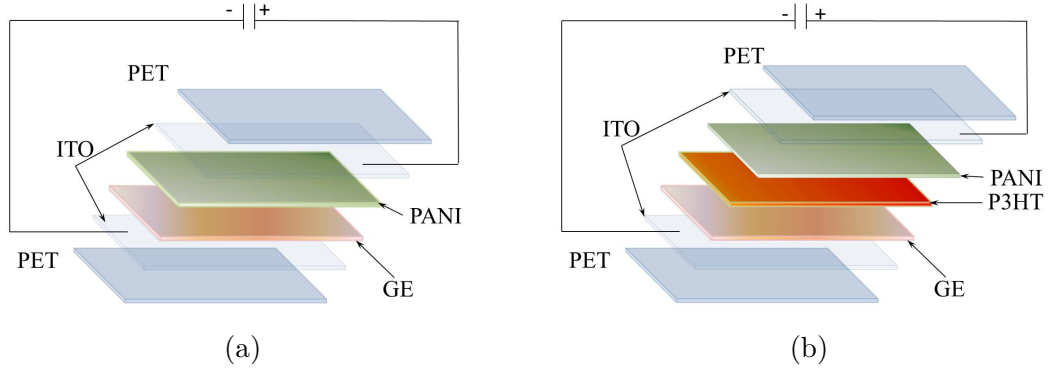


Figure 6.4: Schematic of (a) M^1 , M^2 and M^3 (3 types of PANI thickness); and (b) M^4 (PANI-P3HT) modules.

arises the requirement to collect the surrounding information in bits and pieces. This observation encourages to perform image segmentation and gather the surrounding information in small parts. During image segmentation, one of the limitations is that pixels can not be split into fractions. Keeping this in mind, the image is resized to 2520×2520 pixels in such a way that image segmentation is possible for all arrangements of x and y belongs to 1:10, where x and y are number of segmented parts in row and column respectively. By choosing this size, color information is possible to extract by segmenting the surrounding information into 100 arrangements. More numbers of arrangements are possible by increasing the image size ($m \times n$). The size of the segmented part is $p \times q$, where $p = m/x$ and $q = n/y$. Here, one of the arrangements is chosen to validate the concept. The image splits into 25 equal parts in the arrangement of 5×5 ($x = 5$ and $y = 5$). Every segmented part has $p \times q$ pixels and transmits the signal to modules of PFH for modulation of pattern formations. So, there is a requirement to assign a single color value to each segmented part. In the next step, a single color value is assigned to each segmented part by averaging the intensities of hue, saturation, and value separately given below and termed as color recognition (see Figure 6.3).

$$mean = \frac{\sum_1^q \sum_1^p I}{p \times q} \quad (6.1)$$

where I is the pixel intensity. After color recognition, all the segmented parts are re-joined in the same order of splitting to form a modular image (MoI) (Figure 6.2(iii)). MoI is a digital representation of the environment and the color information of every segmented part is transmitted to the modules of another unit of active camouflage device to achieve the pattern formations accordingly.



Figure 6.5: Four types of modules are arranged in electrochromic modular architecture.

6.3.2 Pattern formation hardware: an array

Pattern formation hardware (PFH) is developed to generate the patterns according to the information shared by the PDA, it fulfills the other requirement of an active camouflage device. The purpose of pattern formation is fulfilled by using modules. It consists of 25 modules in the arrangement of 5×5 , similar to MoI. Each module is an electrochromic color-changing layered device that changes the color on the application of voltage. Electrochromic polymer (ECP) is responsible for modulating the color of modules due to changes in excited states at different voltages. Polyaniline (PANI) and poly (3-hexyl thiophene) (P3HT) are used as ECPs to fabricate the four types of modules (Figure 6.4). The arrangement of four types of 25 electrochromic modules of size $1.5 \text{ cm} \times 1.5 \text{ cm}$ is termed electrochromic modular architecture (MoE_A) (Figure 6.5).

Three types of electrochromic modules (M^1 , M^2 , M^3) are prepared using PANI layers of different thicknesses (Figure 6.4a). PANI shows the light green, green, and blue colors at reduced (-2.5 V), neutral (0 V), and oxidized states (2.5 V) respectively. Using the principle of Lambert's law, variation in thickness of PANI layer gives the different shades of green and bluish green color [145]. Here, PANI of three different thicknesses is used to give the shades of green and bluish-green colors (Figure 6.6a - 6.6c). Since the focus of this study is on the forest vegetation, brown color also plays an important role along with green. Therefore, combined polyaniline (PANI) and poly (3-hexyl thiophene) (P3HT) layers are used in the M^4 electrochromic module (Figure 6.4b) to give brown and green colors at -2.5 V and

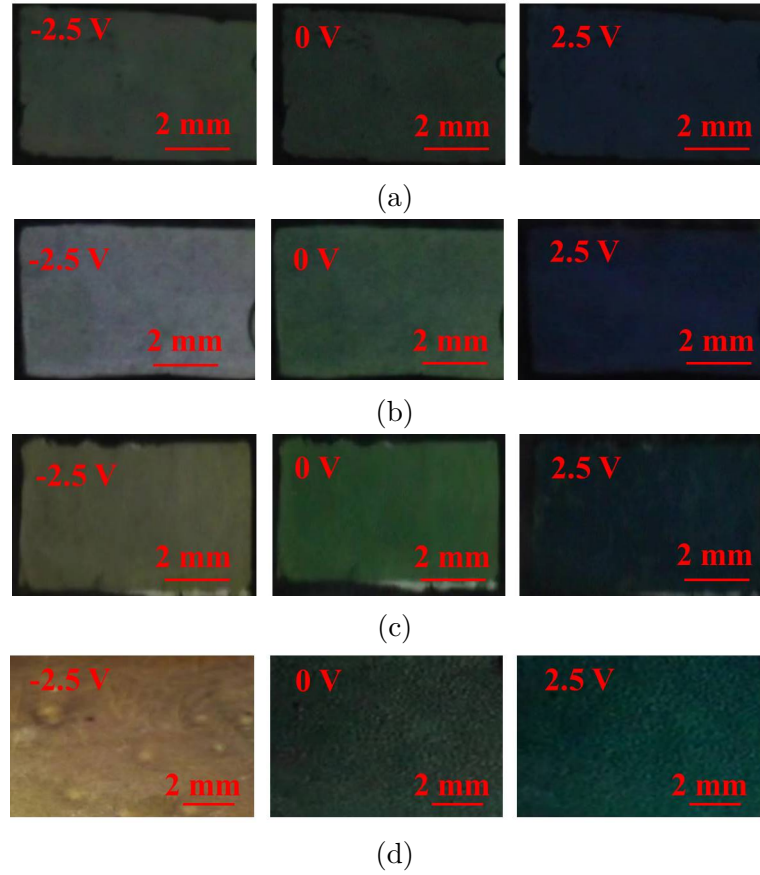


Figure 6.6: Digital images of (a) M^1 , (b) M^2 , (c) M^3 and (d) M^4 at different voltages.

0 V respectively (Figure 6.6d). Captured digital images of M^1 , M^2 , M^3 and M^4 at different voltages are shown in Figure 6.6a - 6.6d. Digital images show the brown and green color shades.

MoE_A is designed and developed using four types of electrochromic modules (M^1 , M^2 , M^3 , M^4). The detection ability of edges and corners is always more than the other parts of the system. Therefore, in its design, some points are taken into consideration.

1. No two consecutive modules are the same,
2. At corners, M^3 is used due to its lightest shade to reduce the detect-ability at corners,
3. Next darker shade, M^2 is used at edges in the alternative arrangement with M^1 ,
4. At the centre, darkest shade M^3 is used, and,
5. M^4 is used in the inner layer with the alternative arrangement of M^3 .

The arrangement of modules in MoE_A is shown in Figure 6.5. Each module is able to show 3 colors and due to the alternative arrangements of ECDs, the possible patterns are 3^{25} . All the modules are connected parallel to supply the power input independently to each module.

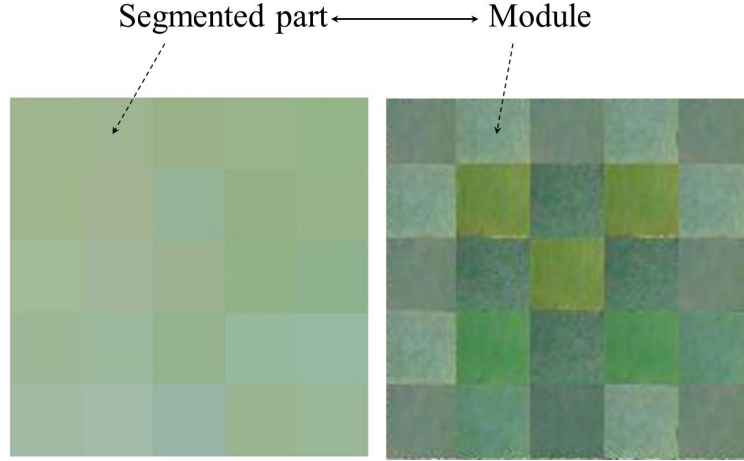


Figure 6.7: Comparing modular image and digital modular architecture.

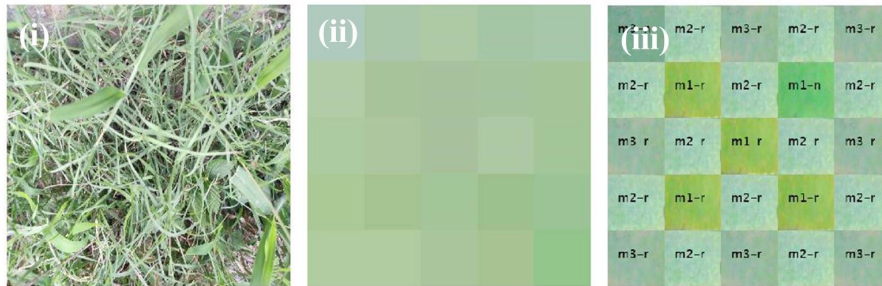


Figure 6.8: Comparing (i) original image, (ii) modular image and (iii) digital modular architecture (MoD_A). MoD_A representing the best suited pattern to particular surrounding by optimizing the digital images of modules ('n' = neutral state (0 V), 'o' = oxidized state (2.5 V) and 'r' = reduced state (-2.5 V)).

6.3.3 Active camouflage device

An active camouflage device (ACD) is developed to validate the proposed concept. It develops by integrating the pattern detection algorithm with pattern formation hardware. Electrochromic modules of MoE_A give a particular shade at a given voltage. To fulfill the requirement of altering the voltage to change the color shade of modules, it needs to perform the simulations to acquire the best-applied voltage for particular surroundings before the physical testing of ACD. Simulated results are used to transmit the signals to MoE_A to modulate the patterns accordingly.

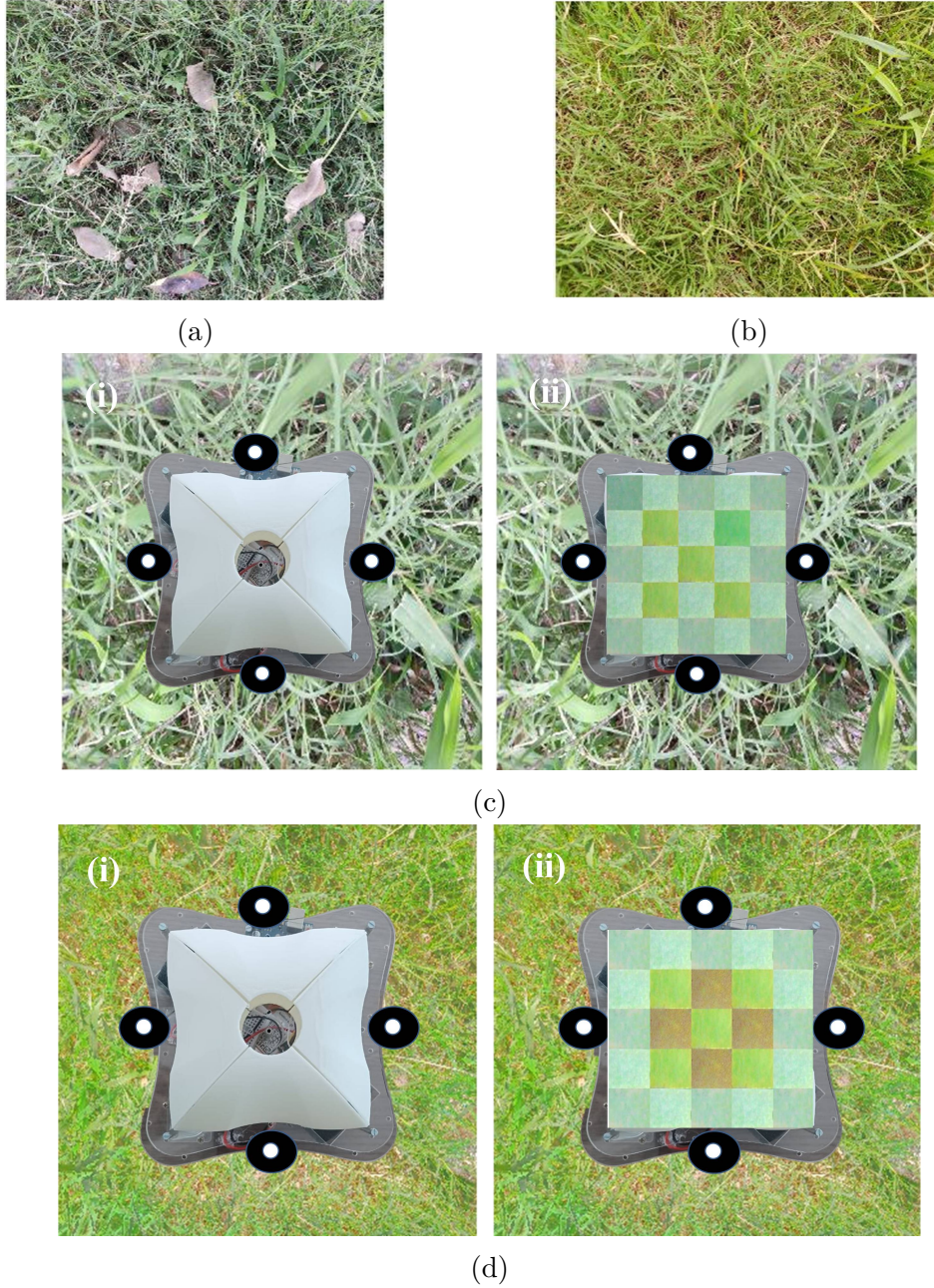


Figure 6.9: Images of green vegetation in the presence of (a) skylight showing bluish green color and (b) sunlight showing yellowish green color of grass. Turtle bot (i) with and (ii) without digital modular architecture ($MoDA$) under (c) skylight and (d) sunlight.

Simulations

Digital images (Figure 6.6) of all the modules at different excited states are used in the simulation. Digital modular architecture ($MoDA$) is prepared following the same design criteria of $MoEA$ for the arrangement of modules (Figure 6.5). Unlike $MoEA$, $MoDA$ has three digital images in place of modules and the digital images are compared with the segmented parts of MoI (see Figure 6.7) to get the desired

Table 6.1: Compare structural similarity index measures of mobile robot, modular image and digital modular architecture with reference to surrounding images.

Surroundings	Mobile robot	Modular image	Digital modular architecture
Skylight 1	0.06	0.17	0.13
Skylight 2	0.06	0.38	0.3
Skylight 3	0.07	0.6	0.44
Sunlight 1	0.02	0.86	0.43
Sunlight 2	0.04	0.76	0.39
Sunlight 3	0.04	0.63	0.3

potential for particular surroundings. A quantitative comparison is done using mean square error (MSE) given below,

$$MSE = \frac{\sum_1^p \sum_1^q (I_q^{(p)} - I_q'^{(p)})^2}{p \times q} \quad (6.2)$$

where I and I' are the pixel intensities of the segmented part and digital image respectively. Since the focus of this work is to get a similar color of surrounding, MSE is applied on the ‘hue’ (H) channel only. All three digital images are compared with the respective segmented part and the image with the least MSE is selected in the MoD_A (Figure 6.8). Electric potential is supplied on the basis of the selected image. ‘r’, ‘n’, and ‘o’ represents the reduced (-2.5 V), neutral (0 V), and oxidized state (2.5 V) respectively. A sample of captured green surroundings and its modular image is compared with the best possible patterns of the MoD_A (Figure 6.8).

Color is the property that critically depends on the material, viewer, and the light source. Along with the material, the viewer is also considered the same by using the same camera to capture all the images. Therefore, a comparative study is performed in the presence of two different light sources; skylight and sunlight as shown in Figure 6.9a and 6.9b. There is a difference in the color of grass under different light sources. The appearance of grass is bluish-green and yellowish-green in the presence of skylight and sunlight (Figure 6.9). Further, a mobile turtle bot is fabricated and placed on the surroundings in the presence of skylight and sunlight (Figure 6.9c(i), 6.9d(i)). It is found easily detectable with the visual appearance (Figure 6.9c(i), 6.9d(i)). On placing the optimized MoD_A on the turtle bot, its detect-ability reduces under both the light sources (Figure 6.9c(ii), 6.9d(ii)). It validates the feasibility of the proposed concept to achieve optical active camouflaging. Further, a quantitative comparative analysis is performed to understand the camouflaging effect of both light sources. Structural similarity index measure (SSIM) is used to compare the detectability in different light sources shown in Table. 6.1. It is a performance measurement parameter used to evaluate the similarity in two digital images using the three features (luminance, contrast, and structure). The equation

used to calculate the SSIM is given below.

$$SSIM(x, y) = \frac{(2\mu_x\mu_y + c_1)(2\sigma_{xy} + c_2)}{(\mu_x^2 + \mu_y^2 + c_1)(\sigma_x^2 + \sigma_y^2 + c_2)} \quad (6.3)$$

where, μ_x, μ_y are pixel sample mean of x and y respectively; σ_x^2, σ_y^2 are variance of x and y respectively; σ_{xy} is covariance of x and y ; $c_1 = k_1L, c_2 = k_2L; k_1 = 0.01, k_2 = 0.03; L = 2^{bits \text{ per pixel}} - 1$. For better clarity, images are captured at three different locations under both light sources to compare the camouflaging performance. Initially, the bare mobile robot is compared with the surrounding images captured in the presence of skylight and sunlight both followed by the *MoI* (Figure 6.9). Since *MoI* is the representation of the environment, it is taken as a reference for further comparison. At last *MoD_A* is compared with the surrounding. It is found that SSIM is ~ 0 on comparing the bare mobile robot with surroundings which implies no similarity and highest detectability. On comparing with the SSIM of *MoI*, *MoD_A* is found in the range of 74 - 80 % and 47 - 52 % for skylight and sunlight surroundings respectively. It shows a higher similarity under the skylight. The quantitative evaluation also validates the visual inspection that the proposed concept is best suited for surroundings under skylight rather than sunlight.

Physical testing

Further, a physical testing of ACD is performed as a proof of concept using simulated results. ACD is prepared by the system integration of *PDA* and *PFH*. Integration is performed in such a way that each segmented part of *MoI* is connected with the modules of *MoE_A* separately and electric potential is applied according to the output of simulated results. Any one of the voltages (-2.5 V, 0 V, and 2.5 V) is applied on each module independently. So two relays are connected with each module for switching the voltage applied. The circuit diagram is shown in Figure 6.10b. It makes the modules to work and replace independently to each other and fulfills the requirement of modularity. Moreover, the mapping of segmented parts of *MoI* and modules of *MoE_A* is done in such a way that their position remains the same as shown in Figure 6.10a. Simulating voltages of the optimized *MoD_A* for different surroundings are applied on the modules of *MoE_A*. Signals represent the 2.5 V for the oxidized state, -2.5 V for the reduced state, and 0 V for the neutral state. It is found that ACD is capable of sensing the surroundings and modulating the patterns accordingly for different surroundings as shown in Figure 6.10c.

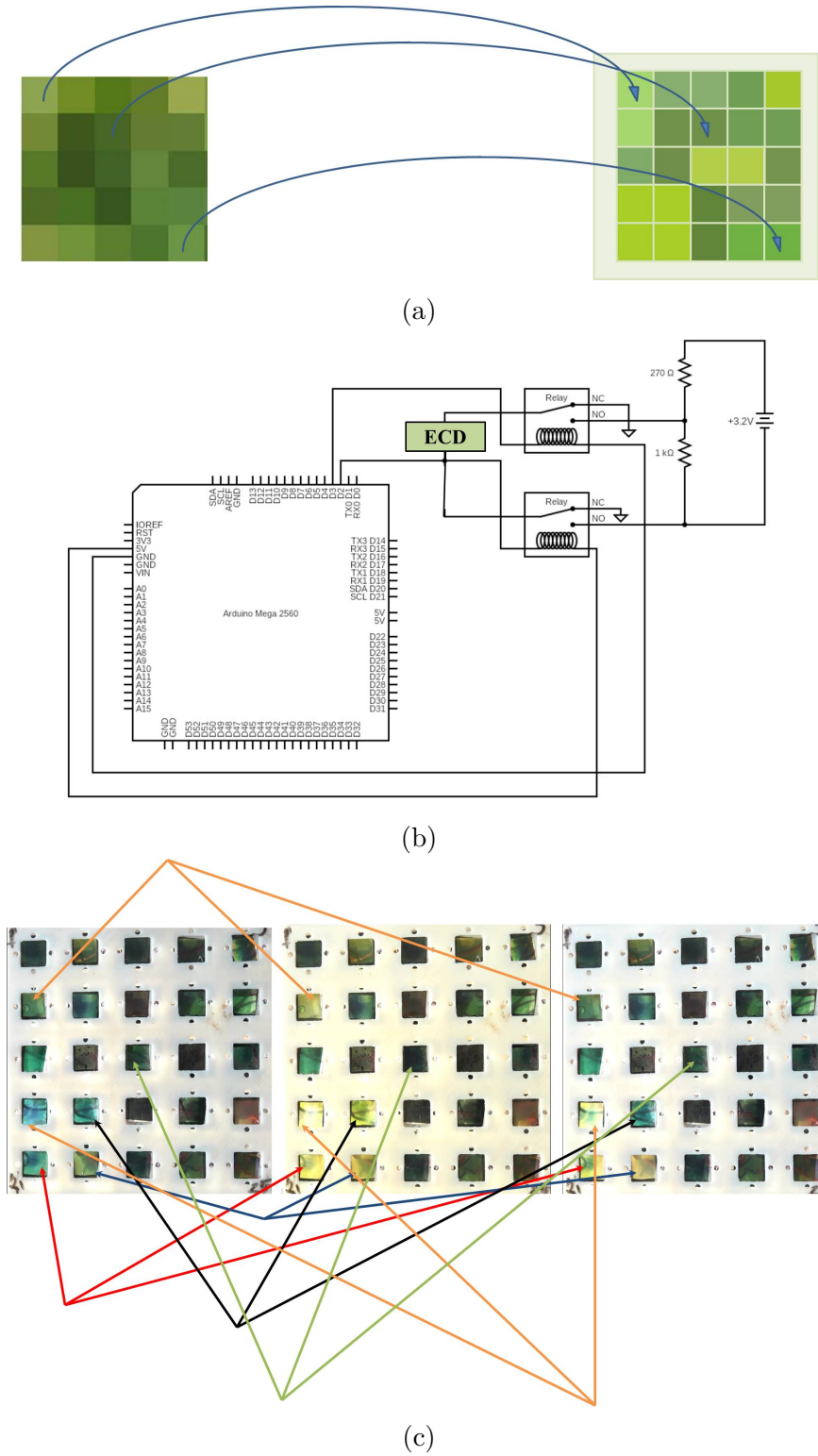


Figure 6.10: (a) Schematic showing mapping of segmented part of the modular image and module of electrochromic modular architecture, (b) circuit diagram and (c) active camouflage device changing patterns for different surroundings.

6.4 Conclusion

This work provides a design concept and demonstration to achieve active camouflaging in forest vegetation. An Active camouflage device is developed by using two units; pattern detection algorithm (PDA) and pattern formation hardware (PFH). PDA collects the information from surrounding and PFH changes the patterns accordingly. The algorithm collects the surrounding information and processes it to form a modular image (*MoI*) using a shadow removal algorithm, image segmentation, and color recognition. PFH achieves the pattern formation using electrochromic modular architecture; in which modules are electrochromic devices. PANI and PANI-P3HT-based electrochromic devices are used to achieve the green, bluish-green, and brown colors at different potentials. Three PANI-based and one P3HT-based modules are used in the electrochromic modular architecture. Then, simulation work is performed to optimize the applied potential required to actuate the modules of modular architecture for different surroundings. A comparative study is done in two types of surroundings; one is in the presence of skylight and another is with sunlight. The proposed concept is best suited for the surroundings under the skylight as confirmed by the visual inspection and quantitative analysis. SSIM is found $\sim 75\%$ and $\sim 50\%$ for skylight and sunlight surroundings respectively. Finally, modular image and electrochromic modular architecture are integrated physically, and testing is performed using simulated voltages. It is found that active camouflage device changes the pattern according to different forest surroundings. However, there are some modifications required in fabrication and control design to make it more suitable to work in the real environment. 3-D printed modular architecture has dead space between cavities to avoid short-circuiting of ECD. There is a requirement to remove this dead space by modifying the fabrication technique in such a way that all ECDs are connected parallel to the electric supply without touching each other. A controller with high computing power and large memory space is also required to make it automated and workable in a real environment. To this end, the proposed concept is capable of achieving active camouflaging and can be used for surveillance purposes in future.

Chapter 7

Conclusion

7.1 Summary of the work

A detailed study has been conducted to develop a modular electrochromic device for active camouflaging in forest vegetation. Inspired by bio species, two units are developed to sense the surroundings and to bring the physical change accordingly followed by their integration. Pattern detection algorithm (PDA) senses the surrounding information and makes it useful for modular electrochromic architecture (MEA) to bring the changes accordingly. Electrochromic devices (ECD) are used as modules to change the color on the application of voltage. Their service life is also improved by inducing the self-healing ability in the gel electrolyte layer. The salient features of this thesis are described below.

- It is observed that the addition of PMMA in gel electrolytes is a feasible strategy to induce self-healing and increase the service life of ECD. Different weight percent of PMMA influences the recovery in mechanical properties of GE.
- It is found that green shades in ECD are possible to modulate by varying the thickness of the PANI layer. Ion diffusion and redox voltages are also a function of PANI thickness.
- Combination of multiple ECP layers in ECD shows the colors in broader color space. Combined PANI and P3HT layers give the green and brown shades at different voltages when both are applied on the same electrode.
- Electrochromic modular architecture is designed and developed for green/brown surroundings using single and dual ECDs as modules.
- Optimized patterns are developed using a similarity index for best representing the surroundings.
- An Integrated active camouflage device is developed using ECD modules to test the desired patterns. It finds potential applications in technical textiles, surveillance, wildlife discoveries, etc.

7.2 Future scope

1. To analyze the self-healing ability of gel electrolyte by using additives in PMMA to increase its mechanical strength.
2. To study the effect of the molar concentration of lithium perchlorate on the self-healing performance of gel electrolyte.
3. To design and develop the complete self-healable electrochromic device.
4. To study and develop electrochromic devices for a large number of color shades.
5. To improve the cyclic stability of ECDs.
6. To apply the machine learning algorithms for getting the best arrangement of modules in modular electrochromic architecture.

References

- [1] Bodo D. Wilts, Primož Pirih, Kentaro Arikawa, and Doekele G. Stavenga. Shiny wing scales cause spec(tac)ular camouflage of the angled sunbeam butterfly, *Curetis acuta*. *Biol. J. Linn. Soc.*, 109(2):279–289, 2013. ISSN 00244066. doi: 10.1111/bij.12070.
- [2] L. M. Mäthger, M. F. Land, U. E. Siebeck, and N. J. Marshall. Rapid colour changes in multilayer reflecting stripes in the paradise whiptail, *Pentapodus paradiseus*. *J. Exp. Biol.*, 206(20):3607–3613, 2003. ISSN 00220949. doi: 10.1242/jeb.00599.
- [3] Hyunwoo Yuk, Shaoting Lin, Chu Ma, Mahdi Takaffoli, Nicolas X. Fang, and Xuanhe Zhao. Hydraulic hydrogel actuators and robots optically and sonically camouflaged in water. *Nat. Commun.*, 8:1–12, 2017. ISSN 20411723. doi: 10.1038/ncomms14230. URL <http://dx.doi.org/10.1038/ncomms14230>.
- [4] Pengcheng Li, Yuzhe Wang, Ujjaval Gupta, Jun Liu, Lei Zhang, Donghe Du, Choon Chiang Foo, Jianyong Ouyang, and Jian Zhu. Transparent Soft Robots for Effective Camouflage. *Adv. Funct. Mater.*, 29(1):1901908, 2019.
- [5] Zhipeng Meng, Baoting Huang, Suli Wu, Lu Li, and Shufen Zhang. Bio-inspired transparent structural color film and its application in biomimetic camouflage. *Nanoscale*, 11(28):13377–13384, 2019. ISSN 20403372. doi: 10.1039/c9nr04360h.
- [6] J. B. Messenger. Cephalopod chromatophores: Neurobiology and natural history. *Biol. Rev. Camb. Philos. Soc.*, 76(4):473–528, 2001. ISSN 14647931. doi: 10.1017/S1464793101005772.
- [7] R. T. Hanlon, C. C. Chiao, L. M. Mäthger, A. Barbosa, K. C. Buresch, and C. Chubb. Cephalopod dynamic camouflage: Bridging the continuum between background matching and disruptive coloration. *Philos. Trans. R. Soc. B Biol. Sci.*, 364(1516):429–437, 2009. ISSN 14712970. doi: 10.1098/rstb.2008.0270.
- [8] Aaron Fishman, Jonathan Rossiter, and Martin Homer. Hiding the squid: Patterns in artificial cephalopod skin. *J. R. Soc. Interface*, 12(108):20150281, 2015. ISSN 17425662. doi: 10.1098/rsif.2015.0281.

- [9] Jonathan Rossiter, Bryan Yap, and Andrew Conn. Biomimetic chromatophores for camouflage and soft active surfaces. *Bioinspiration and Biomimetics*, 7(3), 2012. ISSN 17483182. doi: 10.1088/1748-3182/7/3/036009.
- [10] Cunjiang Yu, Yuhang Li, Xun Zhang, Xian Huang, Viktor Malyarchuk, Shuodao Wang, Yan Shi, Li Gao, Yewang Su, Yihui Zhang, Hangxun Xu, Roger T. Hanlon, Yonggang Huang, and John A. Rogers. Adaptive optoelectronic camouflage systems with designs inspired by cephalopod skins. *Proc. Natl. Acad. Sci. U. S. A.*, 111(36):12998–13003, 2014. ISSN 10916490. doi: 10.1073/pnas.1410494111.
- [11] David D. Ordinario, Erica M. Leung, Long Phan, Rylan Kautz, Woo Kyung Lee, Mahan Naeim, Justin P. Kerr, Mercedeez J. Aquino, Paul E. Sheehan, and Alon A. Gorodetsky. Protochromic Devices from a Cephalopod Structural Protein. *Adv. Opt. Mater.*, 5(20):1–6, 2017. ISSN 21951071. doi: 10.1002/adom.201600751.
- [12] Jérémie Teyssier, Suzanne V. Saenko, Dirk Van Der Marel, and Michel C. Milinkovitch. Photonic crystals cause active colour change in chameleons. *Nat. Commun.*, 6:1–7, 2015. ISSN 20411723. doi: 10.1038/ncomms7368.
- [13] Yunlong Wang, Huanqing Cui, Qilong Zhao, and Xuemin Du. Chameleon-Inspired Structural-Color Actuators. *Matter*, 1(3):626–638, 2019. ISSN 25902385. doi: 10.1016/j.matt.2019.05.012. URL <https://doi.org/10.1016/j.matt.2019.05.012>.
- [14] Hyeonseok Kim, Joonhwa Choi, Kyun Kyu Kim, Phillip Won, Sukjoon Hong, and Seung Hwan Ko. Biomimetic chameleon soft robot with artificial crypsis and disruptive coloration skin. *Nat. Commun.*, 12(1):1–11, 2021. ISSN 20411723. doi: 10.1038/s41467-021-24916-w. URL <http://dx.doi.org/10.1038/s41467-021-24916-w>.
- [15] Stephen Daynes, Richard S. Trask, and Paul M. Weaver. Bio-inspired structural bistability employing elastomeric origami for morphing applications. *Smart Mater. Struct.*, 23(12):125011, 2014. ISSN 1361665X. doi: 10.1088/0964-1726/23/12/125011.
- [16] J. H. Pikul, S. Li, H. Bai, R. T. Hanlon, I. Cohen, and R. F. Shepherd. Stretchable surfaces with programmable 3D texture morphing for synthetic camouflaging skins. *Science (80-.)*, 358(6360):210–214, 2017. ISSN 10959203. doi: 10.1126/science.aan5627.

- [17] Guoping Wang, Xuechen Chen, Sheng Liu, Chingping Wong, and Sheng Chu. Mechanical Chameleon through Dynamic Real-Time Plasmonic Tuning. *ACS Nano*, 10(2):1788–1794, 2016. ISSN 1936086X. doi: 10.1021/acsnano.5b07472.
- [18] Stephen A. Morin, Robert F. Shepherd, Sen Wai Kwok, Adam A. Stokes, Alex Nemiroski, and George M. Whitesides. Camouflage and display for soft machines. *Science (80-.)*, 337(6096):828–832, 2012. ISSN 10959203. doi: 10.1126/science.1222149.
- [19] A. Rankin and S. McGarry. A flexible pressure sensitive colour changing device using plasmonic nanoparticles. *Nanotechnology*, 26(7):075502, 2015. ISSN 13616528. doi: 10.1088/0957-4484/26/7/075502.
- [20] Li Zhu, Jonas Kapraun, James Ferrara, and Connie J. Chang-Hasnain. Flexible photonic metastructures for tunable coloration. *Optica*, 2(3):255, 2015. ISSN 2334-2536. doi: 10.1364/optica.2.000255.
- [21] Qiming Wang, Gregory R. Gossweiler, Stephen L. Craig, and Xuanhe Zhao. Cephalopod-inspired design of electro-mechano-chemically responsive elastomers for on-demand fluorescent patterning. *Nat. Commun.*, 5(May): 1–9, 2014. ISSN 20411723. doi: 10.1038/ncomms5899. URL <http://dx.doi.org/10.1038/ncomms5899>.
- [22] C. Larson, B. Peele, S. Li, S. Robinson, M. Totaro, L. Beccai, B. Mazzolai, and R. Shepherd. Highly stretchable electroluminescent skin for optical signaling and tactile sensing. *Science (80-.)*, 351(6277):1071–1074, 2016. ISSN 10959203. doi: 10.1126/science.aac5082.
- [23] Ho Hsiu Chou, Amanda Nguyen, Alex Chortos, John W.F. To, Chien Lu, Jianguo Mei, Tadanori Kurosawa, Won Gyu Bae, Jeffrey B.H. Tok, and Zhenan Bao. A chameleon-inspired stretchable electronic skin with interactive colour changing controlled by tactile sensing. *Nat. Commun.*, 6:1–10, 2015. ISSN 20411723. doi: 10.1038/ncomms9011. URL <http://dx.doi.org/10.1038/ncomms9011>.
- [24] Issam Mjejri, Cara M. Doherty, Marta Rubio-Martinez, Glenna L. Drisko, and Aline Rougier. Double-Sided Electrochromic Device Based on Metal-Organic Frameworks. *ACS Appl. Mater. Interfaces*, 9(46):39930–39934, 2017. ISSN 19448252. doi: 10.1021/acsami.7b13647.
- [25] Kai Ling Zhou, Hao Wang, Sheng Jun Zhang, Jin Ting Jiu, Jing Bing Liu, Yong Zhe Zhang, and Hui Yan. Electrochromic modulation of near-infrared

- light by WO₃ films deposited on silver nanowire substrates. *J. Mater. Sci.*, 52(21):12783–12794, 2017. ISSN 15734803. doi: 10.1007/s10853-017-1391-0.
- [26] Claes Goran Granqvist. Electrochromic devices. *J. Eur. Ceram. Soc.*, 25(12 SPEC. ISS.):2907–2912, 2005. ISSN 09552219. doi: 10.1016/j.jeurceramsoc.2005.03.162.
- [27] Emerson Marcelo Giroto and Marco A. De Paoli. Flexible Electrochromic Windows: A Comparison Using Liquid and Solid Electrolytes. *J. Braz. Chem. Soc.*, 10(5):394–400, 1999. ISSN 01035053. doi: 10.1590/S0103-50531999000500010.
- [28] Fern M. Kelly, Ludivine Meunier, Cédric Cochrane, and Vladan Koncar. Polyaniline: Application as solid state electrochromic in a flexible textile display. *Displays*, 34(1):1–7, 2013. ISSN 01419382. doi: 10.1016/j.displa.2012.10.001. URL <http://dx.doi.org/10.1016/j.displa.2012.10.001>.
- [29] Yolanda Alesanco, Ana Viñuales, Javier Rodriguez, and Ramón Tena-Zaera. All-in-one gel-based electrochromic devices: Strengths and recent developments. *Materials (Basel)*., 11(3):1–27, 2018. ISSN 19961944. doi: 10.3390/ma11030414.
- [30] Xiaoxue Lin, Qingyi Lu, Caiyu Yang, Yan Wang, Wei Zhang, Dongxu Li, Yanyu Gao, Haijun Niu, and Wen Wang. Multifunctional donor–acceptor conjugated polymers containing isoindigo and benzothiadiazole moieties for electrochromic, photoelectric sensor, 2,4,6-trinitrophenol detection and resistance memory device. *J. Mater. Sci.*, 56(20):12001–12017, 2021. ISSN 15734803. doi: 10.1007/s10853-021-05952-9. URL <https://doi.org/10.1007/s10853-021-05952-9>.
- [31] Umran Koc, Gozde Yurdabak Karaca, Aysegul Uygun Oksuz, and Lutfi Oksuz. RF sputtered electrochromic wool textile in different liquid media. *J. Mater. Sci. Mater. Electron.*, 28(12):8725–8732, 2017. ISSN 1573482X. doi: 10.1007/s10854-017-6597-z.
- [32] Kerui Li, Qinghong Zhang, Hongzhi Wang, and Yaogang Li. Red, green, blue (RGB) electrochromic fibers for the new smart color change fabrics. *ACS Appl. Mater. Interfaces*, 6(15):13043–13050, 2014. ISSN 19448252. doi: 10.1021/am502929p.
- [33] Wei Ren Lian, Ying Chi Huang, Yi An Liao, Kun Li Wang, Lain Jong Li, Ching Yuan Su, Der Jang Liaw, Kueir Rarn Lee, and Juin Yih Lai. Flexible

- electrochromic devices based on optoelectronically active polynorbornene layer and ultratransparent graphene electrodes. *Macromolecules*, 44(24):9550–9555, 2011. ISSN 00249297. doi: 10.1021/ma201689e.
- [34] By Mao Li, Asit Patra, Yana Sheynin, and Michael Bendikov. Novel Highly Stable Organic Electrochromic Material with High Contrast Ratio , High Coloration Efficiency , and Low-Switching Voltage. *Adv. Mater.*, 21: 1707–1711, 2009. doi: 10.1002/adma.200802259.
- [35] Avni A Argun, Pierre-henri Aubert, Barry C Thompson, Irina Schwendeman, Carleton L Gaupp, Jungseek Hwang, Nicholas J Pinto, David B Tanner, Alan G Macdiarmid, and John R Reynolds. Multicolored Electrochromism in Polymers : Structures and Devices. *Chem. Mater.*, 16(23):4401–4412, 2004. doi: 10.1021/cm049669l.
- [36] Min Hong Kim, Hyung Wook Choi, Kyung Hwan Kim, and Kyung Hwan Kim. Thickness Dependence of WO_{3-x} Thin Films for Electrochromic Device Application Thickness Dependence of WO_{3-x} Thin Films for Electrochromic Device Application. *Mol. Cryst. Liq. Cryst.*, 598:54–61, 2014. doi: 10.1080/15421406.2014.933298.
- [37] H. N. Hersh, W. E. Kramer, and J. H. McGee. Mechanism of electrochromism in WO₃. *Appl. Phys. Lett.*, 27(12):646–648, 1975. ISSN 00036951. doi: 10.1063/1.88346.
- [38] Satoshi Hashimoto and Hideki Matsuoka. Mechanism of electrochromism for amorphous WO₃ thin films. *J. Appl. Phys.*, 69(2):933–937, 1991. ISSN 00218979. doi: 10.1063/1.347335.
- [39] Wei Feng Chen, Shu Yii Wu, and Yi Fang Ferng. The electrochromic properties of nickel oxide by chemical deposition and oxidization. *Mater. Lett.*, 60(6): 790–795, 2006. ISSN 0167577X. doi: 10.1016/j.matlet.2005.10.031.
- [40] K. K. Purushothaman and G. Muralidharan. Nanostructured NiO based all solid state electrochromic device. *J. Sol-Gel Sci. Technol.*, 46(2):190–194, 2008. ISSN 09280707. doi: 10.1007/s10971-007-1657-0.
- [41] Huan Shen Liu, Bo Cheng Pan, and Guey Sheng Liou. Highly transparent AgNW/PDMS stretchable electrodes for elastomeric electrochromic devices. *Nanoscale*, 9(7):2633–2639, 2017. ISSN 20403372. doi: 10.1039/c6nr09220a.
- [42] Anjali Chaudhary, Devesh K Pathak, Suryakant Mishra, Priyanka Yogi, and Pankaj R Sagdeo. Polythiophene -viologen bilayer for electro-trichromic device. *Sol. Energy Mater. Sol. Cells*, 188(August):249–254, 2018.

- [43] A. Medrano-Solís, M. E. Nicho, and F. Hernández-Guzmán. Study of dual electrochromic devices based on polyaniline and poly (3-hexylthiophene) thin films. *J. Mater. Sci. Mater. Electron.*, 28(3):2471–2480, 2017. ISSN 1573482X. doi: 10.1007/s10854-016-5820-7.
- [44] Heng Yi Lu, Chin Yen Chou, Jia Hao Wu, Jiang Jen Lin, and Guey Sheng Liou. Highly transparent and flexible polyimide-AgNW hybrid electrodes with excellent thermal stability for electrochromic applications and defogging devices. *J. Mater. Chem. C*, 3(15):3629–3635, 2015. ISSN 20507526. doi: 10.1039/c5tc00142k.
- [45] Wei Teng Neo, Qun Ye, Soo Jin Chua, and Jianwei Xu. Conjugated polymer-based electrochromics: Materials, device fabrication and application prospects. *J. Mater. Chem. C*, 4(31):7364–7376, 2016. ISSN 20507526. doi: 10.1039/c6tc01150k. URL <http://dx.doi.org/10.1039/c6tc01150k>.
- [46] Hongfeng Wang, Matthew Barrett, Brett Duane, Jian Gu, and Frederic Zenhausern. Materials and processing of polymer-based electrochromic devices. *Mater. Sci. Eng. B Solid-State Mater. Adv. Technol.*, 228(November 2017):167–174, 2018. ISSN 09215107. doi: 10.1016/j.mseb.2017.11.016.
- [47] Thanakorn Jiemsakul, Kanpitcha Jiramitmongkon, Udom Asawapirom, and Chuleekorn Chotsuwan. Investigation of P3HT electrochromic polymer films prepared by ultrasonication of polymer solutions. *J. Mater. Sci.*, 52(14): 8485–8492, 2017. ISSN 1573-4803. doi: 10.1007/s10853-017-1109-3.
- [48] Jing Wang, Han Yan, and Yun Lu. The thiophene derivative with ferricyanide end group and its polymers: synthesis and electrochromic performance. *J. Mater. Sci.*, 50(21):6920–6925, 2015. ISSN 15734803. doi: 10.1007/s10853-015-9242-3.
- [49] Ching Mui Cho, Qun Ye, Wei Teng, Tingting Lin, and Jing Song. Red-to-black electrochromism of 4,9-dihydro-s-indaceno[1,2-b:5,6-b']dithiophene-embedded conjugated polymers. *J. Mater. Sci.*, 50:5856–5864, 2015. doi: 10.1007/s10853-015-9135-5.
- [50] D. R. Rosseinsky and P. M.S. Monk. Studies of tetra-(bipyridilium) salts as possible polyelectrochromic materials. *J. Appl. Electrochem.*, 24(12): 1213–1221, 1994. ISSN 0021891X. doi: 10.1007/BF00249884.
- [51] Cheng Hung Chang, Kun Li Wang, Jyh Chiang Jiang, Der Jang Liaw, Kueir Rarn Lee, Juin Yih Lai, and Kuan Hua Lai. Novel rapid

- switching and bleaching electrochromic polyimides containing triarylamine with 2-phenyl-2-isopropyl groups. *Polymer (Guildf)*., 51(20):4493–4502, 2010. ISSN 00323861. doi: 10.1016/j.polymer.2010.07.023. URL <http://dx.doi.org/10.1016/j.polymer.2010.07.023>.
- [52] Masao Kaneko, Hideki Nakamura, and Takeshi Shimomura. Multicolour electrochromism of polyaniline film. *Die Makromol. Chemie, Rapid Commun.*, 8(4):179–180, 1987. ISSN 0173-2803. doi: 10.1002/marc.1987.030080402.
- [53] Anjali Chaudhary, Devesh K. Pathak, Manushree Tanwar, Priyanka Yogi, Pankaj R. Sagdeo, and Rajesh Kumar. Polythiophene-PCBM-Based All-Organic Electrochromic Device: Fast and Flexible. *ACS Appl. Electron. Mater.*, 1(1):58–63, 2019. ISSN 26376113. doi: 10.1021/acsaelm.8b00012.
- [54] J. Zhang, J. P. Tu, X. H. Xia, Y. Qiao, and Y. Lu. An all-solid-state electrochromic device based on NiO/WO₃ complementary structure and solid hybrid polyelectrolyte. *Sol. Energy Mater. Sol. Cells*, 93(10):1840–1845, 2009. ISSN 09270248. doi: 10.1016/j.solmat.2009.06.025. URL <http://dx.doi.org/10.1016/j.solmat.2009.06.025>.
- [55] Wanyu Chen, Caizhi Zhu, Le Guo, Meng Ying Yan, Lili Wu, Bo Zhu, Chenjie Qi, Siyuan Liu, Heng Zhang, and Yong Peng. A novel ionically crosslinked gel polymer electrolyte as an ion transport layer for high-performance electrochromic devices. *J. Mater. Chem. C*, 7(13):3744–3750, 2019. ISSN 20507526. doi: 10.1039/C9TC00621D.
- [56] Elif Ceren Gok, Murat Onur Yildirim, Esin Eren, and Aysegul Uygur Oksuz. Comparison of machine learning models on performance of single- And dual-type electrochromic devices. *ACS Omega*, 5(36):23257–23267, 2020. ISSN 24701343. doi: 10.1021/acsomega.0c03048.
- [57] Tzung Hua Lin and Kuo Chuan Ho. A complementary electrochromic device based on polyaniline and poly(3,4-ethylenedioxythiophene). *Sol. Energy Mater. Sol. Cells*, 90(4):506–520, 2006. ISSN 09270248. doi: 10.1016/j.solmat.2005.02.017.
- [58] Chung Wen Kuo, Bor Kuan Chen, Wen Bin Li, Lan Yu Tseng, Tzi Yi Wu, Ching Guey Tseng, Ho Rei Chen, and Yu Chang Huang. Effects of supporting electrolytes on spectroelectrochemical and electrochromic properties of polyaniline-poly(styrene sulfonic acid) and poly(ethylenedioxythiophene)-poly(styrene sulfonic acid)-based

- electrochromic device. *J. Chinese Chem. Soc.*, 61(5):563–570, 2014. ISSN 21926549. doi: 10.1002/jccs.201300479.
- [59] Sihang Zhang, Sheng Chen, Feng Yang, Fei Hu, Bin Yan, Yingchun Gu, Hao Jiang, Ya Cao, and Ming Xiang. High-performance electrochromic device based on novel polyaniline nanofibers wrapped antimony-doped tin oxide/TiO₂ nanorods. *Org. Electron.*, 65(November 2018):341–348, 2019. ISSN 15661199. doi: 10.1016/j.orgel.2018.11.036.
- [60] U. León-Silva, M. E. Nicho, Hailin Hu, and Rodolfo Cruz-Silva. Effect of modified ITO substrate on electrochromic properties of polyaniline films. *Sol. Energy Mater. Sol. Cells*, 91(15-16):1444–1448, 2007. ISSN 09270248. doi: 10.1016/j.solmat.2007.03.023.
- [61] A. Medrano-Solís, M. E. Nicho, and F. Hernández-Guzmán. Study of dual electrochromic devices based on polyaniline and poly (3-hexylthiophene) thin films. *J. Mater. Sci. Mater. Electron.*, 28(3):2471–2480, 2017. ISSN 1573482X. doi: 10.1007/s10854-016-5820-7.
- [62] Eliana A. R. Duek, Marco A. De Paoli, and Marina Mastragostino. An Electrochromic Device Based on Polyaniline and Prussian Blue. *Adv. Mater.*, 4(4):287–291, 1992.
- [63] Sven Macher, Marco Schott, Martin Dontigny, Abdelbast Guerfi, Karim Zaghib, Uwe Posset, and Peer Löbmann. Large-Area Electrochromic Devices on Flexible Polymer Substrates with High Optical Contrast and Enhanced Cycling Stability. *Adv. Mater. Technol.*, 6(2):1–9, 2021. ISSN 2365709X. doi: 10.1002/admt.202000836.
- [64] Elif Sahin, Pinar Camurlu, and Levent Toppare. Dual-type electrochromic devices based on both n- and p-dopable poly(dithieno[3,4-b,3',4'-e]-[1,4]-dithiine). *Synth. Met.*, 156(16-17):1073–1077, 2006. ISSN 03796779. doi: 10.1016/j.synthmet.2006.06.020.
- [65] Huige Wei, Xingru Yan, Shijie Wu, Zhiping Luo, Suying Wei, and Zhanhu Guo. Electropolymerized polyaniline stabilized tungsten oxide nanocomposite films: Electrochromic behavior and electrochemical energy storage. *J. Phys. Chem. C*, 116(47):25052–25064, 2012. ISSN 19327447. doi: 10.1021/jp3090777.
- [66] Tae Ho Kim, Hyeong Jin Jeon, Jae Wook Lee, and Yoon Chae Nah. Enhanced electrochromic properties of hybrid P3HT/WO₃ composites with multiple colorations. *Electrochem. commun.*, 57:65–69, 2015. ISSN 13882481.

- doi: 10.1016/j.elecom.2015.05.008. URL <http://dx.doi.org/10.1016/j.elecom.2015.05.008>.
- [67] Ohyun Kwon and Michael L. McKee. Calculations of Band Gaps in Polyaniline from Theoretical Studies of Oligomers. *J. Phys. Chem. B*, 104(8):1686–1694, 2000. ISSN 15206106. doi: 10.1021/jp9910946.
- [68] Shanxin Xiong, R U Wang, Shuaishuai Li, Bohua Wu, J I A Chu, Xiaoqin Wang, Runlan Zhang, and Ming Gong. Electrochromic Behaviors of Water-Soluble Polyaniline with Covalently Bonded Acetyl Ferrocene. *J. Electron. Mater.*, 47(7):3974–3982, 2018. doi: 10.1007/s11664-018-6281-y.
- [69] Subhendu Bhandari. *Polyaniline: Structure and Properties Relationship*. Elsevier Inc., 2018. ISBN 9780128095515. doi: 10.1016/b978-0-12-809551-5.00002-3. URL <http://dx.doi.org/10.1016/B978-0-12-809551-5.00002-3>.
- [70] D K Bandgar, G D Khuspe, R C Pawar, C S Lee, and V B Patil. Facile and novel route for preparation of nanostructured polyaniline (PANi) thin films. *Appl. Nanosci.*, 4:27–36, 2014. doi: 10.1007/s13204-012-0175-8.
- [71] Sihang Zhang, Sheng Chen, Feng Yang, Fei Hu, Bin Yan, Yingchun Gu, Hao Jiang, Ya Cao, and Ming Xiang. High-performance electrochromic device based on novel polyaniline nanofibers wrapped antimony-doped tin oxide/TiO₂ nanorods. *Org. Electron.*, 65(October 2018):341–348, 2019. ISSN 15661199. doi: 10.1016/j.orgel.2018.11.036. URL <https://doi.org/10.1016/j.orgel.2018.11.036>.
- [72] Yongxiang Li. Novel photoelectrochromic cells containing a polyaniline layer and a dye-sensitized nanocrystalline TiO₂ photovoltaic cell. *Synth. Met.*, 94: 273–277, 1998.
- [73] Sung Jong Yoo, Joon Hyuk Cho, Ju Wan Lim, Sun Ha Park, Jyongsik Jang, and Yung Eun Sung. High contrast ratio and fast switching polymeric electrochromic films based on water-dispersible polyaniline-poly(4-styrenesulfonate) nanoparticles. *Electrochem. commun.*, 12(1):164–167, 2010. ISSN 13882481. doi: 10.1016/j.elecom.2009.11.014. URL <http://dx.doi.org/10.1016/j.elecom.2009.11.014>.
- [74] A. Bessière, C. Duhamel, J. C. Badot, V. Lucas, and M. C. Certiat. Study and optimization of a flexible electrochromic device based on polyaniline. *Electrochim. Acta*, 49(12):2051–2055, 2004. ISSN 00134686. doi: 10.1016/j.electacta.2003.12.034.

- [75] Liuxue Shen, Lianhuan Du, Shaozao Tan, Zhigang Zang, Chuanxi Zhao, and Wenjie Mai. Flexible electrochromic supercapacitor hybrid electrodes based on tungsten oxide films and silver nanowires. *Chem. Commun.*, 52(37):6296–6299, 2016. ISSN 1364548X. doi: 10.1039/c6cc01139j.
- [76] Liangbing Hu, George Gruner, Dan Li, Richard B. Kaner, and Jiri Cech. Patternable transparent carbon nanotube films for electrochromic devices. *J. Appl. Phys.*, 101(1), 2007. ISSN 00218979. doi: 10.1063/1.2402330.
- [77] Brian G Lewis and David C Paine. Applications and Processing of Transparent Conducting Oxides. *MRS Bull.*, 25(8):22–27, 2000. URL http://www.mrs.org.libproxy.mit.edu/s{_}mrs/sec{_}subscribe.asp?CID=2937{&}DID=173286{&}action=detail{&}5Cnhttp://www.mrs.org.libproxy.mit.edu/s{_}mrs/bin.asp?CID=2937{&}DID=94240{&}DOC=FILE.PDF.
- [78] J. E. A. M. van den Meerakker and W. R. ter Veen. Reductive Corrosion of ITO in Contact with Al in Alkaline Solutions. *J. Electrochem. Soc.*, 139(2): 385–390, 1992. ISSN 0013-4651. doi: 10.1149/1.2069228.
- [79] Anil Arya and A. L. Sharma. *Polymer electrolytes for lithium ion batteries: a critical study*, volume 23. Ionics, 2017. ISBN 1158101619. doi: 10.1007/s11581-016-1908-6.
- [80] Gamze Atak and Özlem Duyar Coşkun. Fabrication of an all solid-state electrochromic device using zirconium dioxide as an ion-conducting layer. *Thin Solid Films*, 664(August):70–78, 2018. ISSN 00406090. doi: 10.1016/j.tsf.2018.08.030.
- [81] Yuria Saito, Hiroshi Kataoka, and A. Manuel Stephan. Investigation of the conduction mechanisms of lithium gel polymer electrolytes based on electrical conductivity and diffusion coefficient using NMR. *Macromolecules*, 34(20): 6955–6958, 2001. ISSN 00249297. doi: 10.1021/ma0102823.
- [82] Isabella Nicotera, Luigi Coppola, Cesare Oliviero, Marco Castriota, and Enzo Cazzanelli. Investigation of ionic conduction and mechanical properties of PMMA-PVdF blend-based polymer electrolytes. *Solid State Ionics*, 177(5-6): 581–588, 2006. ISSN 01672738. doi: 10.1016/j.ssi.2005.12.028.
- [83] Yan Jie Wang and Dukjoon Kim. Crystallinity, morphology, mechanical properties and conductivity study of in situ formed PVdF/LiClO₄/TiO₂ nanocomposite polymer electrolytes. *Electrochim. Acta*, 52(9):3181–3189, 2007. ISSN 00134686. doi: 10.1016/j.electacta.2006.09.070.

- [84] P. Zhang, L. C. Yang, L. L. Li, M. L. Ding, Y. P. Wu, and R. Holze. Enhanced electrochemical and mechanical properties of P(VDF-HFP)-based composite polymer electrolytes with SiO₂ nanowires. *J. Memb. Sci.*, 379(1-2):80–85, 2011. ISSN 03767388. doi: 10.1016/j.memsci.2011.05.043.
- [85] Yanhuai Ding, Ping Zhang, Zhilin Long, Yong Jiang, Fu Xu, and Wei Di. The ionic conductivity and mechanical property of electrospun P(VdF-HFP)/PMMA membranes for lithium ion batteries. *J. Memb. Sci.*, 329(1-2):56–59, 2009. ISSN 03767388. doi: 10.1016/j.memsci.2008.12.024.
- [86] A. Manuel Stephan, R. Thirunakaran, N. G. Renganathan, V. Sundaram, S. Pitchumani, N. Muniyandi, R. Gangadharan, and P. Ramamoorthy. A study on polymer blend electrolyte based on PVC/PMMA with lithium salt. *J. Power Sources*, 81-82:752–758, 1999. ISSN 03787753. doi: 10.1016/s0378-7753(99)00148-2.
- [87] S. Ramesh, Tan Winie, and A. K. Arof. Investigation of mechanical properties of polyvinyl chloride-polyethylene oxide (PVC-PEO) based polymer electrolytes for lithium polymer cells. *Eur. Polym. J.*, 43(5):1963–1968, 2007. ISSN 00143057. doi: 10.1016/j.eurpolymj.2007.02.006.
- [88] seong hun Kim, jong kuk Choi, and young chan Bae. Mechanical properties and ionic conductivity of gel polymer electrolyte based on poly(vinylidene-fluoride-co-hexafluoropropylene). *J. Appl. Polym. Sci.*, 81(4): 948–956, 2001. ISSN 00218995. doi: 10.1002/app.1516.
- [89] Xu Peng, Huili Liu, Qin Yin, Junchi Wu, Pengzuo Chen, Guangzhao Zhang, Guangming Liu, Changzheng Wu, and Yi Xie. A zwitterionic gel electrolyte for efficient solid-state supercapacitors. *Nat. Commun.*, 7(May):1–8, 2016. ISSN 20411723. doi: 10.1038/ncomms11782. URL <http://dx.doi.org/10.1038/ncomms11782>.
- [90] Yazhou Chen, Guodong Xu, Xupo Liu, Qiyun Pan, Yunfeng Zhang, Danli Zeng, Yubao Sun, Hanzhong Ke, and Hansong Cheng. A gel single ion conducting polymer electrolyte enables durable and safe lithium ion batteries via graft polymerization. *RSC Adv.*, 8(70):39967–39975, 2018. ISSN 20462069. doi: 10.1039/C8RA07557C.
- [91] Hsien Wei Chen, Tzu Pin Lin, and Feng Chih Chang. Ionic conductivity enhancement of the plasticized PMMA/LiClO₄ polymer nanocomposite electrolyte containing clay. *Polymer (Guildf)*, 43(19):5281–5288, 2002. ISSN 00323861. doi: 10.1016/S0032-3861(02)00339-7.

- [92] Ava Hosseinioun and Elie Paillard. In situ crosslinked PMMA gel electrolyte from a low viscosity precursor solution for cost-effective, long lasting and sustainable lithium-ion batteries. *J. Memb. Sci.*, 594(September 2019): 117456, 2020. ISSN 18733123. doi: 10.1016/j.memsci.2019.117456. URL <https://doi.org/10.1016/j.memsci.2019.117456>.
- [93] Khushbu Gohel, D. K. Kanchan, Hiren K Machhi, Saurabh S Soni, and C Maheshwaran. Gel polymer electrolyte based on PVDF- HFP : PMMA incorporated with propylene carbonate (PC) and diethyl carbonate (DEC) plasticizers : electrical , morphology , structural and electrochemical properties Gel polymer electrolyte based on PVDF-HFP : PMM. *Mater. Res. express*, 7: 025301, 2020.
- [94] O. Bohnke, G. Frand, M. Rezrazi, C. Rousselot, and C. Truche. Fast ion transport in new lithium electrolytes gelled with PMMA. 2. Influence of lithium salt concentration. *Solid State Ionics*, 66(1-2):105–112, 1993. ISSN 01672738. doi: 10.1016/0167-2738(93)90033-Y.
- [95] Chi S. Kim and Seung M. Oh. Spectroscopic and electrochemical studies of PMMA-based gel polymer electrolytes modified with interpenetrating networks. *J. Power Sources*, 109(1):98–104, 2002. ISSN 03787753. doi: 10.1016/S0378-7753(02)00055-1.
- [96] Chen Zhao, Caiyun Wang, Zhilian Yue, Kewei Shu, and Gordon G. Wallace. Intrinsically stretchable supercapacitors composed of polypyrrole electrodes and highly stretchable gel electrolyte. *ACS Appl. Mater. Interfaces*, 5(18): 9008–9014, 2013. ISSN 19448244. doi: 10.1021/am402130j.
- [97] Haiyang Liao, Wenzhao Zhong, Ting Li, Jiuling Han, Xiao Sun, Xili Tong, and Yongqi Zhang. A review of self-healing electrolyte and their applications in flexible/stretchable energy storage devices. *Electrochim. Acta*, 404:139730, 2022. ISSN 00134686. doi: 10.1016/j.electacta.2021.139730. URL <https://doi.org/10.1016/j.electacta.2021.139730>.
- [98] Guoqiang Li, Lingxiao Gao, Lidong Li, and Lin Guo. An electrochromic and self-healing multi-functional supercapacitor based on PANI/nw-WO_{2.7}/Au NPs electrode and hydrogel electrolyte. *J. Alloys Compd.*, 786:40–49, 2019. ISSN 09258388. doi: 10.1016/j.jallcom.2018.12.142.
- [99] Qijun Chen, Yuchen Shi, Kai Sheng, Jianming Zheng, and Chunye Xu. Dynamically Cross-Linked Hydrogel Electrolyte with Remarkable Stretchability and Self-Healing Capability for Flexible Electrochromic Devices.

- ACS Appl. Mater. Interfaces*, 13(47):56544–56553, 2021. ISSN 19448252. doi: 10.1021/acsami.1c15432.
- [100] Yi Wang, Rongzong Zheng, Junsheng Luo, Haseeb Ashraf Malik, Zhongquan Wan, Chunyang Jia, Xiaolong Weng, Jianliang Xie, Longjiang Deng, and Xiaojun Yao. Self-healing dynamically cross linked versatile polymer electrolyte: A novel approach towards high performance, flexible electrochromic devices. *Electrochim. Acta*, 320:134489, 2019. ISSN 00134686. doi: 10.1016/j.electacta.2019.06.182. URL <https://doi.org/10.1016/j.electacta.2019.06.182>.
- [101] Xinhua Liu, Dongbei Wu, Huanlei Wang, and Qigang Wang. Self-recovering tough gel electrolyte with adjustable supercapacitor performance. *Adv. Mater.*, 26(25):4370–4375, 2014. ISSN 15214095. doi: 10.1002/adma.201400240.
- [102] Maryam Hina, Shahid Bashir, Kashif Kamran, Javed Iqbal, S. Ramesh, and K. Ramesh. Fabrication of aqueous solid-state symmetric supercapacitors based on self-healable poly (acrylamide)/PEDOT:PSS composite hydrogel electrolytes. *Mater. Chem. Phys.*, 273(July), 2021. ISSN 02540584. doi: 10.1016/j.matchemphys.2021.125125.
- [103] Antoinette B. South and L. Andrew Lyon. Autonomic self-healing of hydrogel thin films. *Angew. Chemie - Int. Ed.*, 49(4):767–771, 2010. ISSN 14337851. doi: 10.1002/anie.200906040.
- [104] Zengjiang Wei, Jie He, Tony Liang, Hyuntaek Oh, Jasmin Athas, Zhen Tong, Chaoyang Wang, and Zhihong Nie. Autonomous self-healing of poly(acrylic acid) hydrogels induced by the migration of ferric ions. *Polym. Chem.*, 4(17): 4601–4605, 2013. ISSN 17599962. doi: 10.1039/c3py00692a.
- [105] Anthony J. D’Angelo and Matthew J. Panzer. Design of Stretchable and Self-Healing Gel Electrolytes via Fully Zwitterionic Polymer Networks in Solvate Ionic Liquids for Li-Based Batteries. *Chem. Mater.*, 31(8):2913–2922, 2019. ISSN 15205002. doi: 10.1021/acs.chemmater.9b00172.
- [106] Huihui Gan, Yong Zhang, Shaoqiao Li, Liping Yu, Jirong Wang, and Zhigang Xue. Self-Healing Single-Ion Conducting Polymer Electrolyte Formed via Supramolecular Networks for Lithium Metal Batteries. *ACS Appl. Energy Mater.*, 4(1):482–491, 2021. ISSN 25740962. doi: 10.1021/acsaem.0c02384.
- [107] Authors Pauline Jaumaux, Qi Liu, Dong Zhou, Xiaofu Xu, Yizhou Wang, Feiyu Kang, and Baohua Li. Deep Eutectic Solvent-Based Self-Healing

- Polymer Electrolyte for Safe and Long-Life Lithium Metal Batteries. *Angew. Chemie Int. Ed.*, 59(23):9134–42, 2020.
- [108] A. Sydney Gladman, Asha Dee N. Celestine, Nancy R. Sottos, and Scott R. White. Autonomic healing of acrylic bone cement. *Adv. Healthc. Mater.*, 4(2):202–207, 2015. ISSN 21922659. doi: 10.1002/adhm.201400084.
- [109] Asha Dee N. Celestine, Nancy R. Sottos, and Scott R. White. Autonomic healing of PMMA via microencapsulated solvent. *Polymer (Guildf.)*, 69: 241–248, 2015.
- [110] C B Lin, Sanboh Lee, and K S Liu. Methanol-Induced Crack Healing in Poly(Methyl Methacrylate). *Polym. Eng. Sci.*, 30(21):1399–1406, 1990.
- [111] Fatemeh Ahangaran, Mehran Hayaty, Amir H. Navarchian, and Francesco Picchioni. Micromechanical assessment of PMMA microcapsules containing epoxy and mercaptan as self-healing agents. *Polym. Test.*, 64(August): 330–336, 2017. ISSN 01429418. doi: 10.1016/j.polymertesting.2017.10.014. URL <http://dx.doi.org/10.1016/j.polymertesting.2017.10.014>.
- [112] Fatemeh Ahangaran, Amir H. Navarchian, Mehran Hayaty, and Karim Esmailpour. Effect of mixing mode and emulsifying agents on micro/nanoencapsulation of low viscosity self-healing agents in polymethyl methacrylate shell. *Smart Mater. Struct.*, 25(9), 2016. ISSN 1361665X. doi: 10.1088/0964-1726/25/9/095035.
- [113] P. A. Bolimowski and A. Boczkowska. Autonomous self-healing based on epoxy resin–imidazole chemistry in carbon fiber-reinforced polymer composites. *J. Appl. Polym. Sci.*, 136(2):1–9, 2019. ISSN 10974628. doi: 10.1002/app.46938.
- [114] Li Qi, Siddaramaiah, Nam hoon Kim, David Hui, and Joong Hee Lee. Effects of dual component microcapsules of resin and curing agent on the self-healing efficiency of epoxy. *Compos. Part B*, 55:79–85, 2013.
- [115] Amir H. Navarchian, Nasrin Najafipour, and Fatemeh Ahangaran. Surface-modified poly(methyl methacrylate) microcapsules containing linseed oil for application in self-healing epoxy-based coatings. *Prog. Org. Coatings*, 132:288–297, 2019.
- [116] Sydney D. Menikheim and Erin B. Lavik. Self-healing biomaterials: The next generation is nano. *Wiley Interdiscip. Rev. Nanomedicine Nanobiotechnology*, 12(6):1–15, 2020. ISSN 19390041. doi: 10.1002/wnan.1641.

- [117] Andressa Trentin, Samarah V. Harb, Mayara C. Uvida, Sandra H. Pulcinelli, Celso V. Santilli, Kristof Marcoen, Sven Pletincx, Herman Terryn, Tom Hauffman, and Peter Hammer. Dual Role of Lithium on the Structure and Self-Healing Ability of PMMA-Silica Coatings on AA7075 Alloy. *ACS Appl. Mater. Interfaces*, 11(43):40629–40641, 2019. ISSN 19448252. doi: 10.1021/acsami.9b13839.
- [118] Samarah V. Harb, Andressa Trentin, Thiago Augusto Carneiro de Souza, Marina Magnani, Sandra Helena Pulcinelli, Celso V. Santilli, and Peter Hammer. Effective corrosion protection by eco-friendly self-healing PMMA-cerium oxide coatings. *Chem. Eng. J.*, 383:123219, 2020.
- [119] Fatemeh Ahangaran and Amir H. Navarchian. Towards the development of self-healing and antibacterial dental nanocomposites via incorporation of novel acrylic microcapsules. *Dent. Mater.*, 38:858–873, 2022.
- [120] Yong Zhang, Shi qiang Xue, Xiao jun Jiang, Jing yang Mu, and Yang Yi. The Spatial Color Mixing Model of Digital Camouflage Pattern. *Def. Technol.*, 9(3):157–161, 2013. ISSN 22149147. doi: 10.1016/j.dt.2013.09.015. URL <http://dx.doi.org/10.1016/j.dt.2013.09.015>.
- [121] Qi Jia, Xitong Yang, Weidong Xu, Xuliang Lv, and Jianghua Hu. Design of Camouflage Pattern Based on Mathematical Morphology. *Adv. Intell. Syst. Res.*, 141:166–170, 2017. doi: 10.2991/ammsa-17.2017.35.
- [122] Hui Du, Xiaogang Jin, and Xiaoyang Mao. Digital camouflage images using two-scale decomposition. *Eurographics Symp. Geom. Process.*, 31(7): 2203–2212, 2012. ISSN 17278384. doi: 10.1111/j.1467-8659.2012.03213.x.
- [123] Xin Yang, Wei Dong Xu, Qi Jia, and Ling Li. Research on Digital Camouflage Pattern Generation Algorithm Based on Adversarial Autoencoder Network. *Int. J. Pattern Recognit. Artif. Intell.*, 34(6):1–15, 2020. ISSN 02180014. doi: 10.1142/S0218001420500172.
- [124] Qi Jia, Wei Dong Xu, Jiang Hua Hu, Jun Liu, Xin Yang, and Li Yan Zhu. Design and evaluation of digital camouflage pattern by spot combination. *Multimed. Tools Appl.*, 79:22047–22064, 2020.
- [125] Hengfu Yang and Jianping Yin. A digital camouflage generation algorithm using color similarity. *Int. J. Multimed. Ubiquitous Eng.*, 10(6):159–164, 2015. ISSN 19750080. doi: 10.14257/ijmue.2015.10.6.16.

- [126] Peng Bian, Yi Jin, and Nai Ren Zhang. Fuzzy c-means clustering based digital camouflage pattern design and its evaluation. *Int. Conf. Signal Process. Proceedings, ICSP*, pages 1017–1020, 2010. doi: 10.1109/ICOSP.2010.5655856.
- [127] Feng Xue, Shan Xu, Yue Tong Luo, and Wei Jia. Design of digital camouflage by recursive overlapping of pattern templates. *Neurocomputing*, 172:262–270, 2016. ISSN 18728286. doi: 10.1016/j.neucom.2014.12.108. URL <http://dx.doi.org/10.1016/j.neucom.2014.12.108>.
- [128] Mojca Friškovec and Helena Gabrijelčič. Development of a procedure for camouflage pattern design. *Fibres Text. East. Eur.*, 81(4):68–76, 2010. ISSN 23007354.
- [129] Elaheh Daneshvar and Mohammad Amani Tehran. Optimal camouflage colors determination using spectral reflectance of real-scene objects. *Color Res. Appl.*, 46(2):341–349, 2021. ISSN 15206378. doi: 10.1002/col.22587.
- [130] Qi Jia, Hao Xue, Suhong Wang, and Chenghao Ma. Design and Camouflage Effect of Facial Camouflage Pattern. *Proc. 2020 IEEE Int. Conf. Adv. Electr. Eng. Comput. Appl. AEECA 2020*, pages 768–772, 2020. doi: 10.1109/AEECA49918.2020.9213453.
- [131] Yang Li, John Klingner, and Nikolaus Correll. Distributed camouflage for swarm robotics and smart materials. *Auton. Robots*, 42(8):1635–1650, 2018. ISSN 15737527. doi: 10.1007/s10514-018-9717-6. URL <https://doi.org/10.1007/s10514-018-9717-6>.
- [132] Lu Zhao, Liang Zhao, Yuxi Xu, Tengfei Qiu, Linjie Zhi, and Gaoquan Shi. Polyaniline electrochromic devices with transparent graphene electrodes. *Electrochim. Acta*, 55(2):491–497, 2009. ISSN 00134686. doi: 10.1016/j.electacta.2009.08.063.
- [133] Mi Ouyang, Xuming Hu, Xiongchao Shao, Lu Chen, Weijun Li, Ru Bai, Ling Zhang, Xiaojing Lv, Alexey Tameev, and Cheng Zhang. In situ preparation and determination of electrochemical and electrochromic properties of copper phthalocyanine-polyaniline nanocomposite films. *RSC Adv.*, 9(59):34382–34388, 2019. ISSN 20462069. doi: 10.1039/c9ra06540g. URL <http://dx.doi.org/10.1039/C9RA06540G>.
- [134] Chengcheng Wang, Xiaojun Jiang, Peng Cui, Mingfei Sheng, Xiaodan Gong, Liping Zhang, and Shaohai Fu. Multicolor and Multistage Response

- Electrochromic Color-Memory Wearable Smart Textile and Flexible Display. *ACS Appl. Mater. Interfaces*, 2021. ISSN 19448252. doi: 10.1021/acsami.1c01333.
- [135] Yang Zhou, Jian Fang, Hongxia Wang, Hua Zhou, Guilong Yan, Yan Zhao, Liming Dai, and Tong Lin. Multicolor Electrochromic Fibers with Helix-Patterned Electrodes. *Adv. Electron. Mater.*, 4(5):1–8, 2018. ISSN 2199160X. doi: 10.1002/aelm.201800104.
- [136] Jinbo Kim, Maxime Rémond, Donghwan Kim, Hwandong Jang, and Eunkyong Kim. Electrochromic Conjugated Polymers for Multifunctional Smart Windows with Integrative Functionalities. *Adv. Mater. Technol.*, 5(6): 1–22, 2020. ISSN 2365709X. doi: 10.1002/admt.201900890.
- [137] Suchita Kandpal, Tanushree Ghosh, Chanchal Rani, Anjali Chaudhary, Jinwoo Park, Pooi See Lee, and Rajesh Kumar. Multifunctional Electrochromic Devices for Energy Applications. *ACS Energy Lett.*, pages 1870–1886, 2023. ISSN 23808195. doi: 10.1021/acsenenergylett.3c00159.
- [138] Yang Zhou, Yan Zhao, Jian Fang, and Tong Lin. Electrochromic/supercapacitive dual functional fibres. *RSC Adv.*, 6 (111):110164–110170, 2016. ISSN 20462069. doi: 10.1039/c6ra20729d.
- [139] Zhiyan Wang, Lin Shen, Shungui Deng, Ping Cui, and Xiayin Yao. 10 μm -Thick High-Strength Solid Polymer Electrolytes with Excellent Interface Compatibility for Flexible All-Solid-State Lithium-Metal Batteries. *Adv. Mater.*, 33(25):1–7, 2021. ISSN 15214095. doi: 10.1002/adma.202100353.
- [140] Xiaolei Zhao, Pan Xiang, Jinghua Wu, Ziqiang Liu, Lin Shen, Gaozhan Liu, Ziqi Tian, Liang Chen, and Xiayin Yao. Toluene Tolerated $\text{Li}_9.88\text{GeP}_{1.96}\text{Sb}_{0.04}\text{S}_{11.88}\text{Cl}_{0.12}$ Solid Electrolyte toward Ultrathin Membranes for All-Solid-State Lithium Batteries. *Nano Lett.*, 23:227–234, 2022.
- [141] Hong Chul Moon, Timothy P. Lodge, and C. Daniel Frisbie. Solution processable, electrochromic ion gels for sub-1 V, flexible displays on plastic. *Chem. Mater.*, 27(4):1420–1425, 2015. ISSN 15205002. doi: 10.1021/acs.chemmater.5b00026.
- [142] Dong Gyu Seo and Hong Chul Moon. Mechanically Robust, Highly Ionic Conductive Gels Based on Random Copolymers for Bending Durable Electrochemical Devices. *Adv. Funct. Mater.*, 28(14):1–10, 2018. ISSN 16163028. doi: 10.1002/adfm.201706948.

- [143] Yong Min Kim, Won Young Choi, Jin Han Kwon, Jae Kyeong Lee, and Hong Chul Moon. Functional Ion Gels: Versatile Electrolyte Platforms for Electrochemical Applications †. *Chem. Mater.*, 33(8):2683–2705, 2021. ISSN 15205002. doi: 10.1021/acs.chemmater.1c00330.
- [144] Fanglin Xu, Shungui Deng, Qingya Guo, Dong Zhou, and Xiayin Yao. Quasi-Ionic Liquid Enabling Single-Phase Poly(vinylidene fluoride)-Based Polymer Electrolytes for Solid-State LiNi_{0.6}Co_{0.2}Mn_{0.2}O₂||Li Batteries with Rigid-Flexible Coupling Interphase. *Small Methods*, 5(7):1–10, 2021. ISSN 23669608. doi: 10.1002/smtd.202100262.
- [145] Vishal Agrawal, Ekta Singla, and Prabhat K Agnihotri. Modulation of optical properties of electrochromic device. *J. Mater. Sci. Mater. Electron.*, 33: 21935–21954, 2022. ISSN 1573-482X. doi: 10.1007/s10854-022-08982-4. URL <https://doi.org/10.1007/s10854-022-08982-4>.
- [146] D. Battisti, G. A. Nazri, B. Klassen, and R. Aroca. Vibrational studies of lithium perchlorate in propylene carbonate solutions. *J. Phys. Chem.*, 97(22): 5826–5830, 1993. ISSN 00223654. doi: 10.1021/j100124a007.
- [147] H. P. Chen, J. W. Fergus, and B. Z. Jang. The Effect of Ethylene Carbonate and Salt Concentration on the Conductivity of Propylene Carbonate Lithium Perchlorate Electrolytes. *J. Electrochem. Soc.*, 147(2):399, 2000. ISSN 00134651. doi: 10.1149/1.1393209.
- [148] Zhiye Tang, Kazushi Fujimoto, and Susumu Okazaki. A comparison of the brittle PMMA with the ductile PC on the elasticity and yielding from a molecular dynamics perspective. *Polymer (Guildf)*, 226(April):123809, 2021.
- [149] R. P. Wool and K. M. O’Connor. A theory of crack healing in polymers. *J. Appl. Phys.*, 52(10):5953–5963, 1981. ISSN 00218979. doi: 10.1063/1.328526.
- [150] K. Jud, H. H. Kausch, and J. G. Williams. Fracture mechanics studies of crack healing and welding of polymers. *J. Mater. Sci.*, 16(1):204–210, 1981. ISSN 00222461. doi: 10.1007/BF00552073.
- [151] C. K. Liu, T. J. Yang, J. S. Shen, and Sanboh Lee. Some recent results on crack healing of poly(methyl methacrylate). *Eng. Fract. Mech.*, 75:4876–4885, 2008.
- [152] R.P. Wool and K. M. O’Connor. Time Dependence of Crack Healing. *J. Polym. Sci. Lett. Ed.*, 20(13):7–16, 1982.

- [153] Yong Min Kim, Jin Han Kwon, Seonho Kim, U. Hyeok Choi, and Hong Chul Moon. Ion-cluster-mediated ultrafast self-healable ionoconductors for reconfigurable electronics. *Nat. Commun.*, 13(1):1–10, 2022. ISSN 20411723. doi: 10.1038/s41467-022-31553-4.
- [154] Ragnar Seldén. Fracture energy measurements in polycarbonate and PMMA. *Polym. Test.*, 7(3):209–222, 1987. ISSN 01429418. doi: 10.1016/0142-9418(87)90032-8.
- [155] Jamal N. Dawoud. Interaction energies and structures of the $\text{Li} + \cdot (\text{CO})_n$ ($n = 1-3$) complexes. *J. Chem. Sci.*, 129(5):543–552, 2017. ISSN 09737103. doi: 10.1007/s12039-017-1275-5.
- [156] O. Bohnke, C. Rousselot, P. A. Gillet, and C. Truche. Gel Electrolyte for Solid-State Electrochromic Cell. *J. Electrochem. Soc.*, 139(7):1862–1865, 1992. ISSN 0013-4651. doi: 10.1149/1.2069512.
- [157] Zeinab Abdel Hamid, Mona Hasan Gomaa, Sayed S. Abdel Rehim, Maamoun Abdel Hamid, and Ahmed Ibrahim. Synthesis and characterization of nanostructured polyaniline thin films with superhydrophobic properties. *Coatings*, 9(11):1–18, 2019. ISSN 20796412. doi: 10.3390/coatings9110748.
- [158] B. C. Thompson, P. Schottland, G. Sonmez, and J. R. Reynolds. In situ colorimetric analysis of electrochromic polymer films and devices. *Chem. Mater.*, 12(6):1563–1571, 2000. ISSN 03796779. doi: 10.1016/S0379-6779(00)00863-8.
- [159] Noboru Ohta and Alan R. Robertson. *Colorimetry: Fundamentals and Applications*. John Wiley & Sons, 2006. ISBN 9780470094723.
- [160] Sun Young Hong and Su Moon Park. Electrochemistry of conductive polymers 36. pH dependence of polyaniline conductivities studied by current-sensing atomic force microscopy. *J. Phys. Chem. B*, 109(19):9305–9310, 2005. ISSN 15206106. doi: 10.1021/jp050173g.
- [161] Milica M. Gvozdenović, Branimir Z. Jugovic, Jasmina S. Stevanovic, and Branimir N Grgur. Electrochemical synthesis of electroconducting polymers. *Polymers (Basel)*, 68(6):673–684, 2014. ISSN 0350249X. doi: 10.2298/HEMIND131122008G.
- [162] Anja Korent, Kristina Žagar Soderžnik, Sašo Šturm, and Kristina Žužek Rožman. A Correlative Study of Polyaniline Electropolymerization and its

- Electrochromic Behavior. *J. Electrochem. Soc.*, 167(10):106504, 2020. ISSN 1945-7111. doi: 10.1149/1945-7111/ab9929.
- [163] Yen Wei, Guang Way Jang, Chi Cheung Chan, Kesyin F. Hsueh, Ramakrishnan Hariharan, Sandeep A. Patel, and Charles K. Whitecar. Polymerization of aniline and alkyl ring-substituted anilines in the presence of aromatic additives. *J. Phys. Chem.*, 94(19):7716–7721, 1990. ISSN 00223654. doi: 10.1021/j100382a073.
- [164] S Stafstrom, J. L. Bredas, A. J. Epstein, H.S. Woo, D.B. Tanner, W. S. Huang, and A. G. MacDiarmid. Polaron Lattice in Highly Conducting Polyaniline: Theoretical and Optical Studies. *Phys. Rev. Lett.*, 59(13):1464, 1987. ISSN 00319007. doi: 10.1103/PhysRevLett.84.5237.
- [165] R. A. Huggins. Simple method to determine electronic conductivity and ionic components of the conductors in mixed a review. *Ionics (Kiel)*., 8(3-4): 300–313, 2002. ISSN 18620760. doi: 10.1007/BF02376083.
- [166] W. H. Mulder and J. H. Sluyters. An explanation of depressed semi-circular arcs in impedance plots for irreversible electrode reactions. *Electrochim. Acta*, 33(3):303–310, 1988. ISSN 00134686. doi: 10.1016/0013-4686(88)85021-7.
- [167] M. M.E. Jacob, S. R.S. Prabakaran, and S. Radhakrishna. Effect of PEO addition on the electrolytic and thermal properties of PVDF-LiClO₄ polymer electrolytes. *Solid State Ionics*, 104(3-4):267–276, 1997. ISSN 01672738. doi: 10.1016/s0167-2738(97)00422-0.
- [168] W. S. Huang and A. G. MacDiarmid. Optical properties of polyaniline. *Polymer (Guildf)*., 34(9):1833–1845, 1993. ISSN 00323861. doi: 10.1016/0032-3861(93)90424-9.
- [169] Carleton L. Gaupp, Dean M. Welsh, R. David Rauh, and John R. Reynolds. Composite coloration efficiency measurements of electrochromic polymers based on 3,4-alkylenedioxythiophenes. *Chem. Mater.*, 14(9):3964–3970, 2002. ISSN 08974756. doi: 10.1021/cm020433w.
- [170] W Weppner and R A Huggins. Determination of the Kinetic Parameters of Mixed-Conducting Electrodes and Application to the System Li₃Sb. *J. Electrochem. Soc.*, 124(10):1569–1578, 1977. ISSN 0013-4651. doi: 10.1149/1.2133112.
- [171] Noor a Ibraheem, Mokhtar M Hasan, Rafiqul Z Khan, and Pramod K Mishra. Understanding Color Models : A Review. *ARPJ J. Sci. Technol.*, 2(3): 265–275, 2012.

- [172] W. Mokrzycki and M. Tatol. Color difference Delta E - A survey Colour difference E - A survey Faculty of Mathematics and Informatics. *Mach. Graph. Vis.*, 20(4):383–411, 2011. ISSN 0168-7433.
- [173] Hui Gong, Kailing Zhou, Qianqian Zhang, Jingbing Liu, Hao Wang, and Hui Yan. A self-patterning multicolor electrochromic device by horizontal redistribution of ions, 2020.
- [174] Marco Schott, Lukas Niklaus, Christine Müller, Begüm Bozkaya, and Guinevere A. Giffin. Flexible electrochromic devices prepared on ultra-thin ITO glass. *Mater. Adv.*, 2(14):4659–4666, 2021. ISSN 26335409. doi: 10.1039/d1ma00376c.
- [175] Tiago Moreira, César A.T. Laia, Mattia Zangoli, Mariana Antunes, Francesca Di Maria, Stefano De Monte, Fabiola Liscio, A. Jorge Parola, and Giovanna Barbarella. Semicrystalline Polythiophene-Based Nanoparticles Deposited from Water on Flexible PET/ITO Substrates as a Sustainable Approach toward Long-Lasting Solid-State Electrochromic Devices. *ACS Appl. Polym. Mater.*, 2(8):3301–3309, 2020. ISSN 26376105. doi: 10.1021/acsapm.0c00440.
- [176] Esin Eren, Ceyda Alver, Gozde Yurdabak Karaca, Emre Uygun, and Aysegul Uygun Oksuz. Enhanced electrochromic performance of WO₃ hybrids using polymer plasma hybridization process. *Synth. Met.*, 235(December 2017): 115–124, 2018. ISSN 03796779. doi: 10.1016/j.synthmet.2017.12.003.
- [177] Wei Teng Neo, Qun Ye, Ting Ting Lin, Soo Jin Chua, and Jianwei Xu. 4,9-Dihydro-s-indaceno[1,2-b:5,6-b']dithiophene-embedded electrochromic conjugated polymers with high coloration efficiency and fast coloration time. *Sol. Energy Mater. Sol. Cells*, 136:92–99, 2015. ISSN 09270248. doi: 10.1016/j.solmat.2015.01.007.
- [178] Dejan Stekovic and Mikhail E. Itkis. Phenalenyl based neutral radical as a novel electrochromic material modulating visible to short-wave infrared light. *RSC Adv.*, 8(73):42068–42072, 2018. ISSN 20462069. doi: 10.1039/c8ra09804b.
- [179] P. Chandrasekhar, B. J. Zay, G. C. Birur, S. Rawal, E. A. Pierson, L. Kauder, and T. Swanson. Large, switchable electrochromism in the visible through far-infrared in conducting polymer devices. *Adv. Funct. Mater.*, 12(2): 95–103, 2002. ISSN 1616301X. doi: 10.1002/1616-3028(20020201)12:2<95::AID-ADFM95>3.0.CO;2-N.

- [180] Serge Beaupré, Anne Catherine Breton, Jean Dumas, and Mario Leclerc. Multicolored electrochromic cells based on poly(2,7-carbazole) derivatives for adaptive camouflage. *Chem. Mater.*, 21(8):1504–1513, 2009. ISSN 08974756. doi: 10.1021/cm802941e.
- [181] Maryam Bayat, Hossein Izadan, Sara Santiago, Francesc Estrany, Mohammad Dinari, Dariush Semnani, Carlos Aleman, and Gonzalo Guirado. Study on the electrochromic properties of polypyrrole layers doped with different dye molecules, 2021.
- [182] Hongwei Fan, Kerui Li, Xuelong Liu, Kaixuan Xu, Yun Su, Chengyi Hou, Qinghong Zhang, Yaogang Li, and Hongzhi Wang. Continuously Processed, Long Electrochromic Fibers with Multi-Environmental Stability. *ACS Appl. Mater. Interfaces*, 12(25):28451–28460, 2020. ISSN 19448252. doi: 10.1021/acsami.0c09589.
- [183] Vishal Agrawal, Ekta Singla, and Prabhat K Agnihotri. Exploiting Self-Healing Characteristics of Poly(methyl methacrylate) in Gel Electrolyte for Application in Electrochromic Devices. *ACS Appl. Eng. Mater.*, 2023.
- [184] Sheerin Naqvi, Preeti Yadav, Pallab Pahari, and Asit Patra. Dodecyl-substituted poly(3,4-ethylenedioxy-selenophene): polymerization and its solution-processable applications for electrochromic and organic solar cells. *J. Polym. Res.*, 28(7), 2021. ISSN 15728935. doi: 10.1007/s10965-021-02609-8.
- [185] Joo-hee Kang, Yeon-ji Oh, Seung-min Paek, Seong-ju Hwang, and Jin-ho Choy. Electrochromic device of PEDOT – PANI hybrid system for fast response and high optical contrast. *Sol. Energy Mater. Sol. Cells*, 93: 2040–2044, 2009. doi: 10.1016/j.solmat.2009.08.007.
- [186] Chanil Park, Jeong Min Kim, Youngno Kim, Soyoung Bae, Minseok Do, Soeun Im, Sinseok Yoo, and Jung Hyun Kim. High-Coloration Efficiency and Low-Power Consumption Electrochromic Film based on Multifunctional Conducting Polymer for Large Scale Smart Windows. *ACS Appl. Electron. Mater.*, 3:4781–4792, 2021.
- [187] Haijin Shin, Yuna Kim, Thiruvellu Bhuvana, Jiyea Lee, Xu Yang, Cheolmin Park, and Eunkyong Kim. Color Combination of Conductive Polymers for Black Electrochromism. *ACS Appl. Mater. Interfaces*, 4:185–191, 2012.